Ultraviolet Band-Edge Emission from Zinc Oxide Nanostructures

Claire Elizabeth Marvinney

Dissertation
Submitted to the Faculty of the
Graduate School of Vanderbilt University
in partial fulfillment of the requirements
for the degree of

DOCTOR OF PHILOSOPHY
in

Interdisciplinary Materials Science
May 11, 2018
Nashville, Tennessee

Approved:

Richard F. Haglund Jr., Ph.D.

Richard R. Mu, Ph.D.

Sokrates T. Pantelides, Ph.D.

Sandra J. Rosenthal, Ph.D.

Jason G. Valentine, Ph.D

To

Ema and Epa

&

Grammom and Poppop

ACKNOWLEDGEMENTS

This dissertation has been quite the journey, and there have been many helping hands along the way throughout my entire life, both inside and outside of the lab. This research would not be here, as it is today, without the help of my advisor, many collaborators, committee, IMS program, and coworkers. And I would not be finishing my dissertation as sane as I am without the support of my many friends – near and far –, all of my family – nuclear, extended, and chosen –, and especially my boyfriend, Nathan.

First I thank my research advisor, Professor Richard Haglund, for encouraging me to do a rotation in his research lab, being a true mentor, and giving me a lifelong friendship. His knowledge about science and life has guided me through these almost six years, teaching me what it really means to be a researcher, and always pushing me to do my best work and to be my best. I love that we share an interest in travel, politics, and culture, as well as science, it has always made our meetings educational and enjoyable! Additionally, I came into the lab not having taken an English course since high school. Prof. Haglund has the most eloquent writing of anyone I have met, and I hope I have learned some of these skills from him along the way, regardless how often I attempt to string too many nouns together as an adjective. I know we will stay in touch long after the ink on this document dries!

Next I thank Professor Richard Mu. Richard has a longstanding collaboration with our research group, studying ZnO nanowires. It was in his labs that I learned how to grow nanowires and to characterize their optical properties. He encouraged me to learn new skills, suggesting I try a summer in China with his collaborators, leading to my EAPSI Fellowship experience and continued collaboration. He has been a second advisor to me throughout my graduate

experience, supporting my research directions and providing background knowledge for my experiments. Additionally, he really taught me how to be a mentor, always providing opportunities to have the older students teach the newer students, and giving us the freedom to take the lead. I am forever thankful and very glad that even now we continue our collaboration and friendship as I move forward with my career!

I am very grateful to my committee members, Professors Sandra Rosenthal, Sokrates Pantelides, and Jason Valentine, for their expertise and guidance. Their stimulating questions brought about amazing conversations during my defense. That and their insight into my work have strengthened my research, helping me delve further into the physics, materials science, and chemistry by providing new perspectives from a broad range of backgrounds. Thank you Prof. Rosenthal for the background you have provided on ultrafast laser physics and transmission electron microscopy and for always challenging me to think of the broader impact and future of my work. Thank you Prof. Valentine for your expertise in plasmonics and nanophotonics and for asking the most in depth questions about the fundamental purpose of my research. Thank you Prof. Pantelides for your knowledge of condensed matter theory and theoretical physics and for bringing questions from outside of my field, providing me opportunities to think out of the box. I also thank Prof. Pantelides for our collaborations, from the work on complementary spectroscopy techniques to the density functional calculations of the ZnO and MgO interface.

Before I thank all my collaborators, I would like to single out Prof. Daniel Mayo, because he has been my mentor since 2012 when I joined the Haglund lab. Thank you Dan, not only for being a mentor, but for being my friend through all of this! You taught me what it meant to do lab research. You showed me how to turn an idea into research. Discussions with you have always lead to more questions, about what else is possible, what is the future, what more should

we do. I look forward to discussing research and what life holds with you for years to come! Not only with you, but with your family, as Nicole and Draevyn have also become great friends!

Next I thank all of my collaborators in the US and abroad. I acknowledge each of your contributions to this dissertation in the chapter that the contribution appears, but I would like to first thank you here. I thank Prof. Daniel Mayo and Andrew Cook for the years of collaborations on ZnO nanowire growth and characterization. Together we learned a lot about experiment design and nanowire growth! I am glad we still collaborate Andrew. I thank Dr. Jordan Hachtel, for introducing me to STEM-CL and STEM-EELS, and for doing innovative plasmonic research with my samples. I thank Dr. James McBride, for years of TEM/STEM/EDS imaging and analysis of my samples, and helping with the long process of publishing a difficult paper. I thank Prof. Xiao Shen for collaborating on density functional calculations of ZnO interfaces and assisting with making a thorough publication. I thank Prof. Sergey Avanesyan for teaching me about lasers and time-resolved photoluminescence. I thank Prof. Akira Ueda for helping design and fix experiment components. I thank Kent Hallman for teaching me laser spectroscopy design. I thank my undergraduate researchers, Ephraim Bililign, Zhineng Li, Dominic Critchlow, Eion Hindsman-Curry, Joshua Robinson, and Yujie Cai, for your interest and ideas in the research, and your work that continues to lead to new directions and publications!

To my collaborators at Northeast Normal University, I thank you for the great research experience in Changchun, China. To Prof. Yichun Liu and Prof. Haiyang Xu, I thank you for the offer to work with your group for the summer. To Dr. Weizhen Liu, I thank you for being my mentor and connecting me with all the students who trained me on vertical nanowire growth. I thank Dr. Cen Zhang for collaborating with me, as your research was similar to my proposal. I thank Yang Liu for being my friend and coworker that summer, and Dr. Lina Kong for showing

me parts of China outside of the lab. Finally, I thank everyone else in the lab that I have missed here, so many of you helped me and supported me! I hope I did the same for you!

I did not collaborate with everyone in my research groups, but we always assisted each other while working towards our graduate degrees! I want to take a moment now to thank all of you. First, to the Haglund lab, from members who graduated and inspired my work, to members just starting as I leave, I thank you: Dr. Ben Lawrie, Prof. Krishen Appavoo, Dr. Jed Ziegler, Dr. Bob Marvel, Dr. Rod Davidson, Prof. Dan Mayo, Dr. Jorge Salas, Dr. Christina McGahan, Kent Hallman, Kristen Engerer, Jason Bonacum, Dr. Kevin Miller, Nick Beier, Zhihua Zhu, Sam White, Matthew Feldman, David Curie, Ryan Nolan, and all the other summer students and post docs who have worked with us over the years! Second, to the Mu lab, from Masters students to Ph.Ds and everything in between, we have always been a close-knit group, I thank you: Prof. Dan Mayo, Anthony Mayo, Andrew Trenchard, Kenneth Coca, Prof. Akira Ueda, Prof. Sergey Avanesyan, Dr. Jennifer Jones, Dr. Jian Ma, Andrew Cook, Carcia Carson, Omar Ali, Adrian Parker, April Byrne, Elena Galea, and all the students who rotated through the lab!

And I wouldn't be here without the support of my program, the Interdisciplinary Materials Science Program. I thank Prof. Ron Schrimpf for taking an initial interest in my application. I thank Prof. Greg Walker for his considerate charge of the program. I thank Prof. Sharon Weiss for being the faculty advisor of the Vanderbilt Materials Research Society, an outreach group I was greatly involved in. I thank Prof. Anthony Hmelo for training and assisting me in VINSE and outreach, and thank Robin Midgett for his years of mentoring the IMS students with TAing, becoming our friends. I thank Professors Richard Haglund, Jason Valentine, Sharon Weiss, Ronald Schrimpf, Kalman Varga, Kirill Bolotin, Timothy Hanusa, Eva Harth, Greg Walker, and James Wittig for their teaching of the coursework for my IMS degree.

I give the most heartfelt thanks to Sarah Ross, who has been in charge of keeping IMS, VINSE, and MRS running smoothly. Without you Sarah, we would all be lost. You have always been someone to turn to when things aren't going to plan, and always have amazing science demos to share, so thank you! I also thank Rene Colehour, Alisha McCord, and Pat Tellinghuisen for their help to the program and with outreach over the years! And of course I thank my cohort, and many others in the program. To my cohort – Dr. Andrew Westover, Dr. Landon Oakes, Dr. Jun Li, Kristen Engerer, Kyle Zufelt, Dr. Alice Leach, Dr. Kevin Miller, Matt Gerboth, Brad Baer, and Keith Share – thank you for the long homework hours and years of working together! And to many other IMS, VINSE, engineering, and physics students I have commiserated with – Dr. Joy Garnett, Dr. Kelsey Beavers, Dr. Toshia Wrenn, Dr. Noah Orfield, Dr. Zach Coppens, Dr. Michael King, Dr. Nelson Gaspard, Dr. Amy Ng, Charlie Arutt, Zhihua Zhu, Mengya Li, Rose Perea, Dan Burger, Tengfei Cao, Anna Douglas, Kate Moyer, Kemar Reid, Danielle Bailey, Jake Benzing, Casey Brock, Talitha Frecker, Nathaniel Freymeyer, Liuda Prozorovska, Nitin Muralidharan, Drew Tonigan, Kristina Kitko, and Sarah Harrell – thank you!

There are so many people to thank for the almost six years of my graduate career, and I wouldn't be here without the friends I made along the way. To my first mentors, Dr. Michael King and Dr. Nelson Gaspard, I thank you for teaching me and taking me out for many happy hours! To my partners in crime, Dr. Christina McGahan and Kristen Engerer, thank you for all the mischief we got up to over the years, especially those beautiful Christmas lights, Christina! I know times were rough, and I certainly wouldn't have made it through without the two of you flanking me in the office, commiserating at the worst of times and rejoicing at the best of times! To my roommates, Emily Overberg and Madison Knowe, Kristin Engerer, Dr. Laura Engerer, and Dr. Alice Leach, and Dr. Monica Bennett, thank you for relieving grad school stress by

dancing, baking, and hiking with me! To Dr. Joy Garnett and Dr. Lisa Mace, thank you for being my first Nashville friends. To my board gamers turned hiking friends – Dr. Daniel Bennett, Dr. Monica Bennett, Dr. Liz Ferrick-Kiddie, Dr. Brad Kiddie, Dr. Matt Brodt, Dr. Andrew Westover, Jamie Westover, Dr. Arthur Russakoff, Jodie Hawk, Kristin Engerer, Christian Bonnell – thank you for the years of fun becoming lifelong friends! To my ballroom friends – Christian Bonnell, Kristin Engerer, Sarita Bhat, Danny Pugh, Dr. Christina McGahan, and Bill Smith – thanks to this hobby and expanding beyond Vanderbilt! To my Zumba and running friends – Rachel Helvering, Dr. Nicole Diggins, Dr. Christina McGahan, Bill Smith, Dr. Cecilia Chung, Dr. Alice Leach, Dr. Laura Glass, Dr. Jennifer Stancill, Dr. Gwynne Davis – thanks for the years of exercising, health goals, and social outings, keeping us sane! And to my close IMS friends – Dr. Alice Leach, Brad Baer, Matt Gerboth, Lisa Womack, Drew Tonigan, Kristin Engerer, and Christian Bonnell – thanks for the years of commiseration! And thank you Susan Moody and Danny Pugh, for keeping me inspired with art and dance classes these six years, and to all my past art, dance, and music teachers, for training my right brain!

If I had not accepted Vanderbilt's offer and not moved to Nashville, I would not have met Nathan Bartlett. Thank you Nathan, for everything you have done with me these last two years as I finish my degree. From hiking, caving, and kayaking with Seraph (who has become our shared dog, the most anxiously loving creature I have ever met, being my pillow as I wrote my dissertation from home, keeping me active with her need for and love of running), to creating our own garden and doing home improvement, to many wonderful vacations and endless board game duels, and even getting me to finally play the Legend of Zelda, you have brightened my life and supported me with every decision made about my/our future! I love you. And I also thank you, Nathan, for introducing to me to so many wonderful people as my friends earned their degrees

and moved away. So thank you first to Nathan's family, the Bartletts, Cherie, Randy, Thomas, and Joseph, for their newfound support, friendship, and adventures! And to my new friends JV Vest, Haley Vest, Jesse Hoover, Rachel Gentry, Elena Knaffl, Sydney Norman, James Massey, and Andy O'Neal for board game fun and other adventures! Here's to many more years!

Additionally, I would not be here without the friends, teachers, and family supporting me from so many other stages of my life! I was interested in getting my Ph.D by the time I was four years old (thanks mom and dad!), but that decision didn't solidify into reality until I was applying to graduate school at the end of my physics degree at Rensselaer Polytechnic Institute. Thank you to Prof. Peter Persans and Prof. Jim Napolitano for encouraging me to apply to programs outside of physics, to Prof. Wayne Roberge for being my first research mentor, and to Prof. Christian Wetzel for helping me experience materials science research, leading me to the applied nanoscience I truly love! And to my closest class of 2012 RPI friends – Dr. Evan Weinberg, (almost Dr.!) Nicole and Alan Lummis, Rachel Schnabel – thank you for maintaining our wonderful friendships! We have had shared great times since graduating, and it's wonderful to support each other in our careers and lives! And to the friends I have made through you – Tiff Brucker, Mike Deroche, Jenna Hoopingarner, Pat Terrio, Alan Barr, Olga Prikhodko, Brian Ware – thank you for your support in finishing this crazy degree! Additionally, to my RPI physics friends – Zack Zvendgard, Sarah Evans, David Lombardo, Steve Lentine, Erin Hansen, Dr. Charles Martin, Dr. Alyssa Montalbano, Andrew Birkel, and many more – thank you for support through both degrees! I hope we reconnect soon! I also thank the RPI ballroom team, swim and water polo club, dance club, and outing club for years of friendship and support!

Some of you friends have even stuck with me since Maranacook Community high school or earlier! Delaney Evans, Marissa Perry, Patsy Frey-Davis, Matt Frey-Davis, Nicole Albee –

you guys mean so much to me. We are “the ladies” (except Matt and Thomas, haha) and our summer beach and New Year’s traditions have kept me traveling to my favorite state for as long a vacation as I can manage all these past years! Thank you to Delaney especially here, for being my cheerleader in writing the dissertation document, helping keep me on task! Thank you to other K-12 friends, and to my Maranacook teachers: from Steve DeAngelis for inspiring me to go into physics, to my mom, Cheryl Marvinney, for being my rock (hehe, bad geology joke) as my teacher and mentor at Maranacook, Dennis Drews for being my advisor all those years, to Carrie Emmerson, Sue Melcher, Mark Wicks, Robyn Graziano, Roselea Kimball, and the rest of my amazing teachers, skiing, swimming, running, and soccer coaches from early childhood and on! And thank you to those who taught me at summer camps, especially to those at the National Youth Science Camp! All NYSCers from 2008, I am so glad we have a community to continue inspiring each of us to do amazing things with our lives! Let’s always stay in touch!

So many family friends have supported me through my life as I dreamed of higher education and worked towards my doctorate! Thank you to the entire Waldron clan for becoming extended family with all the adventures and celebrations these past almost 28 years! Especially to Tim, Kiki, and Jess for truly being lifelong friends and always challenging me to learn! Thank you endlessly to the Whittemores, Darcy, Henry, Katie, and Sam, always challenging me to find new adventures and knowledge, being the cousins Kyle and I never had with us in Readfield. Thank you also to the Peales, Debbie, Rob, Rich, and Ian, for being another second family, keeping me in touch with careers and knowledge outside of and inside of STEM! And thank you to the Boes, Eivind, Onnie, Bronwen, and Miranda, a true lifelong second family, running back to when my dad was in HS! I also thank the Clarkes, Kenistons,

Grazianos, Bourgoines, Parkers, DeAngelises, Wickses, Monsuliks, and many others for their support, mentorship, and friendship over the years of my childhood to adulthood!

Of course, I couldn't have done this degree, and all the work up to going to graduate school, without the extremely supportive family that I have. My grandparents all went to college, supporting both their children and grandchildren to not only get undergraduate degrees, but to achieve higher education as well, where they desired. My grandfather, Raymond Marvinney - Epa, got a mechanical engineering degree and becoming one of the first rocket scientists, working for Reaction Motors; my grandmother, Ruth Marvinney - Ema, got a nursing degree and used it throughout her life, first on the job and then with her family and friends; my grandfather, Victor Lykens - Poppop, worked towards his physics degree until he got a job offer to work for IBM, where he worked on early home computers and electronic equipment; and my grandmother, Elizabeth Lykens - Grammom, got an art degree, continuing teaching pottery throughout her life to her community, even teaching all of her grandchildren and friends. They taught their family well! Thus to all my aunts, uncles, and cousins, you are always an inspiration. I love that our family gatherings are full of intellectual conversation, from the arts, to politics, to science, as well as full of fun games and food! Thank you Beth, Jim, Anna, Peter, and Ryan Geier, and Dave, Kelly, Alex, Liz, and Quinn Lykens. Thank you Dr. Denny, Don, Rayme, Tanya, Dr. Elias, Ian, and Tasha Marvinney, Ranny, Stefan, Eliese, and Yvonne Dysktra, Pat, Chuck, and Nick Patti, and Gail, Jeff, Sam, and Kevin Grove. And to the entire extended family and the new family joining us with wedding celebrations these past years!

I have saved thanking the most influential people for last, my parents and my brother. Mom and Dad, the world of discovery you fostered for Kyle and I as we grew up was one of the most amazing things you could have given us! Kyle Marvinney, thank you for enduring your

younger sister crashing your projects and games, and joining in mine! Also, for being competitive with me throughout life, always challenging each other to be better. Thank you Kyle, for being my friend as an adult, and for always reminding me while I worked on this degree that I am lucky to be in a career where I do scientific analysis. Your drive, focus, and perspective on life has always lifted me up – except maybe those times when we pushed each other in the mud – and you are a role model for healthy living, outdoor and scientific adventure!

Of course, Kyle and I have our parents to thank as role models for what a healthy lifestyle truly is. Thank you, Mom and Dad, for raising us both so well, and for becoming our friends as we grew into adulthood! You have always inspired me with your enthusiasm for science wherever we go, from stopping for rocks to identifying birds, and of course, the many baking soda volcanoes and crayfish and sand dollar finding adventures! My first career choice was to be a geologist, just like you both! And in some ways, I joined you, by going from physics to materials science so I can study crystalline materials too! The community you built in Readfield, with your families, with our pets, is one that nurtured education and exploration. To my mom, Cheryl Marvinney, thank you for always supporting me, asking me questions, stretching both our knowledge, and reminding and teaching me to love the outdoors, science, and the little things in life! You are an inspiring teacher, mother, and friend, and have taught me well! I love you. To my dad, Dr. Robert Marvinney, Bob, thank you for inspiring me to get my Ph.D., to become the fourth Dr. Marvinney, pushing me forward to my best, being my dad and friend, being interested in learning what I know, and teaching me how to be a scientist, public speaker, and adventurer! I love you. This dissertation could not have been completed without the love of my parents!

This dissertation is a result of work funded by the Office of Science, U.S. Department of Energy (DE-FG02-01ER45916), the U.S. National Science Foundation East Asia and Pacific Summer Institute (1415013), and the Vanderbilt Institute for Nanoscale Science and Engineering (VINSE).

TABLE OF CONTENTS

Page

LIST OF TABLES

Table Page

LIST OF FIGURES

CHAPTER 1

INTRODUCTION

Zinc oxide is a wide band gap (3.37 eV) semiconductor with a high exciton binding energy (60 meV), of interest for optoelectronic applications due to both its ultraviolet (UV) and visible emissions. This dissertation shows four methods of tuning the UV band-edge emission of ZnO nanostructures. First, in a ZnO/MgO core-shell nanowire there exists a UV photoluminescence enhancement that varies with MgO thickness due to the formation of Fabry-Perot and whispering gallery optical cavity modes. Second, exciton-plasmon coupling in ZnO/MgO core-shell nanowires leads to enhanced emission of the UV luminescence. The combination of optical cavity formation and Ag plasmons leads to two enhancement mechanisms that depend on the MgO spacer thickness. Third, the structure of the MgO shell in the core-shell nanowires depends on the ZnO surface conditions. Changing the growth parameters of the ZnO nanowires tunes the ZnO *m*-plane surface conditions and thus the MgO shell structure. A smooth MgO shell supports enhanced UV photoluminescence through the formation of guided-wave optical modes, while a rough MgO shell supports neither the enhancement nor the guided modes. Fourth, temperature-dependent studies of exciton-phonon coupling elucidate that the vertically oriented nanowires, grown hydrothermally, have fewer defects and a sharper UV band-edge emission than the previously studied randomly oriented nanowires, further indicating that growth protocol has a critical influence on the UV optical properties of ZnO. Additionally, a novel structure, ZnO "nanopopcorn" showed strong exciton-phonon coupling, highlighting its high defect density. In summary, there is a range of mechanisms that can be used to enhance,

modify, and control the UV band-edge emission in ZnO nanostructures, with vertically oriented ZnO nanowires having the most promise for enhanced UV emission optoelectronic and all-optical devices, from on-chip waveguides, lasers and LEDs, to scintillators and sensors.

1.1 Motivation

Interest in zinc oxide (ZnO) is predicated on its potential for ultraviolet (UV) optoelectronic and photonic devices, and has persisted because of its stable room temperature optical properties, material abundance, and biocompatibility.[1-6] Currently, zinc oxide nanomaterials and interfaces are studied for applications ranging from transparent electrodes, light-emitting diodes, and nanolasers, to biological sensors and scintillators.[1,2,7-12] In 2015 some eight thousand papers were published on ZnO according to the Scopus search shown in Figure 1.1,[2] with ZnO nanostructure publications of particular interest in the last 20 years. My dissertation extends this body of ZnO work by furthering our understanding of the ZnO UV photoluminescence enhancement mechanisms due to optical cavity formation and plasmon-exciton coupling, and by determining the ZnO material structure characteristics for optimizing the UV emission.

Zinc oxide is a group II-VI semiconducting material, with a band gap of 3.37 eV at room temperature. For optoelectronic applications, the band-edge emission of ZnO is similar to GaN (E_{gap} = 3.4 eV), a group III-V semiconductor. However, at $E_{binding}$ = 60 meV, ZnO has the highest exciton binding energy of the II-VI semiconductors, and it is much larger than the exciton binding energy for GaN ($E_{binding}$ = 21 meV), making ZnO a more stable room-temperature emitter than GaN.

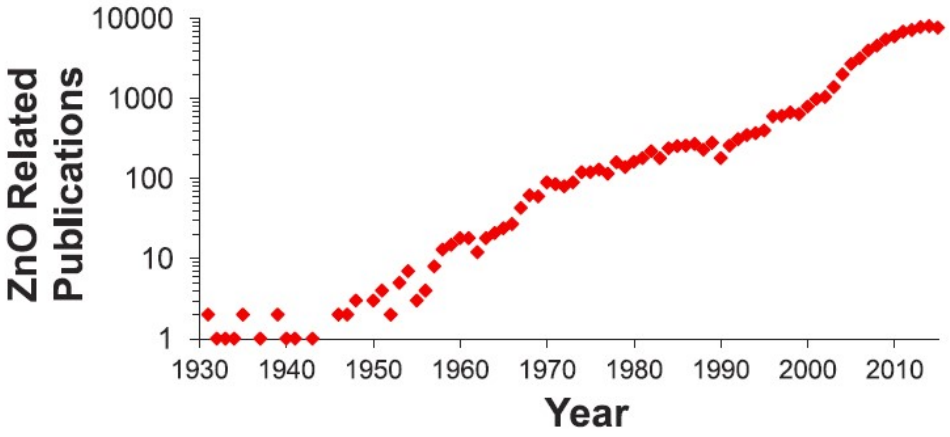

Figure 1.1: The number of annual ZnO publications versus year, according to a search of the Scopus database by Rogers, *et al*, for the term 'zinc oxide' in the abstract, title, or keywords.[2]

Gallium nitride is currently used in commercial optoelectronic devices such as blue light emitting diodes and diode lasers.[2] However, without a stable p-type dopant that performs better than p-GaN, ZnO has yet to be reduced to practice in a commercial homojunction optoelectronic device as GaN has been.[2,13] The difficulty in p-type doping of ZnO is caused by self-compensation, that is, when ZnO is doped with a p-type material, native donor defects spontaneously form to compensate the deliberately introduced acceptors.[13] In the past, research efforts have demonstrated ZnO homojunction light-emitting diode devices, though the p-type carrier concentration was relatively low ($2x10^{16}$ cm^{-3}).[14] Efforts continue, with a ZnO homojunction epitaxial nanofilm device boasting a phosphorous doped p-type carrier concentration of $5.7x10^{18}$ cm^{-3}, keeping its p-type carrier concentration for two months before converting back to n-type.[15]

In spite of the failure so far to find a stable p-type ZnO material, interest in ZnO persists, not only because of its desired room temperature exciton stability, but also because of its material abundance and cost.[2,3] The cost of ZnO is closely tied to the cost of zinc, the fourth

most commonly used metal in the world.[3] In 2016, the US price for zinc was $0.99/lb, while in comparison, the cost for gallium was $400/lb.[4] This stems from the fact that 13.22 million metric tons of zinc were refined in 2016, with 1.9 billion metric tons still available in reserve worldwide.[4] Gallium on the other hand, only saw 375 metric tons refined in 2016, with a worldwide reserve of 1 – 2 million metric tons.[4] The orders of magnitude less refined Ga than refined Zn stems from the fact that Ga is refined from aluminum and zinc ore in concentrations of 50 parts Ga per million parts Al or Zn.[4] Thus even while GaN is the predominantly used near-UV optoelectronic emitter, the UV optical properties of ZnO are still worth studying, because when p-type ZnO is stabilized, the operating lifetime of ZnO devices should be much greater than that of GaN. Additionally, it took over two decades to develop the stable, Mg-doped p-GaN, and this discovery won the 2014 Nobel prize in physics for its critical contribution to blue light-emitting diodes.[16,17]

Zinc oxide forms crystalline wurtzite in a variety of nanostructures, with small variations in growth conditions (temperature, pressure, reactant ratio) leading to large morphology differences.[18-20] Of the various possible ZnO nanostructures,[1,5,8] nanowires offer a highly crystalline nanostructure that in principle support both guided-wave luminescence[21,22] and optical cavity modes.[23,24] The widely studied emission properties of ZnO are also sensitive to growth, as the high surface-area-to-volume ratios in nanostructures lead to variation in the strength and wavelength of not only the UV exciton emission but also the broad visible emission associated with a superposition of defect states.[1,18] Both the UV and visible emission of ZnO can be coupled to surface plasmons, which affect the relative emission decay probabilities between the radiative and non-radiative pathways, leading to enhanced or quenched luminescence.[21,25-29]

Changes to these intrinsic and extrinsic properties of the band-edge emission of ZnO through control of the ZnO nanostructure and the surface environment are still being addressed.[2]

The research in this document shows that when ZnO nanowires are decorated with metal nanoparticles, the photoluminescence and electroluminescence yield is enhanced by the Purcell mechanism due to exciton-plasmon coupling. Cathodoluminescence and electron energy loss spectroscopy enable a detailed analysis of these metal nanoparticle plasmon modes.[30] Furthermore, coating nanowires with an MgO cladding layer shows an additional photoluminescence enhancement that is dependent on the MgO thickness, caused by the formation of optical cavity modes.[31] Surprisingly, the MgO thickness dependent enhancement depends critically on the ZnO growth conditions and *m*-plane surface structure.[32] Of the possible nanowire morphologies, vertical "carpet" ZnO NWs are the most promising for waveguiding and on-chip applications, due to their strong, unidirectional UV band-edge emission waveguided along the *c*-axis. Temperature dependent photoluminescence shows that the carpet nanowires have fewer defects than the randomly oriented nanowires, while the novel, free-form ZnO "nanopopcorn" shows strong UV exciton-phonon replica emissions and defect emissions unseen in either of the nanowire structures. Overall, vertically-oriented carpet ZnO nanowires are an attractive architecture for optoelectronic and all-optical devices, using plasmon-exciton coupling and optical confinement for enhanced luminescence, sensing, and lasing.[11,33-38]

These results demonstrate the range of variation possible in the ZnO band-edge exciton emission, controlling intrinsic emission properties with changes in structure and surface states, and controlling extrinsic emission properties through plasmon-exciton coupling techniques. A deeper understanding of the ZnO band-edge emission enhancement enables the study of laser devices, from waveguided lasing[22,34] in vertical "carpet" ZnO nanowires for propagation of UV

light in a three-dimensional device architecture, to random lasing in ZnO nanoparticle films[39] - similar in morphology to ZnO nanopopcorn. This control and enhancement of the ZnO band-edge emission is ideal for use in future optoelectronic and all-optical applications, from on-chip waveguides, lasers and LEDs, to scintillators and other detectors.

Before discussing the ZnO UV band-edge emission experiments in subsequent chapters, first the physical and optical properties of ZnO and ZnO nanostructures are presented. Relevant background information is given on plasmonics, as plasmon-exciton coupling is a commonly used technique for UV emission enhancement throughout this research.

1.2 ZnO Structure

1.2.1 Crystal Structure

Zinc oxide is a group II-VI semiconductor compound with a tetrahedral bonding configuration where each zinc atom is surrounded by four oxygen atoms and vis versa. This tetrahedral configuration is shown in Figure 1.2. Tetrahedral bonding is common among II-VI and III-V compound semiconductors and typically results in a crystal structure of either cubic zinc-blende or hexagonal wurtzite.[7] However, zinc oxide favors the wurtzite structure[5,8] (Figure 1.2) only growing in the zinc-blende structure epitaxially from a zinc-blende substrate.[40]

In ZnO there is a large electronegativity difference between the Zn^{2+} and O^{2-} ions, that of 0.91 and 3.5 on the Pauling scale, respectively,[41,42] which leads to a considerable bond polarity with an effective charge of $Z^* = 1.15 \pm 0.15$.[43] This means that the bond type of ZnO is actually between that of typical III-V and many II-VI semiconductors (covalent) and that of alkali halide insulators (ionic).[7] This high bond polarity and strong ionic character of ZnO is

responsible for the wurtzite structure preference, which is more common in higher polarity tetrahedral bonding (BeO, ZnS, InN) while zinc-blende is more common in lower polarity tetrahedral bonding (CdTe, GaAs, AlP).[7]

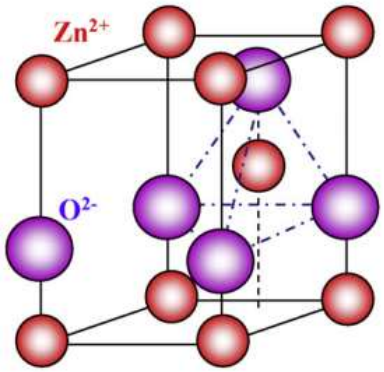

Figure 1.2: A primitive unit cell of wurtzite ZnO showing the tetrahedral coordination of zinc and oxygen atoms.[44]

The hexagonal wurtzite structure of zinc oxide is uniaxial, directed along one of the tetrahedral bonds, known as the *c*-axis, as shown in Figure 1.3. The *c*-axis [0001] is polar due to the bond polarity between Zn^{2+} and O^{2-}, which leads to a lengthened *c/a* axis ratio in ZnO, at *c/a* = 1.602, the highest of all wurtzite-type semiconductors.[7] The lattice constants of wurtzite ZnO in ambient conditions are *a* = 3.249 Å and *c* = 5.207 Å. The (0001) face is Zn-terminated, while the $(000\bar{1})$ face is O-terminated, with planes designated by the Miller-Bravais indices (*hkil*). Having four lattice indices allows for symmetries in the hexagonal lattice to be visibly displayed, as the hexagonal lattice has three-fold and six-fold rotational symmetry. The sides of wurtzite ZnO with equal number of Zn and O ions are non-polar, the $(11\bar{2}0)$ *m*-plane and the $(10\bar{1}0)$ *a*-plane. The *m*- and *a*- directions are shown in Figure 1.3.b, with the four indices showing symmetries.

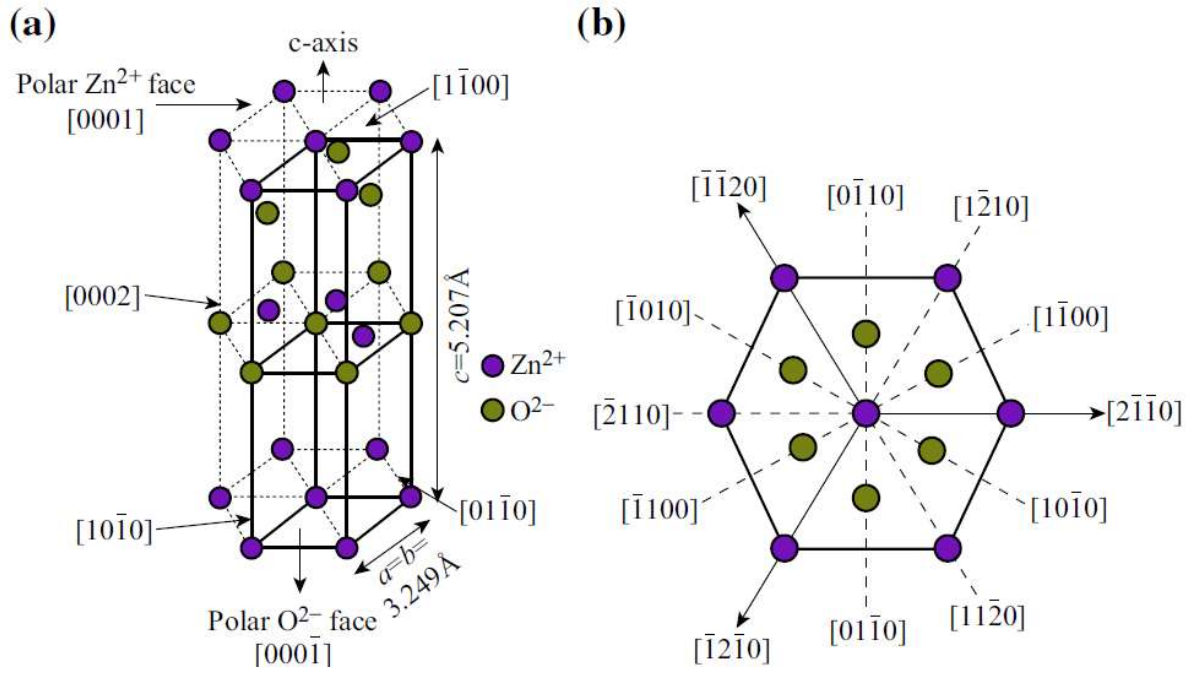

Figure 1.3: Various crystal planes of wurtzite ZnO identified in a) a ZnO unit cell and b) a cross section of the hexagonal crystal.[10]

The primitive wurtzite lattice (Figures 1.2 and 1.3.a) with its two pairs of Zn and O ions, is designated by the space group $P6_3mc$.[7] This space group has 12 symmetry operations, with both six-fold and three-fold rotational symmetry, along with glide plane and mirror symmetry. However, due to its polarity, wurtzite ZnO is non-centrosymmetric, lacking an inversion center. This space group leads to both the piezoelectric and second-harmonic-generation properties of ZnO,[7,45-48] not studied here.

1.2.2 Phonon Modes

A phonon is a quasiparticle defined as the collective oscillation of an elastic and periodic arrangement of atoms or molecules. Phonons are a quantized excited state of vibrational modes, and in zinc oxide the excited phonon dynamics depend on three parameters of the crystal lattice:

i) the uniaxial wurtzite crystal structure, ii) the difference in mass between the Zn and O atoms, and iii) the strong ionic nature of the Zn-O bond. Group theory predicts 12 allowed phonon eigenmodes, with three acoustic phonon modes and nine optical phonon modes.[7,49] Figure 1.4 depicts the displacement vectors of the Zn and O atoms for the optical phonon modes and their vibrational energies. The mass difference between Zn and O leads to the O atom having the larger (dominant) displacement in all but the $B_1^{(1)}$ and $E_2^{(1)}$ modes. Additionally, because of the high bond polarity of ZnO, two optical phonon modes are polar, A_1 and E_1, leading to a splitting of the polar vibrational modes when they propagate parallel to the displacement vector of the atomic motion (longitudinal optical phonons) and perpendicular to the displacement vector of the atomic motion (transverse optical phonons). The longitudinal optical (LO) modes oscillate at much higher energies than the transverse optical (TO) modes, in this splitting.

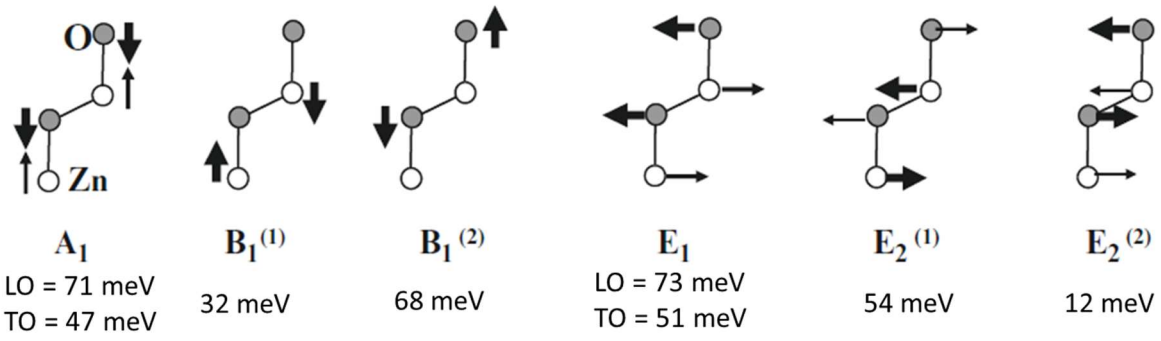

Figure 1.4: Eigenvectors of the ZnO optical phonon modes, with bold arrows representing the dominating displacement vector for each mode, from Klinghsirn, *et al*.[7] The oscillation energy associated with each mode is noted.[7]

The calculated dispersion of the ZnO phonon modes is shown in Figure 1.5, with experimental measurements overlaid. In a cubic system, the A_1 and E_1 modes would be the same vibrational mode. However, due to the uniaxial nature of the hexagonal wurtzite crystal structure of ZnO, there is splitting between these phonon modes when they propagate parallel and

perpendicular to the c-axis, making TO and LO phonon branches. Between the TO and LO phonon modes lies the reststrahlen band, where a negative dielectric function screens incident radiation and prevents propagation of phonon modes. For ZnO at the gamma point, the E_1 and A_1 reststrahlen bands are positioned at 411 – 593 cm^{-1} and 381 – 582 cm^{-1}, respectively.[7] Additionally, Figure 1.5 displays data not only for the higher energy optical phonon branches, but also the lower energy acoustic phonon branches, minimized at the gamma point of the Brillouin zone.

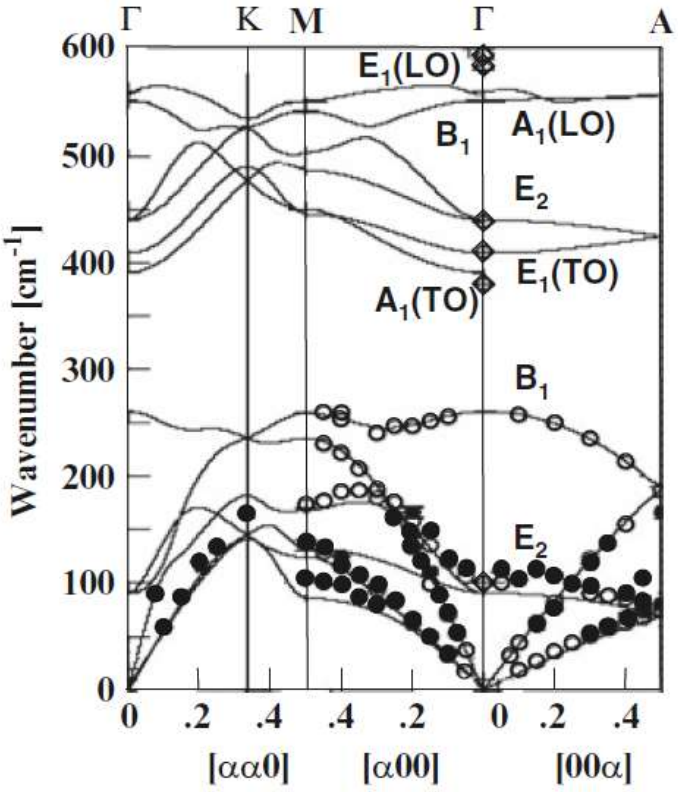

Figure 1.5: Ab initio calculated ZnO phonon dispersion relations along directions of high symmetry in the wurtzite structure,[50] with experimental data represented as solid circles,[51] open circles,[52] and open diamonds.[53] Reprinted from Klingshirn, *et al*.[7]

1.2.3 Possible Nanostructures

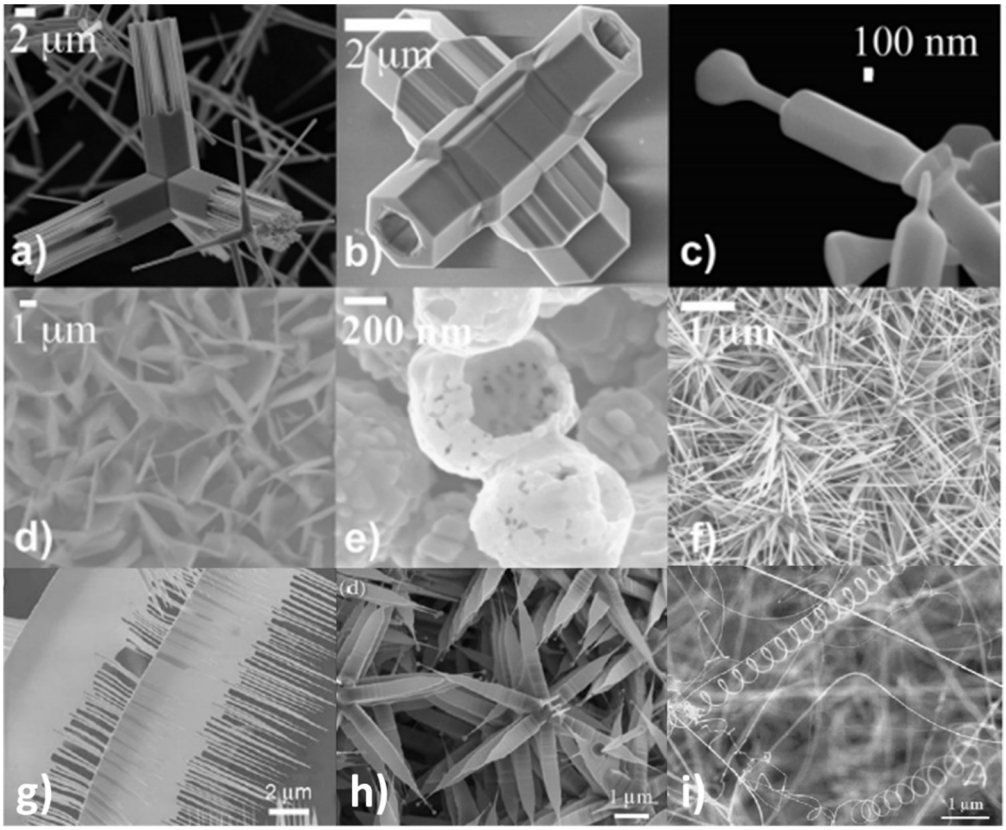

Figure 1.6: Scanning electron micrographs of ZnO nanostructures, with ZnO a)-b) tetrapods, c) random diameter structure, d) nanosheets, e) nanoshells, f) multipod nanowires, g) nanocombs, h) nanopropellors,[54] and i) helical nanobelts.[55] a)-f) are grown by Djurisic *et al* (2010),[1] and g)-i) are presented in the review Djurisic, et al (2006).[20]

Currently, there are many research groups studying the properties of nanostructured materials for optoelectronic and optical devices.[1,2,5,56] By controlling the growth conditions of ZnO, a variety of micro- and nanostructures can be grown, including tetrapods, nanoshells, nanospirals, nanocombs, multipod nanowires, nanosheets, random morphology structures, and nanopropellors, shown in Figure 1.6.[1,5,20] The optical properties of ZnO nanostructures diverge from bulk ZnO optical properties due to both the decreased size and increased surface area-to-

volume ratios, leading to increased optical confinement, surface interactions, and quantum confinement in one-, two-, and three-dimensions.[1,8,57,58]

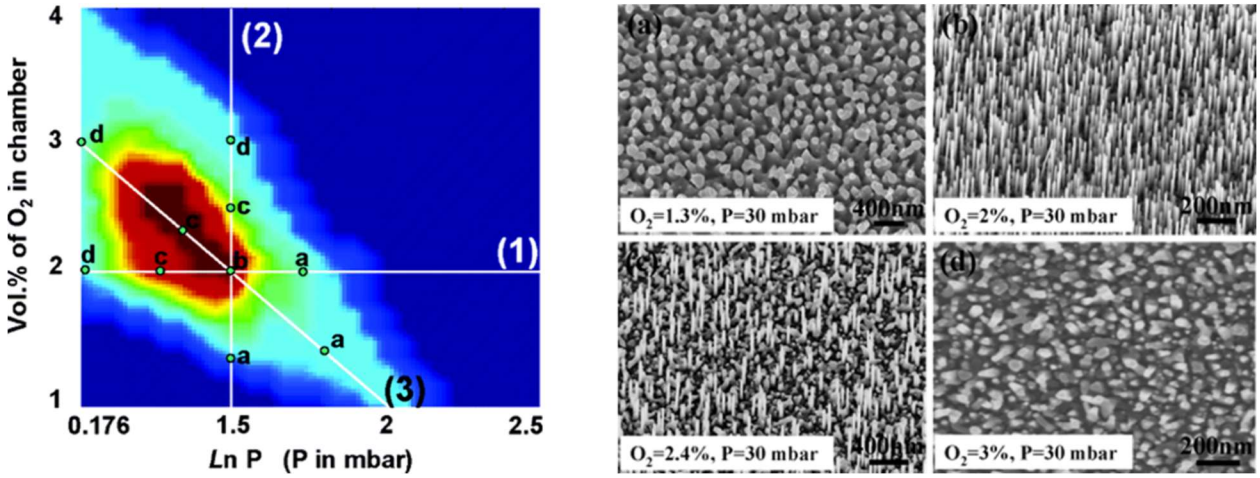

Figure 1.7: Left: the "phase space" diagram that correlates oxygen partial pressure and the growth chamber pressure for growing aligned ZnO nanowires, created from over 100 experiments, with Matlab smoothing (red = ordered nanowires, blue = rough seed layer).[19] Line (1) has constant oxygen partial pressure; line (2) has constant system pressure; line (3) varies linearly with both. Right: SEM images that correspond to ZnO nanowire samples grown with conditions at point a), b), c), and d) on line (2).[19]

The various techniques for growing ZnO lead to the variability in nanostructure, with i) synthesis techniques ranging from chemical vapor deposition to hydrothermal synthesis, ii) variation in the substrate ranging from Si and GaN, and iii) controllability of the growth parameters from oxygen content to temperature.[1,3,8,10,15,18-20,59] Slight changes within the same growth method can change crystal qualities and morphology of the nanostructure.[18,19] In Song, *et al*,[19] in a vapor-liquid-solid growth method, the total chamber pressure and partial oxygen pressure were varied in over a hundred experiments to determine the phase space for their desired nanostructure, that of ordered ZnO nanowires, Figure 1.7. Slight changes in the oxygen partial pressure during growth led to large changes in the morphology of the ZnO on the

sample.[19] Zúñiga-Pérez, *et al*,[18] in a study of the oxygen pressure and temperature for growing pulsed laser deposited ZnO nanowires, found that these phase-space variations have a pronounced effect on the ratio of near-band edge emission to visible emission of the ZnO nanowire luminescence. A reduced growth temperature and an oxygen rich environment lead to better quality nanowires with increased UV emission.[18]

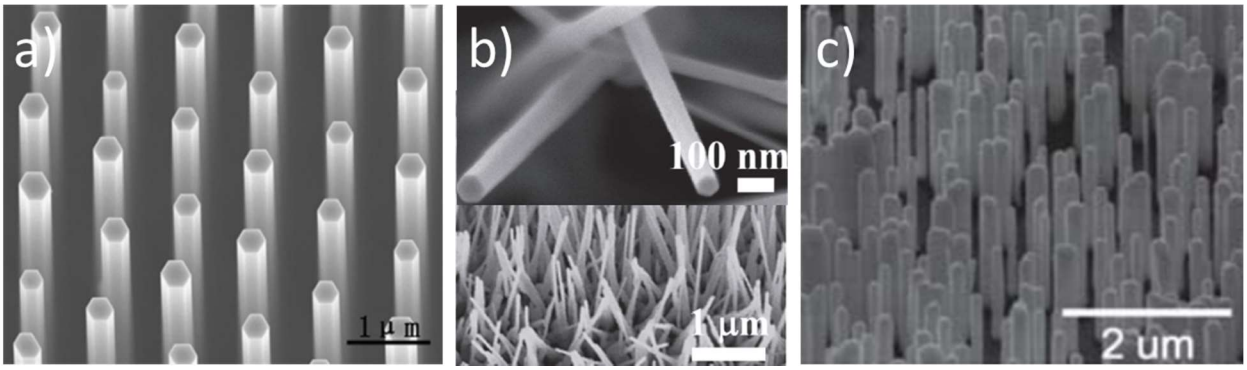

Figure 1.8: Scanning electron micrographs of ZnO, a) perfectly aligned nanowires grown through chemical vapor deposition on a gold nanopatterned sapphire substrate,[60] b) randomly oriented nanowires growth through a vapor-transport method on a gold nanocluster coated Si substrate,[61] and c) vertically oriented nanowires grown through a hydrothermal synthesis on a p-GaN substrate.[62]

Of the many nanostructures of ZnO, nanowires are a favorable architecture for ZnO optoelectronic devices, because confinement of optical modes and waveguiding in the high refractive index material (n_{ZnO} =2.45) can lead to enhanced UV photoluminescence (PL) output and even lasing.[22,23,25,33,63] Zinc oxide nanowires are grown by methods from chemical vapor deposition to hydrothermal synthesis, using both patterned (to deterministically seed the nanowire position) and unpatterned substrates.[1,15,18,19,59,60,64-67] Figure 1.8 shows the results of three different ZnO nanowire growth techniques. In Figure 1.8.a a sapphire substrate was patterned with a gold nanoparticle array in a polystyrene self-assembly process, then vertically

oriented ZnO nanowires were grown deterministically from the nanoparticles by chemical vapor deposition.[60] Figure 1.8.b shows randomly oriented ZnO nanowires grown by a vapor transport deposition on an Si substrate covered in sputtered gold nanoparticles.[61] Finally, the hydrothermal method for growing the vertically oriented ZnO nanowires shown in Figure 1.8.c required no gold seeding of the c-axis oriented p-GaN substrate.[62]

1.3 ZnO Luminescence

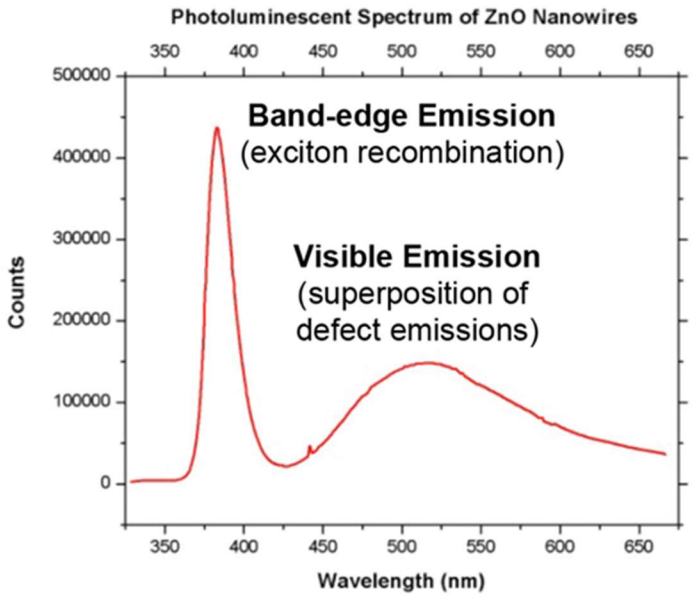

Figure 1.9: Room-temperature photoluminescence of ZnO nanowires. The sharply-defined UV emission is the band-edge exciton recombination, centered at 3.3 eV. The visible emission, centered around 2.3 eV, is a superposition of intrinsic defect emissions.

Zinc oxide has a direct UV near-band-edge emission and a second, broad emission in the visible region associated with donor-acceptor pair and other defect states, as shown in the typical

photoluminescence spectrum of ZnO nanowires in Figure 1.9. The room temperature near-band-edge emission of ZnO is the recombination of free excitons, varying from 373 – 390 nm, with dependence on the nanostructure size and morphology.[18,20] The broad peak centered at 2.3 eV is a superposition of visible emissions from various intrinsic defects.[7,20,68] For highly-crystalline ZnO, the band-edge exciton emission is improved and the non-radiative decay through defect pathways is minimized, leading to enhanced UV emission.[69]

1.3.1 ZnO Free Excitons

An exciton is a quasiparticle representing the bound state of an electron and hole attracted by their electrostatic Coulomb force. When an electron is excited from the valence band to the conduction band of a semiconductor, excitons can form when the Fermi velocities of the electron and hole are equal. There are two types of excitons. Frenkel excitons are localized near their ion core, however Wannier-Mott excitons are free to move about the crystal, as they exist when the rate of electron-hole hoping between crystal cells exceeds the Coulomb coupling strength of the excitons.[70] The binding energy of a free Wannier-Mott exciton has the character of the hydrogen atom binding energy, and can be expressed as a relationship related to the eigenstate solutions to the hydrogen atom Schrödinger equation, as[70]

$$E_n = \frac{\mu e^4}{2\hbar^2 \varepsilon_0^2 n^2} \qquad (1.1)$$

where μ is the reduced electron-hole mass, e is the charge of an electron, $\hbar$ is the reduced Planck constant, ε_o is the dielectric constant, and n is the integer excited state of the exciton. This leads to a solution for the exciton radius as well, where the exciton Bohr radius equals[70]

$$a_n = \frac{n^2 \hbar^2 \varepsilon_0}{\mu e^2} \qquad (1.2).$$

For zinc oxide, the exciton has a very high binding energy of 59 ± 1 meV, implying a small free exciton radius of 1.8 nm.[7]

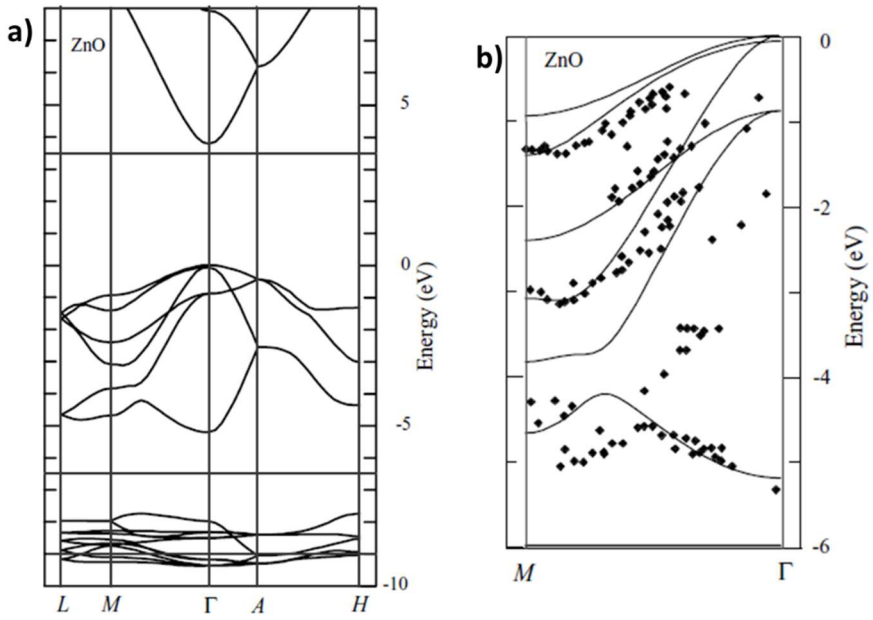

Figure 1.10: Local-density theory calculations of the ZnO band structure along different symmetry axis in momentum space.[71,72] a) The full band structure and b) the hole band structure near the gamma point, with overlapping experimental data.[73]

The number of hole bands in the band structure of ZnO determines how many ground state free-exciton transitions can exist. To determine the number of hole bands, the band structure of ZnO must be calculated and measured. Figure 1.10.a shows the theoretical calculation for the band structure of wurtzite ZnO, with an accurately calculated bandgap near 3.37 eV, while Figure 1.10.b shows the measured data for the hole band structure displayed on top of the theoretical data near the Γ-point.[71-73] The close up of the hole band indicates there are three overlapping bands near the valence band top, thus, there should be three exciton transitions to those bands.[71-73] There is a discrepancy between the experimental and theoretical

values which is attributed to the measured exciton energies being influenced by electronic relaxations.[71,72] In wurtzite ZnO, the conduction band for the excited state of the exciton and the three valence bands for the ground states of the exciton can be represented by the electron levels of zinc ($[Ar]3d^{10}4s^2$), oxygen ($[He]2s^22p^4$), or the combined bonding and antibonding orbitals of ZnO. The conduction band can be viewed as either the Zn empty 4s levels of Zn^{2+} (ionic binding) or the lowest antibonding sp^3 orbitals (covalent bonding).[7] Subsequently, the valence band is described by either the occupied 2p levels of O^{2-} or the highest bonding sp^3 orbitals.[7]

Finally, the splitting of the three hole bands at the ZnO valence band top in Figure 1.10.b is due not only to the usual spin-orbit coupling, but also by crystal field splitting due to the uniaxial crystal structure of ZnO.[7] Spin-orbit coupling is caused by the interaction of the particles spin with its motion, and crystal field splitting is caused by static electric field produced by the polarity of the wurtzite crystal along the *c*-axis. Unlike in a cubic crystal structure, where spin-orbit coupling dominates and the hole band splits into heavy holes and light holes (as crystal field splitting doesn't exist for cubic symmetries), in hexagonal structures the addition of the crystal field splitting leads to the hole band splitting into three non-degenerate levels, named A, B, and C.[7,71] Figure 1.11.a depicts the schematic band structure of ZnO near the Γ-point, showing the conduction band and the resulting three valence bands, A, B, and C. These correspond to three allowed exciton transitions, where A and B excitons are excited with polarizations perpendicular to the *c*-axis, and C excitons are excited with polarizations parallel to the *c*-axis.[7] Figure 1.11.b shows a schematic comparing the band-structure of wurtzite ZnO for three cases, that of only spin-orbit coupling, only crystal field splitting, and both combined, showing not only how the energy levels change, but also how the Γ-symmetry changes for each scenario.[7,74] However, without a stable bulk crystal of zinc blende ZnO, the ordering of the Γ-

symmetries of the A and B exciton in Figure 1.11.b are still controversial, as the crystal cannot be tested without the presence of crystal field splitting.[7] Low temperature reflectance spectra does detect all three exciton absorption lines, confirming the combined crystal field splitting and spin-orbit coupling model for the wurtzite ZnO band structure.[7,75] The room temperature UV emission of ZnO is the recombination of three free excitons, primarily the A-exciton, homogeneously broadened from scattering with phonon modes, as in Figure 1.9. The exciton binding energies of the A, B, and C excitons are approximately equivalent at 59 ± 1 meV.[7]

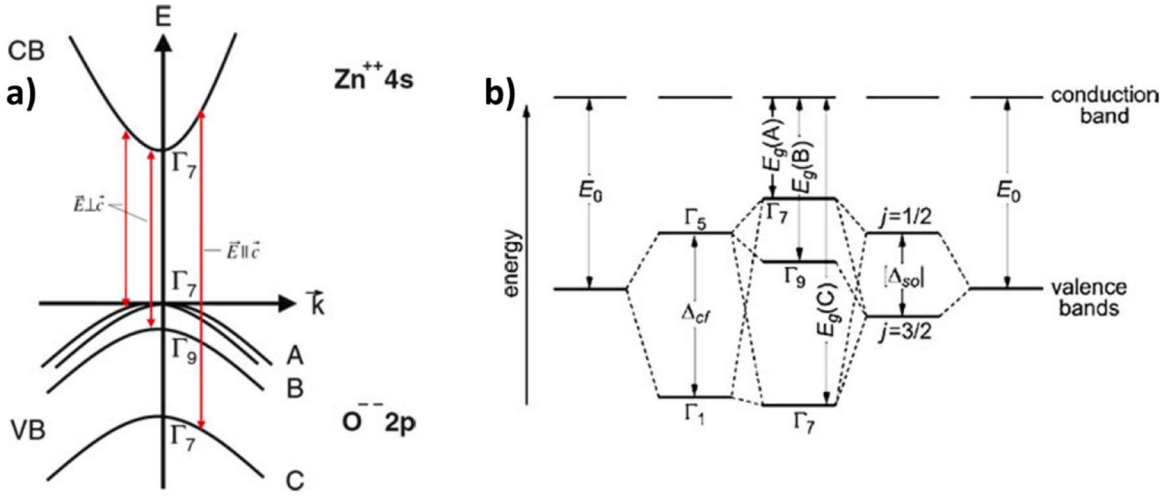

Figure 1.11: a) schematic drawing of the band structure of wurtzite ZnO in the vicinity of the Γ-point, showing the dipole allowed transitions of the A, B, and C excitons (corresponding to recombinations from the conduction band into the A, B, and C valence bands, respectively).[7] b) schematic energy level diagram of the valence band splitting of wurtzite ZnO due to crystal field splitting (cf), spin-orbit coupling (so), and the two combined, indicating the A, B, and C exciton transitions.[7,74]

1.3.2 ZnO Defect States

The broad visible emission in ZnO nanostructures, shown in Figure 1.9, is typically centered in either the green or yellow bands, depending on growth technique.[1,7] As it currently stands, the origin of these defect caused emissions, specifically the green emission, is a

controversial topic, assigned to defects, impurities, and even adsorbates. Figure 1.12 shows a to scale representation of the theoretically calculated defect levels for ZnO, showing the energies of charged and uncharged Zn vacancies, octahedral and tetrahedral zinc interstitials, neutral and charged oxygen vacancies, antisite oxygen, and interstitial complexes in the 3.37 eV bandgap.[1] However, the exact energies of each of these defect levels is inconclusive, as different studies do not predict the same energy levels for the same defects.[1] The difficulties in determining the exact defect energies may be caused by individual defect interactions, which are challenging to account for.[1] The defects in Figure 1.12 emit primarily from the deep defects, that of the oxygen and zinc vacancies, leading to the typical green emission at 520 nm and 540 nm.[1,76,77] A zinc to oxygen antisite defect has also been shown to emit at 520 nm.[1,78] Additionally, the yellow emission is typically from surface defects, centered at 560 nm.[1,79] These surface defects may have a stronger influence on the visible photoluminescence of ZnO nanostructures than bulk defects, due to quenching of the visible emission when a capping layer is introduced.[80-82]

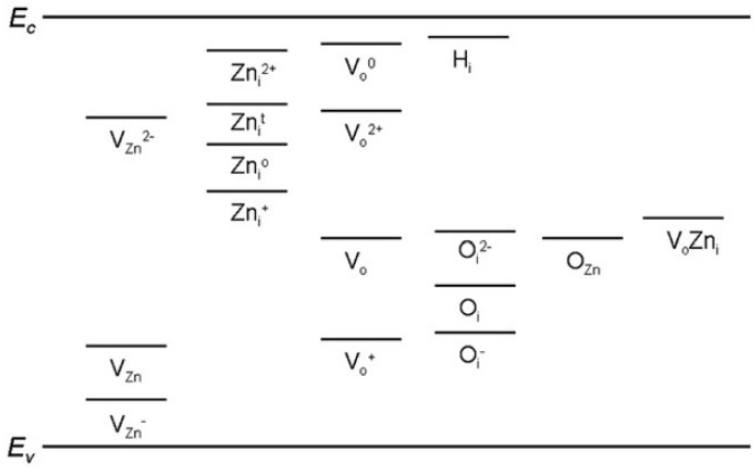

Figure 1.12: Calculated energy levels of different defects in ZnO (relative to the conduction band minimum) gathered from various literature studies by Djurisic, *et al*.[1] V = vacancy (Zn and O denoted by subscript), Zn = zinc interstitial, H = hydrogen interstitial, O = oxygen interstitial, O_{Zn} = antisite oxygen, and V_0Zn_i = an oxygen vacancy / zinc interstitial complex.

1.4 Plasmonics

1.4.1 Plasmon Overview

In metals, valence electrons are not bound, instead they move as a nearly free gas among their stationary ion cores. When these free electrons respond to an electromagnetic force, they oscillate locally according to the driving electromagnetic field. The collective excited states of the electrons form a quasiparticle called a bulk plasmon, with a plasma frequency,

$$\omega_p = \sqrt{\frac{4\pi e^2 N}{m^*}} \qquad (1.3),$$

dependent upon the charge e, number density N, and effective mass m^* of the electrons in the metal.[83] The plasma frequency also influences the optical properties of the metal, with the dispersion relation of the dielectric function, $\varepsilon(\omega)$, depending directly upon the metals plasma frequency, shown in Equation 1.4 with damping term γ.

$$\varepsilon(\omega) = \varepsilon_\infty - \frac{\omega_p^2}{\omega^2 - i\gamma\omega} \qquad (1.4)$$

While the bulk plasmon does not depend on the environment around the metal, for metal interfaces and nanoparticles, the surrounding dielectric environment has an influence on the plasmonic response. Surface plasmons form when a metal has an interface with a dielectric material and electromagnetic fields excite oscillations of the electron density at that interface. The propagation of the electromagnetic excitations along the interface is called a surface plasmon polariton. The surface plasmon polariton resonance frequency, ω_{sp}, depends not only on the plasma frequency of the metal, but also on the dielectric function, ε_d, of the interfacing material:[83]

$$\omega_{sp} = \frac{\omega_p}{\sqrt{1+\varepsilon_d}} \qquad (1.5)$$

A localized surface plasmon (LSP) is confined inside a nanostructure of a metal, oscillating in the nanoparticle without propagation. A localized electric field is created by the oscillating plasmon. The oscillation frequency of a LSP is dependent not only upon the properties of the metal and dielectric surroundings, but also the shape and size of the particle.[83] In the quasi-static limit for a sphere of volume *V* and complex dielectric function ε_m, the extinction cross section (a sum of absorption and scattering) is equal to[83]

$$C_{ext}(\omega) = 9\frac{\omega}{c}\varepsilon_m^{\frac{3}{2}} V \frac{\varepsilon_2(\omega)}{[\varepsilon_1(\omega)+2\varepsilon_m(\omega)]^2+\varepsilon_2^2(\omega)} \qquad (1.6),$$

where ω is the frequency, *c* is the speed of light, and ε_1 and ε_2 are the complex dielectric function of the surrounding environment. In an array of closely spaced metal nanoparticles, both LSPs and surface plasmon polaritons can be present, as the surface plasmon polariton can travel between particles without fully decaying if the interparticle spacing is small enough.[83]

1.4.2 Plasmon-Exciton Coupling

Plasmon-exciton coupling has become an attractive way to control and amplify the emission of a semiconductor material.[28,29,62,84] When a semiconductor and plasmonic material are in proximity and the plasmon is resonant with the emission of the semiconductor, the dipole emitter can couple with the metal plasmons, enhancing the emission. This enhancement is attributed to the Purcell effect, which is the enhancement of the spontaneous emission rate of a material due to a change its environment, i.e. from the presence of a resonant cavity.[85] For the

spontaneous emission enhancement in a resonant microcavity with high quality factor Q and ultrasmall mode volume V, the Purcell factor is[86]

$$F_p = \frac{3}{4\pi^2}\left(\frac{\lambda_c}{n}\right)^3 \frac{Q}{V}, \qquad (1.7)$$

where $\frac{\lambda_c}{n}$ is the wavelength in the medium. High Q-factor resonators have smaller bandwidths and lower damping leading to lower rates of energy loss, while small V resonators can localize the mode. Plasmonic nanoparticles lead to high intensity and localized electric fields near the nanoparticle surface, creating plasmonic resonant cavities with ultrasmall mode volumes. While the quality factor in a plasmonic cavity typically has absorption and radiative losses, the V can be confined to the nanoscale, leading to high Purcell factors and radiative emission enhancement.[86]

Another way to determine the Purcell factor for a resonantly coupled system is to compare the radiative emission rate of the emitter before and after coupling to the plasmonic system[28]

$$F_p = 1 + \frac{\Gamma_p}{\Gamma_0} \qquad (1.8)$$

where $\frac{\Gamma_p}{\Gamma_0}$ is the change in radiative transition rate (with respect to the non-radiative transition rate), of the plasmonic system in comparison to the non-plasmonic system. The radiative transition rate for a material is described by Fermi's Golden Rule #2:

$$\Gamma_{p,0} = \frac{2\pi}{\hbar}\left|\langle f|\hat{H}_{int}|i\rangle\right|^2 \rho(\hbar\omega) \qquad (1.9)$$

where $\left|\langle f|\hat{H}_{int}|i\rangle\right|^2$ is the matrix element of the dipole transition from excited to ground state due to the purturbing electricmagnetic field, and $\rho(\hbar\omega)$ is the joint density of states of the carriers.[28,87] The majority contribution to the joint density of states in the plasmon-exciton

coupled system is the plasmon density of states, as there are orders of magnitude more free electrons in a metal than in a semiconductor excited state. This greatly increased density of states provided by the plasmons in turn increases the spontaneous transition rate of the dipole emitter, resulting in an enhanced radiative emission and reduced non-radiative losses.

1.5 Chapter Outline

Chapter 2: Zinc oxide nanowire and nanostructure fabrication. A high-temperature modified vapor-solid method allows for a wide variety of nanostructures to be grown, while a low temperature hydrothermal method grows consistent, vertically oriented, "carpet" nanowires, given an epitaxial substrate. The hydrothermal method for growing vertically-oriented nanowires provides the most consistent nanowire growth between different depositions. Also discussed is the analysis of nanostructure uniformity and crystallinity along with subsequent techniques for coating nanowires in cladding layers and nanoparticle films.

Chapter 3: The UV photoluminescence enhancement of randomly oriented ZnO/MgO core-shell nanowires coated with Ag nanoparticles is presented. The results of photoluminescence, mode-calculations, finite element simulations, and numerical analysis show the coupling of the ZnO near-band-edge exciton emission to Ag localized surface plasmons and additional optical cavity effects due to ZnO/MgO core-shell nanowires. These point to efficient UV emission from ZnO nanowires for optoelectronic and optical applications.

Chapter 4: The plasmon-exciton coupling from Chapter 3 is studied further, using cathodoluminescence to analyze the radiative emission from plasmons and excitons in the Ag coated ZnO/MgO nanowires. This collaboration with Oak Ridge National Lab also led to a

novel complementary spectroscopy technique to study the random morphology Ag nanoparticles coating the nanowires, identifying their three dimensional plasmon modes. This leads to a better understanding of the complex plasmon modes present in the coated nanowires.

Chapter 5: The effect of the interface quality of ZnO/MgO core-shell nanowires on the ZnO band-edge emission photoluminescence enhancement is explored. Processing the ZnO nanowires under low oxygen partial pressure leads to an MgO-thickness-dependent PL enhancement due to the formation of optical cavity modes. Conversely, processing under higher oxygen partial pressure leads nanowires that support neither mode formation nor band-edge PL enhancement. Photoluminescence spectroscopy, high-resolution electron microscopy, density-functional calculations, and finite element simulations are combined to study the complex mechanisms at play. These results point the way to fabricating optical cavity mode enhanced nanowires for more efficient UV nanolasers, scintillators, and sensors.

Chapter 6: The effects of nanostructure morphology on the UV optical properties of ZnO are elucidated. Vapor-solid and hydrothermal nanowires, along with a novel nanostructure, christened "nanopopcorn," are studied. In temperature dependent PL and Raman spectroscopy experiments, the nanopopcorn are found to have the most defects, while the vertically oriented "carpet" ZnO nanowires have the fewest. Thus the carpet nanowires are the ideal structure for moving forward towards nanolasing applications in a vertical nanowire cavity.

Chapter 7: This chapter presents two applications of the vertically oriented "carpet" ZnO nanowires, using plasmon-exciton coupling to enhance the UV band edge emission of nanowire devices. The first application is that of plasmon enhanced UV light-emitting diodes. The second application is UV nanolasing in ZnO nanostructures, where vertically-oriented nanowires can support a Fabry-Perot lasing cavity, and nanopopcorn could support random lasing. Coating

these structures in metal nanoparticles will enable studies of plasmon-exciton coupling in ZnO lasing, moving toward enhanced UV lasing in on-chip devices.

CHAPTER 2

ZINC OXIDE NANOSTRUCTURE FABRICATION

This chapter discusses all of the ZnO fabrication techniques used to build nanostructures in this dissertation. Characterization techniques done as a part of fabrication to confirm properties of the materials, such as scanning electron microscopy (SEM), x-ray diffraction (XRD), transmission electron microscopy (TEM), scanning transmission electron microscopy (STEM), energy dispersive x-ray spectroscopy (EDS), and extinction spectroscopy, are also discussed in this chapter. All TEM, STEM, and STEM-EDS measurements in this chapter and beyond (excluding Chapter 4), were done by Dr. James McBride. The majority of the fabrication processes in Section 2.1 and 2.2 have been published in Mayo *et al*,[31] Zhang *et al*,[21] Hachtel *et al*,[30] Cook *et al*,[38] and Marvinney *et al*.[32] A paper describing the fabrication processes in Section 2.1.4 is in preparation (along with the work in Chapter 6) for submission.

2.1 Vapor-Solid Growth

This section discusses the methods for growing randomly oriented nanowires using a modified vapor-solid technique. These randomly oriented nanowires are used for experiments in Chapters 3 - 6. Next, this section defines the parameters of the low oxygen-pressure (LOP) and high oxygen-pressure (HOP) protocols employed to fabricate Ag coated ZnO/MgO core-shell nanowires[30-32] for experiments presented in Chapters 3 - 5. Finally, the protocol for nanopopcorn growth using the modified vapor-solid method is expounded for studies done in Chapter 6.

Figure 2.1 gives an overview of the modified vapor-solid growth chamber used for growing randomly oriented ZnO nanowires and nanopopcorn. The rest of Figure 2.1 depicts the process of imaging of the nanowires to determine their morphology, and subsequent depositions of the MgO films and Ag nanoparticles using electron beam evaporation. Descriptions of each of these techniques and the basic characterization of the samples follow.

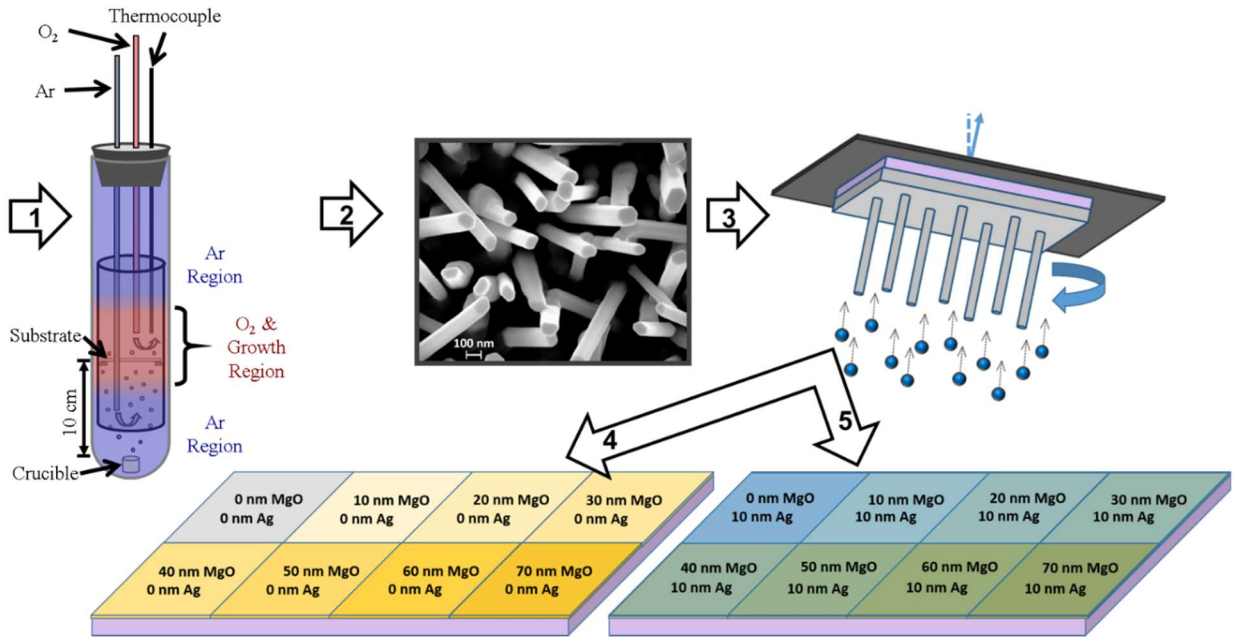

Figure 2.1: Fabrication procedure for Ag coated, ZnO/MgO core-shell nanowires. Step 1: electron beam deposition of a ZnO seed layer on a fused silica substrate. Step 2: modified vapor-solid growth of ZnO nanowires onto the substrate. Step 3: scanning electron microscopy mapping of nanowires to determine sample uniformity. Step 4: glancing-angle electron beam deposition of MgO onto the nanowire sides. Step 5: glancing-angle electron beam deposition of Ag nanoparticles onto the nanowire sides.

2.1.1 Vapor-Solid Nanowire Growth Development

For all modified vapor-solid ZnO nanowires, the substrates were 100 nm ZnO seed layers deposited on 500 μm thick fused silica (dimensions of approximately 1 cm x 2 cm). To coat the

ZnO seed layers, the samples were first cleaned of organics by sonication with acetone, methanol, and deionized water, and then dried with compressed nitrogen gas. Then, the 100 nm thick ZnO seed layer was deposited by electron beam evaporation (Thermionics, 150-0040, 3000 W maximum power), the first step in Figure 2.1. A base pressure of $4x10^{-4}$ Pa was reached before deposition to minimize contamination. An operating pressure of less than $4x10^{-3}$ Pa was maintained at a deposition rate of 0.1 Å/s; the deposition rate was measured by a quartz crystal microbalance to verify coating thicknesses.

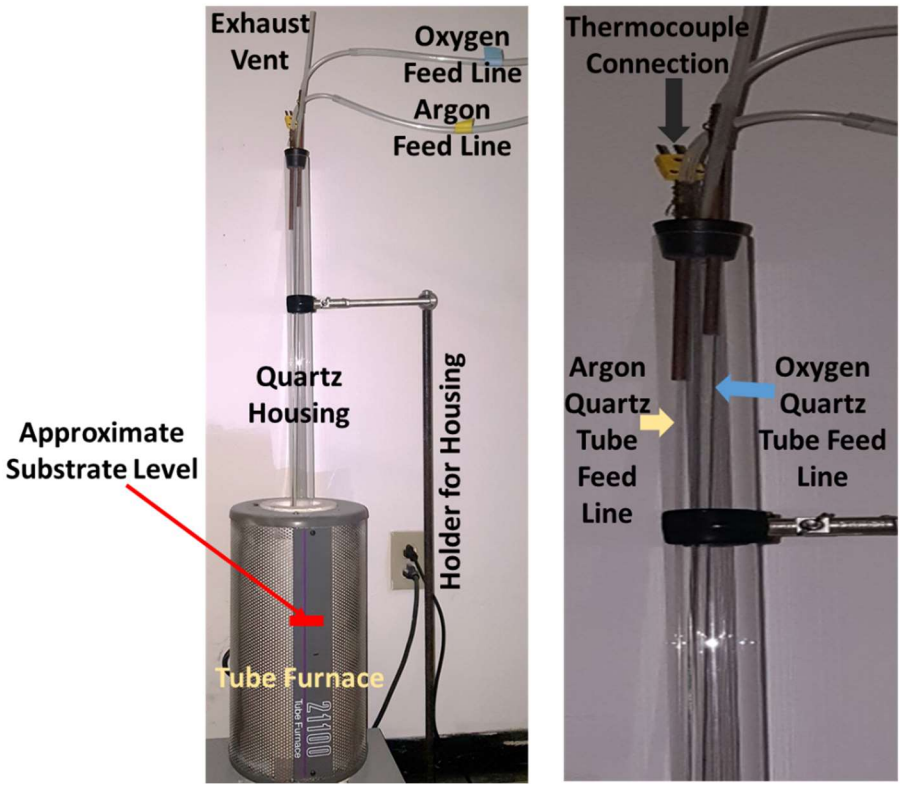

Figure 2.2: The vapor-solid growth lab, showing the tube furnace, quartz housing, gas feed lines outside and inside the quartz housing, exhaust vent, thermocouple connector (which goes down to the substrate level), and the approximate substrate level in the system. In these images the position of the argon and oxygen quartz feed lines are not stabilized/controlled.

The ZnO nanowires were then grown on the ZnO seed layer. This step in the growth process utilized a modified vapor-solid method, using a vertically-oriented tube furnace (Thermolyne 21100), Figure 2.2. A vertically-oriented quartz tube was used to support the substrate and gas feed lines during deposition, depicted in Figure 2.1, step 2, and Figure 2.2. A measured amount (6.0 mg) of Zn powder was placed into a crucible mounted at the bottom of the 0.9 m tall quartz tube housing. The substrate was situated on two silicon shelves in the substrate holder, and a protective fused silica slide was placed on the non-seed layer side of the substrate to prevent unwanted ZnO growth on the backside of the substrate. The substrate holder positioned the substrate approximately 10 cm above the crucible. Gas feed lines for Ar and O_2, an exhaust vent, and a thermocouple connection were fed into the growth tube, Figure 2.2, with the O_2 line and thermocouple directly above the substrate, and the Ar line between the substrate and crucible, as shown in the Figure 2.1, step 2 schematic.

An initial pre-growth time period (pre-growth 1) was used to purge the chamber of ambient air using a high Ar flow rate of 750 – 1000 sccm. This also prevented the O_2 from reaching the surface of the substrate until the desired temperature was reached in the chamber. After purging, the quartz tube was transferred directly from the room temperature environment to the vertical furnace, which was preheated to 700 °C, causing the temperature in the furnace to drop before rising back to 700 °C over the course of the growth. In order to initiate the Zn and O_2 reaction, causing ZnO growth, the Ar pressure was lowered (at a second pre-growth time, pre-growth 2), allowing the desired O_2 partial pressure to reach the substrate, as noted by the red O_2 zone in Figure 2.1, step 2. Waiting to lower the Ar pressure until the desired chamber temperature was reached allowed the evaporated Zn particles time to travel to the level of the substrate before the O_2 was introduced. During the growth period, zinc oxide

nanowires/nanostructures form on the substrates by preferentially nucleating from grains on the ZnO seed layer. After exhausting the Zn source, the quartz tube was removed from the vertical furnace and the sample was allowed to cool under ambient conditions.

To verify the morphology of the nanostructures that had grown on the substrates, each sample was viewed by scanning electron microscopy (SEM) (Hitachi, S-4200, Raith eLine, Zeiss Merlin with Gemini II column). Images were taken in both the plan view and 45˚ tilt configurations on multiple locations of a sample to gauge the uniformity of the growth, identifying if there was uniform nanowire growth, or growth of other nanostructures, as in Figure 2.3. The growths with desired results form nanowires that are uniform in size and spacing, albeit randomly oriented, as shown in Figure 2.3.d,h.

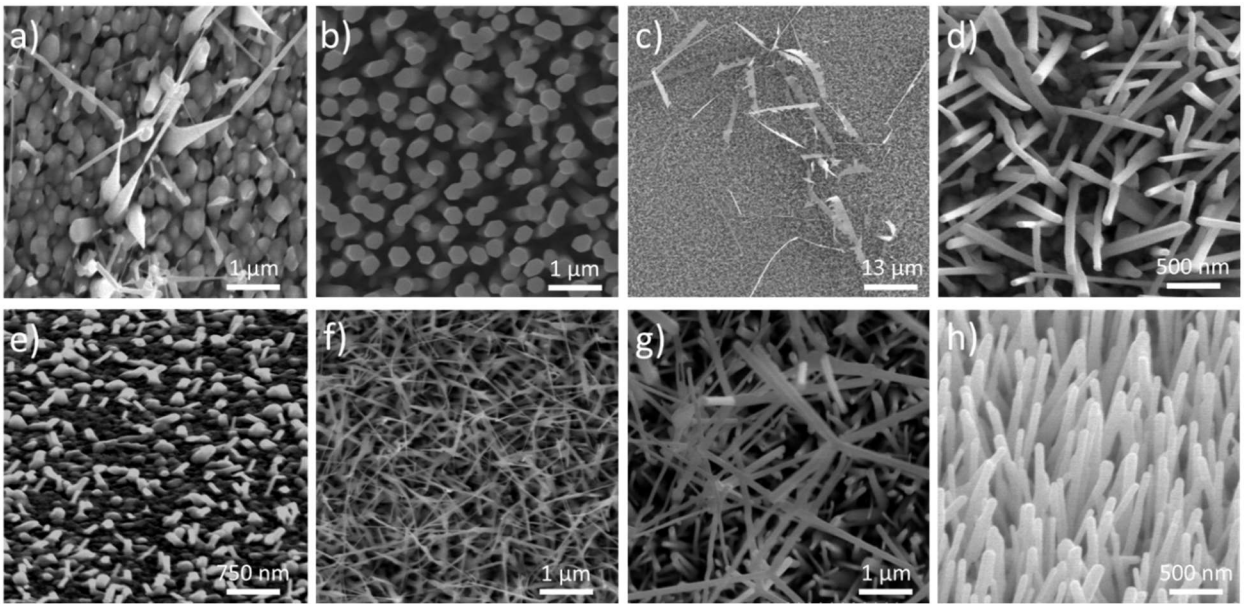

Figure 2.3: Scanning electron micrographs of undesirable (a-c, e-g) and desirable (d, h), ZnO nanostructures. Nanostructures imaged are a) sparse nanoneedles, b) dense nanopillars, c) nanosheets on top of nanowires, d) uniform nanowires, e) sparse nanostubs, f) thin nanoneedles nests, g) tetrapods on top of nanowires, and h) uniform nanowires.

The growth of randomly oriented ZnO crystals was verified by x-ray diffraction measurements (XRD) and transmission electron microscopy (TEM). For all TEM studies (Tecnai Osiris, 200 keV), each sample was prepared by pressing a lacy carbon TEM grid directly onto the nanowires, resulting in a transfer of nanowires from the substrate to the TEM grid. Figure 2.4 shows a TEM micrograph of a typical ZnO nanowire, indicating the *c*-axis direction of crystal growth along the long-axis of the nanowire. Figure 2.5 shows an XRD spectrum for a typical vapor-solid nanowire sample, highlighting the multiple ZnO crystal orientations visible (Joint Committee on Powder Diffraction Standards: JCPDS number 36-1451), because the grains in the ZnO seed layer are also in random orientations.

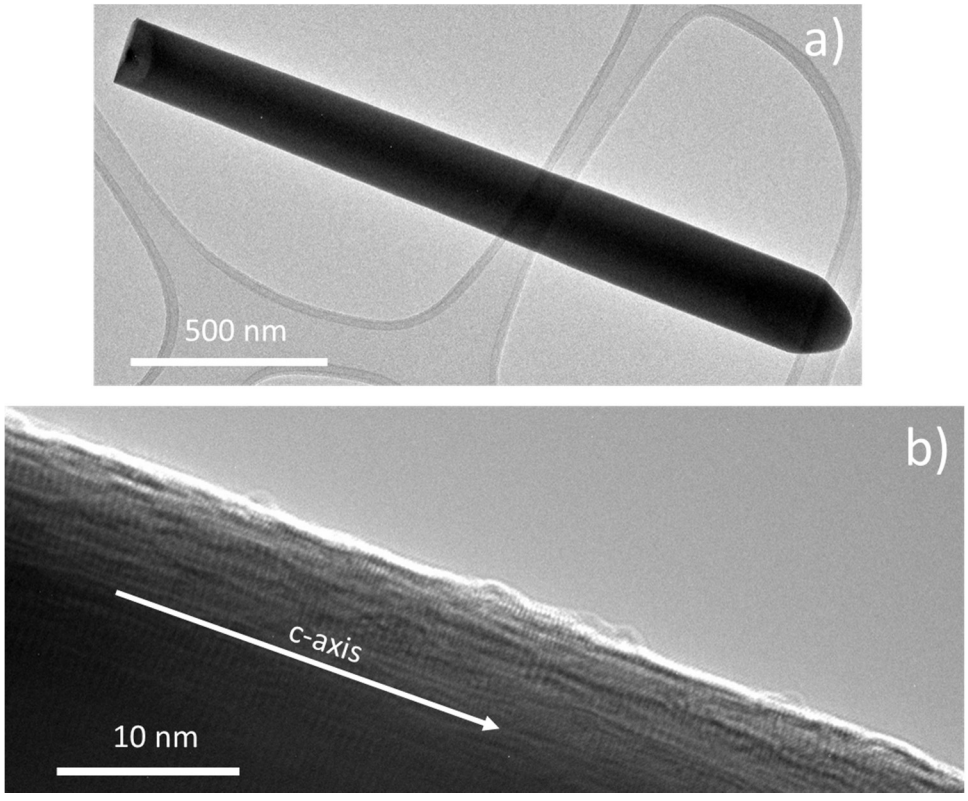

Figure 2.4: Transmission electron micrographs of a typical vapor-solid growth ZnO nanowire, a) micrograph showing the entire nanowire and b) high-resolution micrograph indicating the *c*-axis growth direction perpendicular to the (0001) lattice planes.

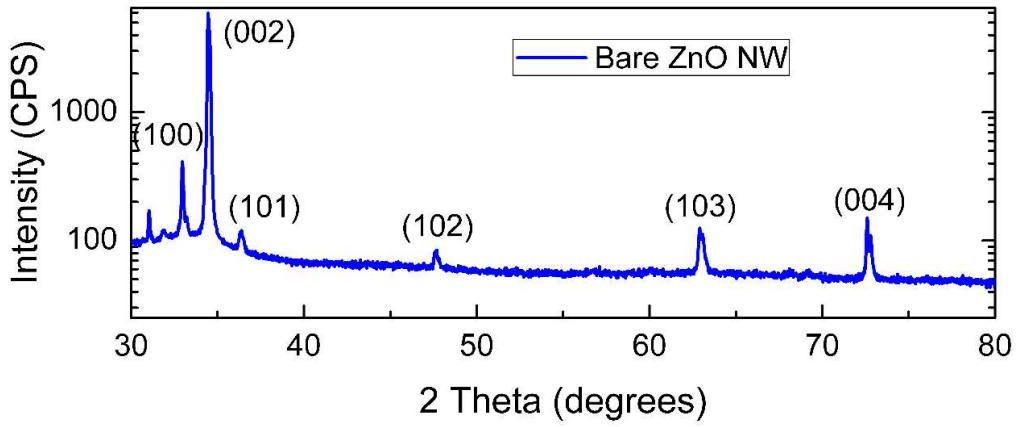

Figure 2.5: XRD 2 theta scan of a typical randomly oriented ZnO nanowire sample.

Table 2.1: Growth parameters used for the various ZnO nanostructures in Figure 2.2.

Figure/ Nanostructure	Date	Total Flow Rate (sccm)	Oxygen Partial Pressure (%)	Oxygen Tube Position	Pre-Growth Time 2 (min)	Initial Growth Temperature (°C)	Total Growth Time (min)
2.1.a Sparse nanoneedles	01/09/14	379	7.7	Uncontrolled	5	600	12
2.1.b Dense nanopillars	02/02/15	378.4	7.5	Centered	0	300	16
2.1.c Nanosheets on nanowires	05/15/14	428.6	7.0	Uncontrolled	4	525	10
2.1.d Uniform nanowires	05/31/13	373	6.2	Uncontrolled	5	600	12
2.1.e Sparse nanostubs	06/07/13	369	5.2	Uncontrolled	5	600	12
2.1.f Thin nanoneedles	05/15/14	270.0	10.0	Uncontrolled	4	525	12
2.1.g Tetrapods on nanowires	02/09/15	378.4	7.5	Centered	0	300	16
2.1.h Uniform nanowires	10/06/14	378.4	7.5	Uncontrolled	4	525	12

A sweep was performed on the vapor-solid growth parameters, in order to optimize uniform nanowire growth (Figure 2.3.d,h) over that of other structures (Figure 2.3.a-c,e-g). The

parameters that were studied are as follows: total chamber flow rate, oxygen partial pressure, oxygen tube position (centered or sidewall of apparatus versus no control), time-into-growth and temperature of oxygen introduction (pre-growth time 2, initial growth temperature), and total growth time. Table 2.1 presents the growth conditions of each of the nanostructures grown in Figure 2.3, to demonstrate the range of parameters that were studied. The nanowires grown in Figure 2.3.h (parameters in Table 2.1), were used in Chapter 6.

2.1.2 LOP versus HOP Nanowire Growth

Table 2.2 Growth protocols for the modified vapor-solid ZnO nanowire growth method used for the LOP and HOP nanowires in Chapters 3 – 5.

	Parameters	**LOP: Lower Oxygen Pressure**	**HOP: Higher Oxygen Pressure**
Pre-Growth 1:	Zinc Source (mg)	6.0	6.0
	Time (min)	8	4
	Temperature (°C)	300	300
	Argon (sccm)	1000	800
	Oxygen (sccm)	23	28.4
	Oxygen (%)	2.25	2.76
Pre-Growth 2:	Time (min)	5	0
	Initial Temperature (°C)	300	----
	Final Temperature (°C)	600	----
	Argon (sccm)	1000	----
	Oxygen (sccm)	23	----
	Oxygen (%)	2.25	----
Growth:	Time (min)	12	16
	Initial Temperature (°C)	600	300
	Final Temperature (°C)	700	700
	Argon (sccm)	350	350
	Oxygen (sccm)	23	28.4
	Oxygen (%)	6.2	7.5

Sometimes a set of parameters did not result in consistent nanostructure growths, as in Table 2.1. Over time, two different growth protocols were developed that most consistently grew the desired randomly oriented ZnO nanowires using the vapor-solid method. These two protocols are outlined in Table 2.2. The low oxygen partial pressure (LOP) method was developed initially, using analog flow meters (Omega, 87 sccm O_2, 2200 sccm Ar) to control the flow of the oxygen and argon gases. The high oxygen partial pressure (HOP) method was developed after the purchase and installation of digital mass flow controllers (MKS, 100.0 sccm O_2, 1000.0 sccm Ar), by sweeping the parameters discussed above. The mass-flow controllers allowed for a more constant control the total chamber flow rate and the oxygen partial pressure than the analog system. The HOP protocol is the best result of the parameter sweep, as it allowed the highest proportion of growths to produce the desired nanowires. The desired nanowires had a diameter of 70 – 100 nm, a uniform spacing of around 200 – 400 nm, and were uniform in length (lower bound 700 nm, depending on growth time).

As in Table 2.2, during the pre-growth phase of the LOP and HOP protocols, Ar was initially held at a high flow rate to purge the system of ambient air and prevent the O_2 from reaching the surface of the substrate. The quartz tube was transferred to the tube furnace as before, however, the lowering of the Ar pressure, and thus initiation of ZnO growth, occurred at different temperatures for the two protocols. For the LOP protocol, the Ar pressure was lowered only after the temperature in the chamber had risen to 600 °C, which occurred five minutes after the vertical chamber was placed in the tube furnace. Thus the Zn vapor migrated to the level of the substrate before the O_2 was introduced. For the HOP protocol, the Ar pressure was lowered when the vertical chamber was first introduced to the tube furnace, now allowing the O_2 to reach the substrate before the Zn vapor and thus reversing the order in which the Zn and O_2 reached the

substrate. The second notable difference between the two protocols is the oxygen partial pressure, for which the protocols are named. The LOP protocol used a low, 6.2 % oxygen partial pressure, while the HOP protocol used a higher, 7.5 % oxygen partial pressure. As always, after exhausting the Zn source, the quartz tube was removed from the vertical furnace and the sample was allowed to cool under ambient conditions.

2.1.3 Ag and MgO Coated LOP and HOP Nanowires

Before overcoating of shell materials or nanoparticles, the samples that showed desirable, uniform nanowires were imaged again with SEM, this time to determine the uniformity of the nanowires across the sample surface area; this produced an SEM sample map. This step is identified in Figure 2.1, step 3. Images for SEM sample maps were taken every 3-5 mm along a sample. Figures 2.6 shows an SEM sample map of the LOP sample used for experiments in Chapter 3 - 5. Figure 2.7 shows an SEM sample map of the HOP sample used for experiments in Chapter 5. The nanowire diameter (*d*), interwire spacing (*IS*), and nanowire length (*l*) were measured using ImageJ software for each SEM image in a sample. From these measurements, averages and standard deviations were determined for *d*, *IS*, and *l* for the total sample, as well as the average percent root mean square deviation (RMSD) of *d*, *IS*, and *l* for each micrograph from the total average for the sample. The RMSD is defined as

$$RMSD = \frac{1}{n}\sqrt{\sum_{i=1}^{n}(\hat{x} - x_i)^2} \qquad (2.1),$$

where x_i is the average measurement for an individual SEM image *i*, $\hat{x}$ is the average value for all the images in the array for the entire sample, and $n = 8$ micrographs for the LOP nanowires and 15 for the HOP nanowires. The average percent RMSD is defined as $RMSD\ (\%) = \frac{RMSD}{\hat{x}} \times$

100. Table 2.3 presents the calculated data for *d*, *IS*, and *l* for the LOP and HOP samples used for MgO thickness dependent studies in Chapter 3 and Chapter 5.

Table 2.3: Analysis of the uniformity of bare ZnO nanowires for the LOP nanowire sample and HOP nanowire sample used for experiments in Chapter 3 and Chapter 5.

	LOP Nanowires	**HOP Nanowires**
Average Length[a] [nm]	911 ± 203	1476 ± 193
Length RMSD[b] [%]	14	6
Average Diameter [nm]	93 ± 19	91 ± 20
Diameter RMSD [%]	5	5
Average Interwire Spacing [nm]	304 ± 125	333 ± 129
Interwire Spacing RMSD [%]	9	10

[a)]Average and standard deviation of the entire sample map [b)] RMSD = root mean square deviation of the average from an individual SEM image to that of the total average, averaged from image i = 1-n, as given in Equation 2.1.

After the sample maps were created and statistics for the nanowires determined, the nanowires were coated with the MgO shell. A glancing-angle electron beam deposition technique was used to coat the MgO shell, as depicted in Figure 2.1, step 4. The electron beam evaporation used was a Thermionics 150-0040, with 3000 W maximum power. A base pressure of $4x10^{-4}$ Pa was reached before deposition to minimize contamination. An operating pressure of less than $4x10^{-3}$ Pa was maintained at a deposition rate of 0.1-0.2 Å/s. The glancing angle technique allowed for the continuous rotation of the substrate in the electron-beam deposition chamber at a calculated angle in order to uniformly coat the sides of the nanowires. The average nanowire length *l* and interwire spacing *IS* were used to determine the required sample angle

during the glancing angle deposition. Minimum shadowing occurs at the inverse tangent of the interwire spacing divided by the nanowire length,

$$\alpha = \tan^{-1}\frac{IS}{l} \qquad (2.2).$$

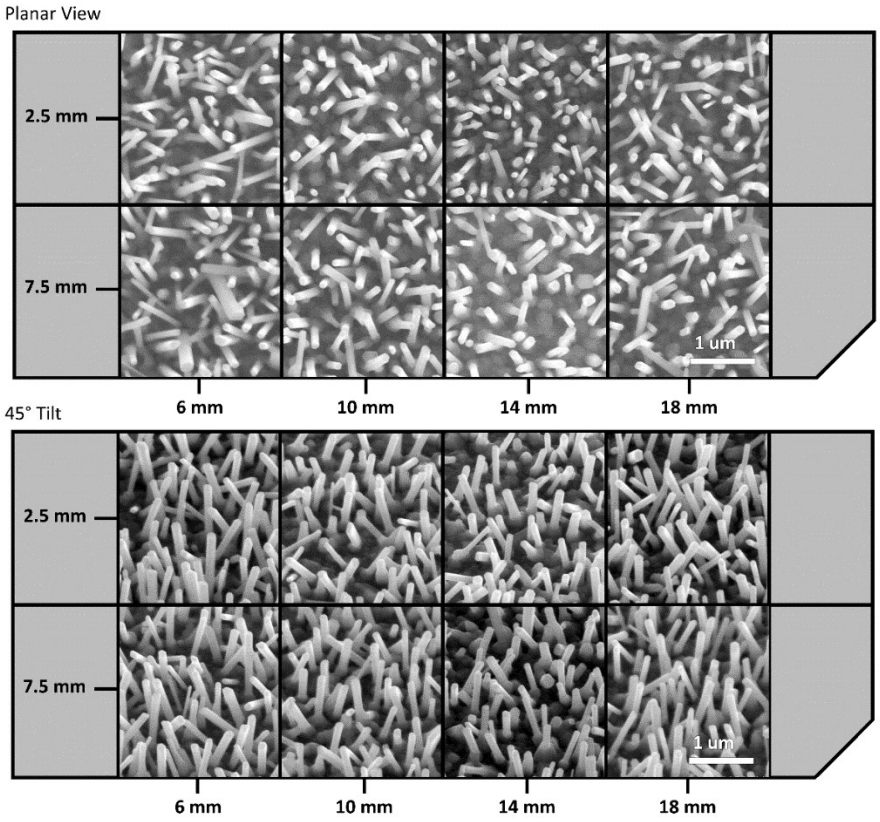

Figure 2.6: Scanning electron microscopy sample map of the LOP sample used for experiments in Chapters 3 – 5.

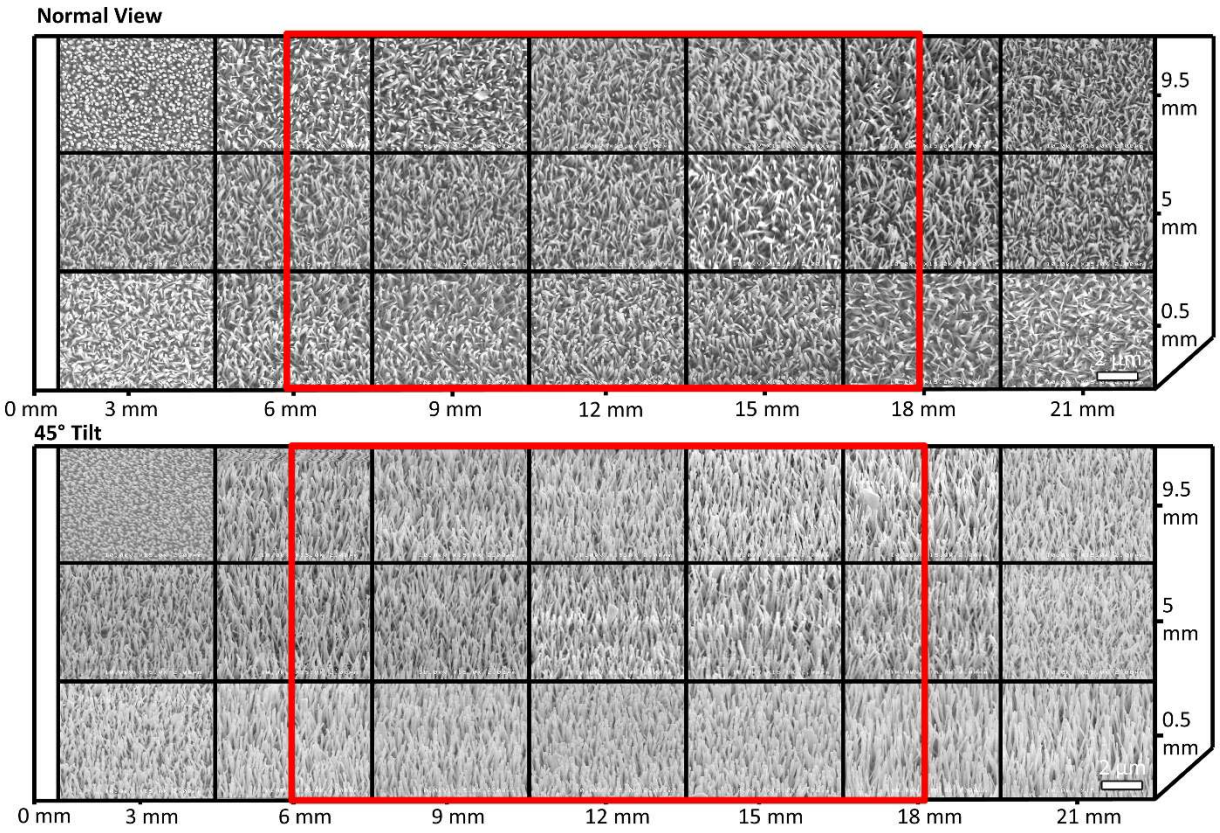

Figure 2.7: An SEM sample map of the HOP nanowires discussed in Chapter 5. The red boxed region was coated in MgO and used for the photoluminescence study. Outside the boxed region the nanowires were not uniform.

Two samples were fabricated in order to study the effects of varying the MgO thickness on the ZnO photoluminescence, as in Chapter 3[31] and Chapter 5.[32] The LOP (for both chapters) and HOP (for Chapter 5 only) samples each had eight MgO thickness regions, from 0 – 70 nm MgO in 10 nm increments. Prior to each glancing angle electron beam deposition of MgO, a mask with a 3x3 mm^2 slot was moved to a new section of the sample. This method was repeated seven times per sample, making a matrix of eight MgO regions. The thickness on the sides of the nanowires was measured with a quartz-crystal microbalance (QCM), with a deposition rate of 0.1-0.2 Å/s. Photoluminescence characterization of the samples was performed before any further depositions on the samples, and those measurements are discussed in the results sections

of Chapters 3 and 5. Extinction spectra were also acquired before further depositions, using a spectrophotometer (Hitachi U-3501) with an attached integrating sphere. Figure 2.8 shows the MgO coated ZnO nanowire extinction spectra for the LOP and HOP samples discussed in Chapter 3 and 5. The distinct ZnO band-edge absorption edge at a wavelength of 380 nm is visible in for both the LOP and HOP samples.

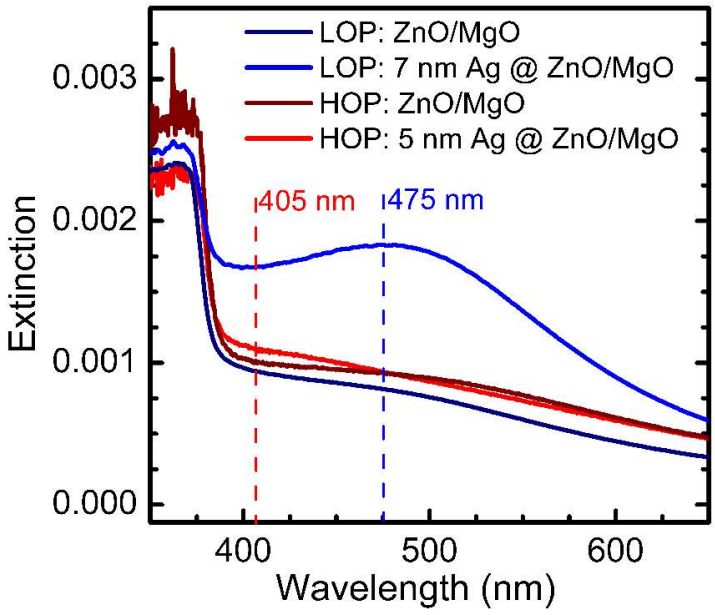

Figure 2.8: Extinction spectra (absorption + scattering) of the LOP and HOP nanowire samples for experiments in Chapters 3 - 5, before and after coating with Ag nanoparticle films. The blue (LOP) and red (HOP) dashed lines indicated the locations of the highest change in extinction between the Ag coated and uncoated samples.

A silver nanoparticle coating was deposited using the same glancing-angle electron beam deposition technique that was used for the MgO coating. For Chapters 3 - 5, the entire LOP sample was overcoated with a nominal 10 nm silver nanoparticle film, with the thickness monitored by a QCM. For Chapter 5, the HOP sample was also overcoated with Ag nanoparticles, this time with a nominal 3 nm silver nanoparticle film. Once the nanowires were

decorated with Ag nanoparticles, the extinction and PL spectra were again measured. The extinction spectra for the Ag coated samples is also given in Figure 2.8. The maximum difference in extinction due to the addition of the Ag nanoparticles is noted for each sample, indicating the localized surface plasmon resonance (LSPR). The maximum change in extinction is a factor of ten different between the two samples, Table 2.4, and the LSPRs are at 475 nm and 405 nm for the Ag nanoparticles on the LOP and HOP nanowires, respectively.

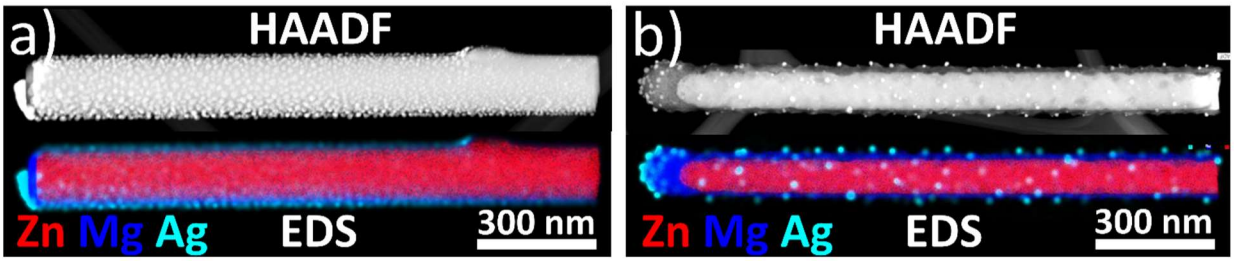

Figure 2.9: Scanning transmission electron microscopy high-angle annular dark field (HAADF) and energy dispersive x-ray spectroscopy (EDS) micrographs of an Ag coated ZnO/MgO core-shell a) LOP nanowire and b) HOP nanowire.

Scanning transmission electron microscopy (STEM) high-angle annular dark field imaging (HAADF), and STEM energy dispersive x-ray spectroscopy (EDS) (Tecnai Osiris, 200 keV) were used to determine the uniformity of the MgO coating, and the size and uniformity of the Ag nanoparticles. The samples was prepared for the transmission electron microscope (TEM) by pressing a lacy carbon TEM grid directly onto the sample. This resulted in a transfer of nanowires from the substrate to the grid. Figure 2.9.a-b show HAADF and EDS micrographs for nanowires grown by the LOP and HOP protocols, respectively. In nanowires grown under both LOP and HOP ZnO growth protocols, the MgO formed a uniform thickness coating along the long axis of the nanowire. A thicker MgO coating is found on the top facet of each

nanowire, typical of glancing angle deposition. The Ag nanoparticles also formed a uniformly distributed layer along the nanowire length, with the LOP nanowires (10 nm nominal coating thickness) having a much greater surface coverage than the HOP nanowires (3 nm nominal coating thickness). Again, the size of the Ag nanoparticles was larger on the top of the nanowires than on the sides, due to the glancing angle deposition technique.

Table 2.4: Ag nanoparticle coating on the LOP and HOP ZnO/MgO core-shell nanowires.

Ag Nanoparticles	**LOP Sample**	**HOP Sample**
Nominal Deposition Thickness (nm)	10	3
Nanoparticle Diameter on Nanowire Sides (nm)	7.2 ± 1.8	5.0 ± 1.4
Nanoparticle Diameter on Nanowire Tops (nm)	23.1 ± 4.3	7.0 ± 1.0
Nanoparticle Coverage (%)	68	6
Δ Extinction at LSPR	10^{-3}	10^{-4}
LSPR Wavelength (nm)	475	405

Next, the STEM HAADF images were used to analyze the size of the Ag nanoparticles. The average diameter and standard deviation of the nanoparticles on the tops of the nanowires and the sides of the nanowires were determined, as well as the percent coverage of the nanoparticles on the surface of the nanowires, Table 2.4. The nanoparticles on the sidewalls of the LOP and HOP nanowires are of comparable diameters, that of 7 nm and 5 nm, respectively. However, the difference in deposition thickness did significantly change the nanoparticle size on the tops of the nanowires between the LOP and HOP samples, to that of 23 nm and 7 nm, respectively. Additionally, the coverage of Ag nanoparticles along the length of the nanowires also changed significantly to almost 70 % coverage for the Ag nanoparticless on the LOP nanowires versus the 6 % coverage for the Ag nanoparticless on the HOP nanowires - an order of

magnitude different. This difference in nanoparticle coverage accounts for the order of magnitude difference in the plasmon resonance extinction between the two samples. Chapter 3 – 4 discusses the Ag nanoparticles on the LOP nanowires in more detail.[30,31] Chapter 5 briefly discusses the Ag nanoparticles on the HOP nanowires.[32]

2.1.4 Nanopopcorn

All previous vapor-solid growths, and thus the resulting nanostructures and nanowires, had the same substrate, a 100 nm ZnO seed layer on a fused silica substrate. In order to grow vertically-oriented "carpet" nanowires, however, the substrate beneath should have the preferred growth orientation, so that the nanowires will grow epitaxially from the substrate.[64] New substrates were acquired, consisting of a 5 cm wafer of a *c*-axis GaN film on *c*-axis sapphire. These substrates were tested with the vapor-solid technique, and thus were cleaved into 1x2 cm rectangles that fit into the vertical tube furnace sample holder.

For this vapor-solid growth, the HOP nanowire parameters were used (shown in Table 2.2). A uniform white growth appeared on the samples after they were removed from the vertical chamber, and were imaged to determine the morphology of the samples using the Merlin SEM. Surprisingly, no nanowires grew on any samples. Instead, the *c*-axis GaN film on sapphire promoted the growth of a novel nanostructure, here christened "nanopopcorn," for its free-form, highly porous morphology. Sample SEM maps, as previously described in Section 2.1.2, showed uniform growth of the nanopopcorn across the sample. Figure 2.10 depicts typical SEM images of the ZnO nanopopcorn.

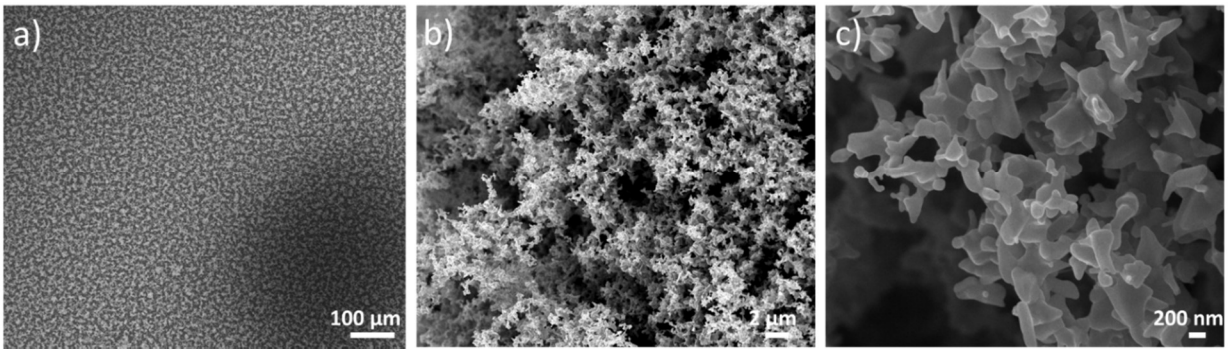

Figure 2.10: Typical SEM images of the ZnO nanopopcorn, a) – c) at different length scales.

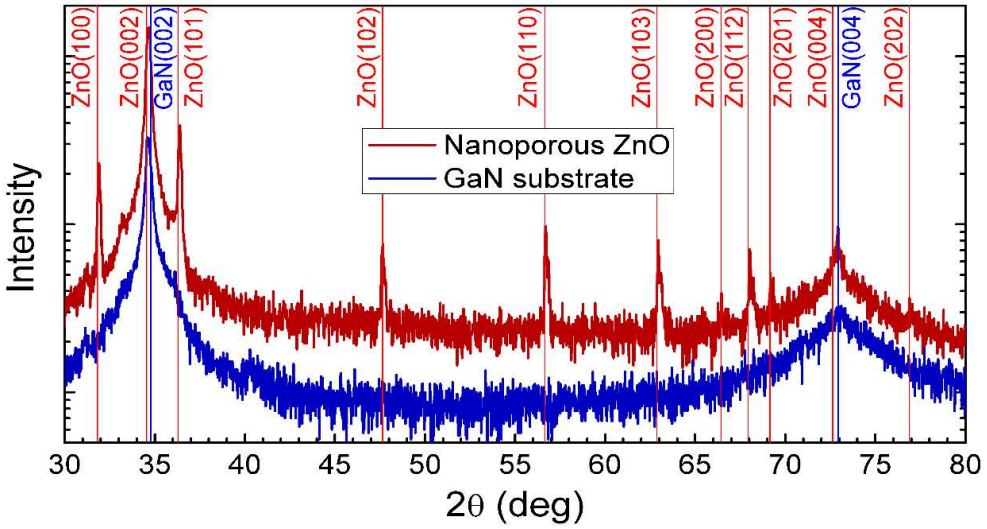

Figure 2.11: XRD of the nanoporous ZnO "nanopopcorn." Multiple crystal orientations are visible, with the strong (002) direction of the ZnO matching the GaN substrate orientation. The data are offset.

Additionally, XRD and TEM measurements determine whether the nanopopcorn nanostructure of ZnO was crystalline. Figure 2.11 shows the 2θ XRD scans of the ZnO nanopopcorn, showing that indeed the ZnO nanopopcorn is crystalline, but the nanostructure has multiple growth directions, and is not grown preferentially from the *c*-axis GaN substrate. The XRD peaks were determined using the Joint Committee on Powder Diffraction Standards

(JCPDS) numbers for ZnO and GaN are 36-1451 and 02-1078, respectively. Figure 2.12 shows TEM micrographs of the nanopopcorn, indicating that neighboring grains of ZnO nanopopcorn are not always oriented in the same (or not even a related) growth direction.

Further discussion of the nanopopcorn ZnO, comparing it to the vapor-solid grown nanowires and hydrothermally grown nanowires (discussed in section 2.2), is reserved for Chapter 6 of this document.

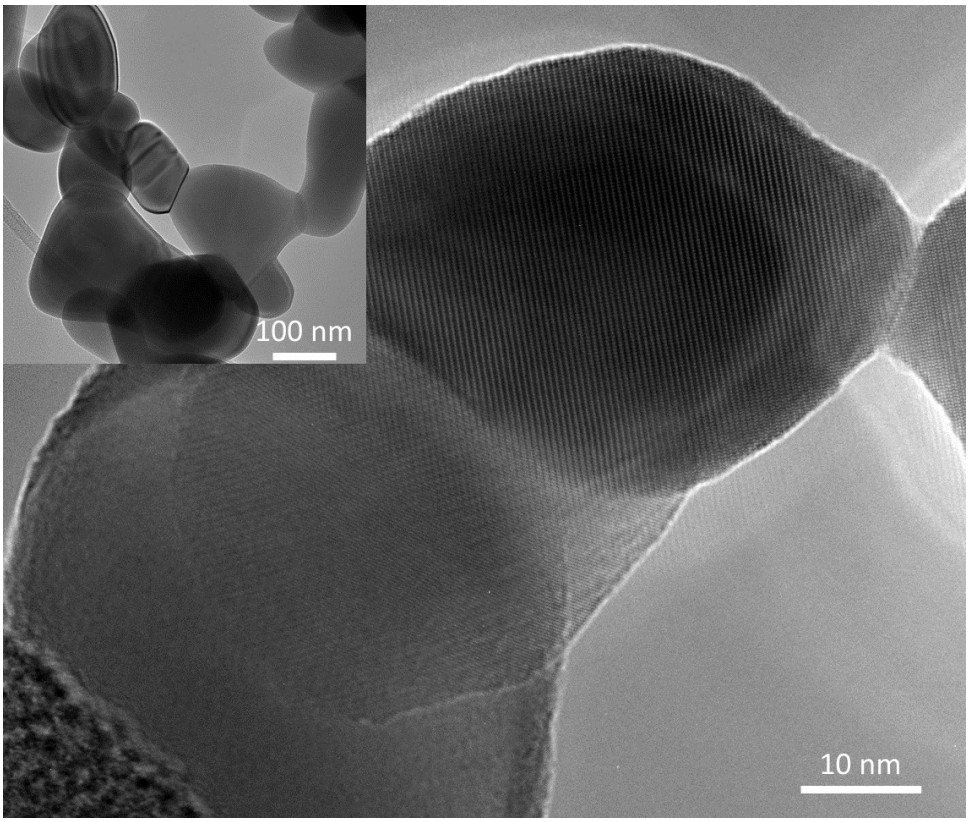

Figure 2.12: High-resolution transmission electron micrograph (HR-TEM) of three nanopopcorn grains (with inset of a zoomed out region showing many crystalline nanopopcorn grains). In the HR-TEM, lattice fringes are visible in the middle grain, and have the same orientation as the grain starting on the right of the image. However, the third grain, on the bottom left, does not show any lattice fringes, meaning the third grain is not oriented along the same axis as the other two.

2.2 Hydrothermal ZnO Nanowires

This section describes the low-temperature hydrothermal growth protocols for the ZnO nanowires discussed in Chapter 6 and Chapter 7.[21,38] The work in Chapter 6 is has not been published. The vertically oriented nanowires do not require any gold catalysts/seeding, but do require an epitaxial *c*-axis substrate to promote the proper orientation of growth.[64]

2.2.1 Vertically-Oriented Nanowires

Our collaborators, Professors Yichun Liu and Haiyang Xu, at Northeast Normal University in Changchun, Jilin Provence, China, developed the low-temperature hydrothermal method we use for growing vertically oriented ZnO nanowires. They have been publishing work using ZnO nanowires grown with this method for the past 7 years.[21,62,64,88] During the East Asia and Pacific Summer Institute Fellowship, these nanowire growth techniques were learned and a study was done of ZnO exciton and metal-nanoparticle plasmon coupling.

The hydrothermal method starts with a *c*-axis oriented substrate, chosen because it requires no ZnO or Au seeding to promote vertically oriented ZnO nanowires. The substrate is a 5 cm wafer of 1 μm thick *c*-axis p-GaN on *c*-sapphire, cleaved into approximately 4x6 mm rectangles. The substrates are mounted on a set of two polytetrafluoroethylene (PTFE) substrate holders. The holders can hold more than five substrates each, so over ten samples can be made at the same time under identical conditions. The holders are lowered into two identical PTFE-coated stainless steel reaction chambers. An equimolar solution of 20 mM zinc acetate dehydrate (ZA) and hexamethylene tetramine (HMT) is prepared by dissolving the ZA and HMT powders in deionized water using a magnetic spinner at room temperature. The 70 mL of

solution is divided between the two reaction chambers, and the two chambers are placed in an oven at 95 °C for 2.5 hours. After growth, the samples are rinsed with DI water and then annealed in air at 105 °C for 15 min to remove the residual organics and surface contaminations. The resulting nanowires grow preferentially in the *c*-axis orientation from the *c*-axis substrate.

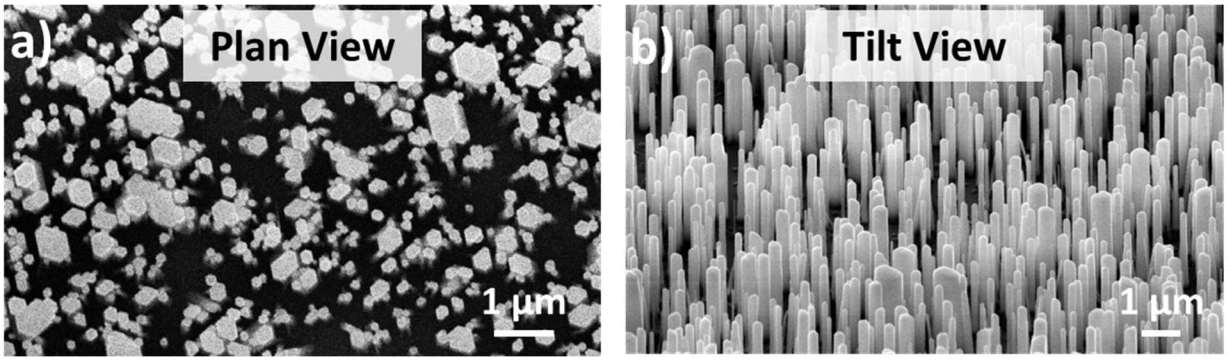

Figure 2.13: Typical SEM images of the carpet ZnO nanowire arrays in a) plan view and b) tilt view.

To verify the morphology of the nanostructures that had grown on the substrates, each sample was viewed by scanning electron microscopy (SEM, Hitachi, S-4200, Raith eLine, Zeiss Merlin with Gemini II column). Images were taken in both the plan view and 45˚ tilt configurations on multiple locations of a sample to gauge the uniformity of the growth. Samples from the same growth had identical nanowires, with the hexagonal cross section and vertical orientation of the typical carpet nanowires seen in Figure 2.13.

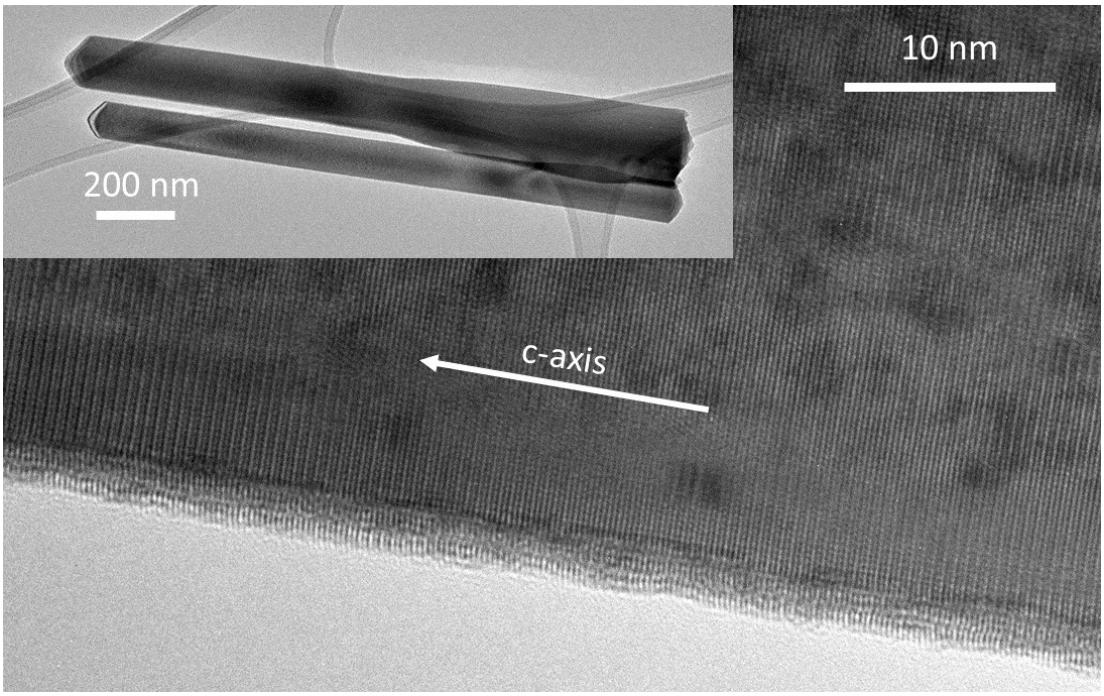

Figure 2.14: TEM (inset) and HR-TEM of hydrothermally grown ZnO nanowries, showing the *c*-axis growth direction along the long-axis of the nanowires.

The nanowire crystal orientation of the samples was confirmed with XRD and TEM. The TEM micrographs in Figure 2.14 show the *c*-axis growth direction is along the long axis of the hydrothermally grown nanowires, the same as in the vapor-solid nanowires. Figure 2.15 shows a typical XRD scan of the carpet nanowires, where the *c*-axis orientation (along the [002] and [004] direction) is clearly visible, and epitaxial with the p-GaN beneath. The JCPDS numbers for assigning the ZnO, GaN, and Al_2O_3 crystal orientations were 36-1451, 02-1078, and 46-1212, respectively.

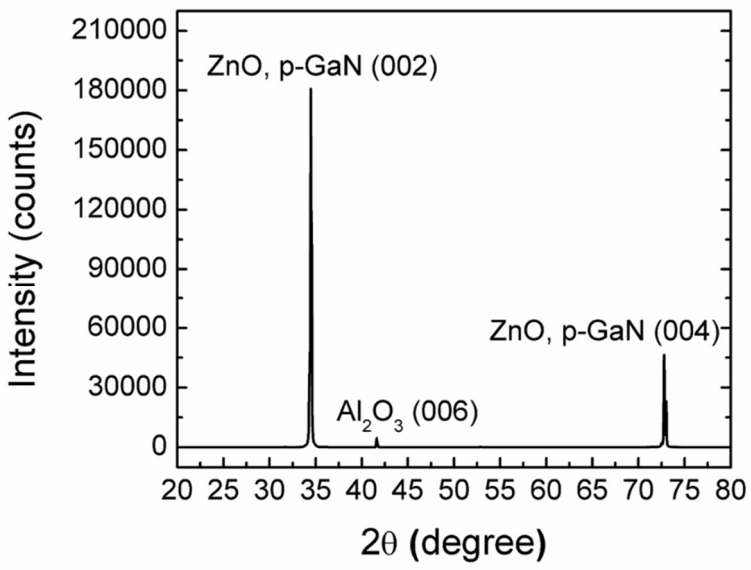

Figure 2.15: Typical XRD 2 theta scan of the vertically oriented carpet ZnO nanowires.

2.2.2 Dependence on Substrate

After returning from Northeast Normal University, the hydrothermal growth method was recreated at Fisk University in Nashville. The same hydrothermal solution and growth conditions were used, however, the substrate was varied to determine if something already in the lab could be used, as the p-GaN substrates had previously been purchased and provided by Northeast Normal University.

It was not possible to produce the hydrothermally grown, vertically-oriented nanowires except on the Mg-doped p-GaN substrates that Northeast Normal University provided. Figure 2.16 shows three different substrates that were tested in the hydrothermal method, that of an electron beam deposited ZnO seed layer, a fused silica substrate, and the *c*-axis GaN substrates (used for the nanopopcorn growth method). The only substrate that we expected vertically oriented ZnO nanowires to grow from the *c*-axis GaN substrate, as the ZnO should grow

epitaxially in the *c*-axis orientation on such a substrate. While the substrate did promote vertical orientation to the ZnO growth, it did not form nanowires, instead forming large platelets of ZnO, Figure 2.16.c, sparsely distributed on the sample. It is not surprising that the GaN and p-GaN substrates did not preferentially grow the same ZnO structures. Low temperature electron beam irradiation or rapid thermal annealing is required to activate the Mg acceptors in the p-type GaN,[16,89,90] with these annealing processes changing the surface chemistry of the p-GaN from that of GaN.[91] Changes in surface chemistry lead to variation in the interfacial thermodynamics, leading to differences in the morphology of the grown structures.[92] While the intrinsic GaN substrate did not grow nanowires, both of the other two substrates did. The nanowires that grew on the ZnO seed layer were thinner, less dense, and more uniform than the nanowires that grew on the fused silica substrate, Figure 2.16.a-b. For all substrate types, multiple samples were grown at a time. Each substrate consistently grew the same ZnO nanostructures.

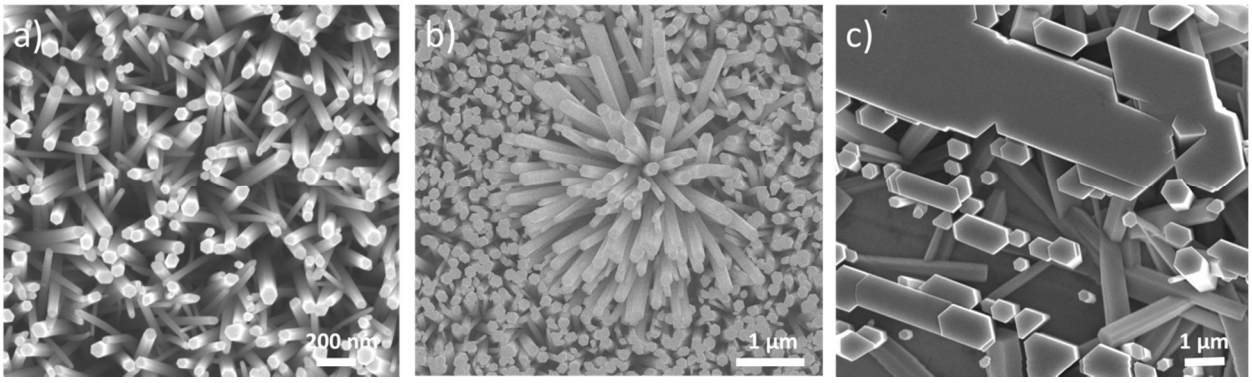

Figure 2.16: SEMs of hydrothermally grown nanostructures, using a substrate other than the p-GaN provided by Northeast Normal University. a) ZnO seed layer: thin, randomly oriented nanowires. b) Fused silica: dense, randomly oriented nanowires. c) Purchased *c*-axis GaN: ZnO *c*-axis platelets with randomly oriented ZnO nanowires growing from their edges.

At present, the collaboration with Northeast Normal University allows us to access *c*-axis p-GaN substrates that promote the growth of vertically-oriented, "carpet" ZnO nanowires. The knowledge that not all *c*-axis oriented GaN substrate promote ZnO nanowire growth indicates that a study of the surface chemistry conditions on p-GaN versus GaN substrates would be beneficial to understanding the growth mechanisms of vertically oriented ZnO nanowires.

2.3 Conclusions

A variety of ZnO nanostructures can grow from the modified vapor-solid growth technique. Slight changes in deposition parameters lead to large changes in the ZnO growth morphology. This modified vapor-solid growth method is capable of growing highly crystalline, randomly-oriented ZnO nanowires when a ZnO seed layer is used as the substrate and the correct growth parameters are used. To improve the vapor-solid growth technique, a new study of the PL-yield of bare LOP and HOP nanowires should be conducted with the new mass flow controllers. Additionally, a glancing-angle electron-beam deposition technique allows for uniform coatings of both insulating films and metal nanoparticles on to the sides of the nanowires. During vapor-solid growth, if a *c*-axis GaN substrate is used (instead of a ZnO seed layer) the free-form ZnO nanopopcorn forms instead.

A hydrothermal growth method can be used to grow vertically oriented ZnO nanowires. The nanostructure is dependent upon the substrate, with the vertically oriented ZnO nanowires only growing from a *c*-axis oriented p-GaN substrate. If the surface chemistry is not ideal, the ZnO still grows vertically, but does not form nanowires, instead forming large platelets of ZnO. When a ZnO seed layer is used, the nanowires grow preferentially in the orientation of the seed

layer, which varies from grain to grain, producing thin, randomly-oriented crystalline nanowires. More than ten identical samples can be grown at a time using the hydrothermal method, making it an ideal technique for the complex photoluminescence studies requiring multiple samples.

2.4 Acknowledgements

There are multiple collaborators to acknowledge for work done in this methods chapter. First, I thank Prof. Daniel Mayo, my mentor in both the Haglund and the Mu labs, for teaching to grow vapor-sold ZnO nanowires and do glancing-angle electron beam depositions. Additionally, we installed the new mass flow controllers for the vapor-solid method, allowing for better control of the oxygen flow during depositions, and trained Andrew Cook on the growth of vapor-solid ZnO nanowires. I thank Andrew and Dan for both being a part of the ZnO growth for the parameter sweep experiments. For growth of the vertically oriented ZnO nanowires, I first thank Prof. Yichun Liu and Prof. Haiyang Xu for accepting and mentoring me as a student in their lab for the summer of 2014. Second, I thank Dr. Weizhen Liu for training me throughout my time at Northeast Normal University, making sure I was connected with the correct students for learning each technique I needed for growing and analyzing the vertical nanowires. Finally, I thank Prof. Richard Mu and Prof. Richard Haglund for their encouragement to seek out methods of growing vertically oriented nanowires, as "carpet" nanowire systems have always been an aim of our research. Additionally, for the TEM images of all ZnO nanostructures grown, I thank Dr. James McBride. He has always been willing to work with me, from sample preparation to imaging, to get the best micrographs and EDS spectra of the ZnO samples.

CHAPTER 3

PLASMON COUPLED CORE-SHELL NANOWIRES

In this chapter, the enhanced UV photoluminescence of randomly oriented ZnO/MgO core-shell nanowires coated with Ag nanoparticles is discussed. The results of photoluminescence (PL), optical mode calculations, simulations based on finite element analysis (FEA), and numerical fitting and analysis show the coupling of the ZnO near-band-edge exciton emission to Ag localized surface plasmons and additional optical cavity effects due to ZnO/MgO core-shell nanowires. This work has been published in Mayo *et al* (minus the FEA),[31] however, the FEA is included in the Marvinney *et al* publication on ZnO/MgO core-shell nanowires in Chapter 5.[32]

- D.C. Mayo, **C.E. Marvinney**, E.S. Bililign, J.R. McBride, R.R. Mu, R.F. Haglund, *Surface plasmon mediated photoluminescence from Ag-coated ZnO/MgO core-shell nanowires*. Thin Solid Films, 2014. **553**: p. 132-137.

3.1 Background

By carefully tuning the emission of ZnO nanowires, a wide variety of high-efficiency devices have been fabricated in recent years, including LEDs,[93-95] lasers,[96,97] and sensors.[98,99] Although different growth, annealing, and doping conditions have all been employed to control the ZnO emission,[100,101] one of the most effective methods for emission enhancement is through coupling to plasmons. Surface plasmons in metallic nanostructures play important roles in many

modern nanotechnologies.[102-105] A strong, localized electric-field enhancement is generated in the neighborhood of the metal nanoparticle, which is highly sensitive to both the geometry of the nanostructure and the surrounding dielectric environment.[106-111] As a result, surface plasmons are broadly tunable and can be used to manipulate light at the nanometer scale in waveguides, absorbers, emitters, and field enhancers.[31,111-115] When metal films or nanoparticles are in proximity to a semiconductor, surface plasmon polaritons or localized surface plasmons can be created that have the potential to drastically enhance or quench emission through coupling of the surface plasmons to the semiconductor luminescent centers.

The enhancement of ZnO emission due to the presence of metal nanoparticles can result from a combination of charge transfer and local field effects, which sometimes makes it difficult to resolve the specific mechanisms responsible.[116,117] Previous research in ZnO thin films separated Ag or Au plasmonic structures from the ZnO using an insulating layer of MgO in varying thicknesses.[28] In this architecture involving spacer layers of increasing thickness, it was possible to study the effects of near-field plasmon-exciton coupling on the enhancement and quenching of the emission bands and isolate the effects of hot-electron transfer.

Here, plasmon-exciton coupling mechanisms were studied in ZnO/MgO core-shell nanowires by comparing nanowires with and without a silver-nanoparticle coating. By varying the thickness of the MgO layer, it was possible to examine the distance-dependent plasmonic effects and elucidate the mechanisms responsible for enhancing the ZnO band-edge photoluminescence (PL). The core-shell nanowires exhibited optical cavity effects as a function of MgO thickness that dramatically enhanced the band-edge PL yields in the ultraviolet. Finite-element simulations determine that both Fabry-Perot and whispering gallery modes can propagate in the nanowires. Decorating the core-shell nanowires with Ag nanoparticles resulted

in a further two-fold and three-fold plasmonic enhancement of the two identified optical cavity modes. The dramatic PL enhancement appears to be due to combined resonant-cavity and plasmonic effects and establishes the plasmonic core-shell nanowire structure as a useful architecture for optoelectronic devices.

3.2 Bare ZnO Nanowires

Under room temperature and atmospheric pressure conditions, ZnO crystallizes in a hexagonal wurtzite structure. The ZnO nanowires were grown using the low-oxygen pressure (LOP) modified vapor-solid method described in Section 2.1.1. They are uniform in thickness, randomly oriented, and have hexagonal facets at the ends, as evidenced by SEM imaging of the nanowires seen in Figure 3.1.a, indicative of high quality, single-crystal nanowires.

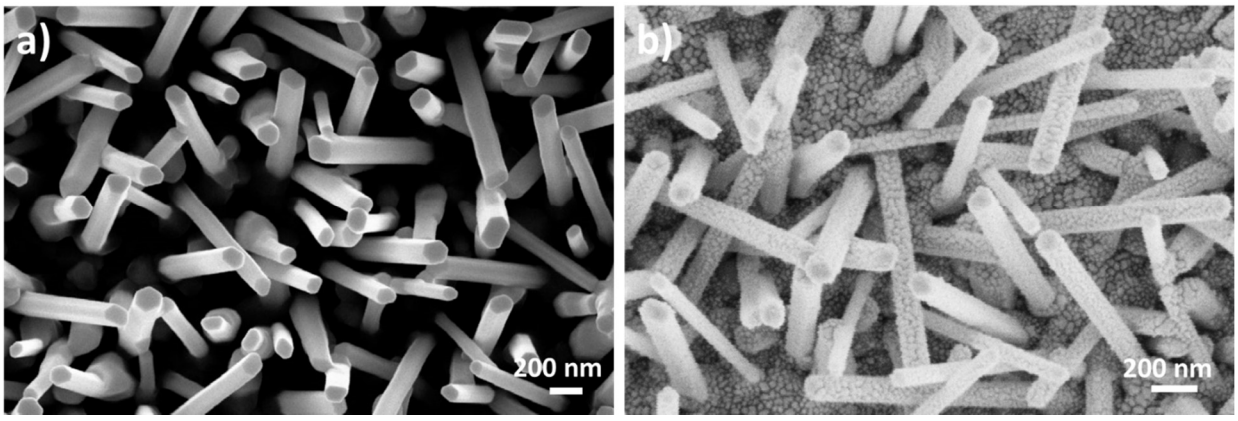

Figure 3.1: Scanning electron micrographs of a) bare LOP ZnO nanowires and b) Ag nanoparticle coated ZnO/MgO core-shell LOP nanowires.

The PL spectra of the ZnO nanowires is shown in Figure 3.2.a. For the bare ZnO nanowires, the band-edge to visible emission is greater than unity, which indicates high crystallinity of the ZnO nanowires.[1] The PL spectra were additionally measured at each MgO thickness. The spectra were measured with a thermoelectrically cooled (-40 °C) CCD camera in a spectroscopy set-up (HORIBA Jobin Yvon LabRAM 800HR) in the range of 1.86 eV – 3.76 eV, encompassing both the band-edge and defect emissions of the ZnO nanowires. The ZnO nanowire photoluminescence was excited by a 325 He-Cd laser (Kimmon, 1K series, 6 mW at the sample), detected in line with the laser normal to the surface. The PL spectrum of each MgO region were obtained as follows: ten PL spectra were acquired with an integration time of 0.2 s, accumulated, and averaged.

3.3 ZnO/MgO Core-Shell Nanowires

3.3.1 Photoluminescence

In order to study plasmon-exciton coupling, before any Ag nanoparticles could be deposited a spacer layer of MgO was deposited using glancing angle electron beam, as discussed in Section 2.1.2. The MgO coating not only provides an insulating layer between the ZnO nanowire and the Ag nanoparticles, but passivates the hot electrons and surface defects of the nanowires,[118-120] and has the potential to produce waveguiding.[21,22] The surface passivation is verified through the quenching of the visible emission in the PL measurements, as seen in Figure 3.2. The MgO was deposited in eight different thicknesses, from 0 nm - 70 nm in 10 nm increments, as described in Chapter 2, Section 2.1.

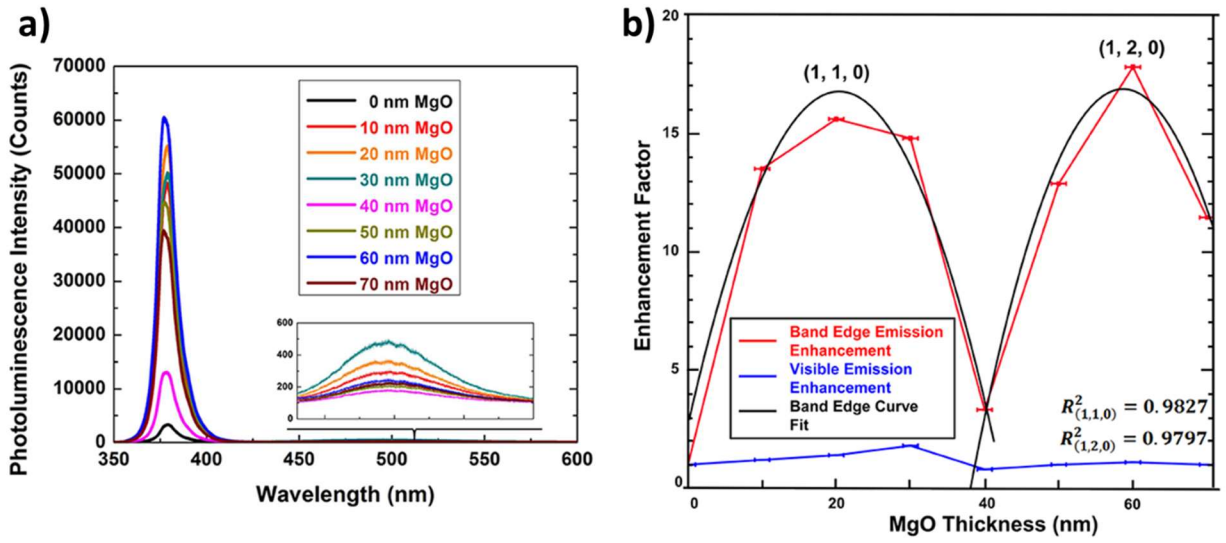

Figure 3.2: a) Photoluminescence measurements as a function of MgO coating thickness. b) The enhancement factor, which is the computed ratio of integrated photoluminescence, normalized vs the bare ZnO nanowires. At 20 nm and 60 nm MgO thickness, there is approximately a 15-fold enhancement of the photoluminescence compared to that of the bare ZnO nanowires.

Figures 3.2.a show the room-temperature PL spectra of the ZnO nanowires with MgO coatings of varying thicknesses. The inset for Figure 3.2.a display an expanded view of the visible emission spectra. The band-edge and visible emission peaks are located at 379 nm and 497 nm, respectively. The photoluminescence enhancement factors in Figures 3.2.b were calculated from the integrated areas under the emission bands in the PL spectra using a linear baseline and were normalized against the PL spectra from bare ZnO NWs. The ZnO/MgO core-shell nanowire PL spectra show a bimodal variation in the band-edge enhancement with increasing MgO thickness. Maximum enhancement is seen at MgO thicknesses of 20 nm and 60 nm, with a minimum at 40 nm. Contrariwise, the visible emission remains relatively constant independent of the MgO thickness.

3.3.2 Optical Cavity Mode Photoluminescence Enhancement

We propose that the dramatic enhancement of the band-edge emission seen in the ZnO/MgO nanowires is primarily due to resonant optical cavity modes within the coated nanowires. The Fabry-Perot optical cavity forms inside a two-dimensional cross section defined by the MgO/ZnO core-shell nanowire and bounded by air as seen in Figure 3.3.a. At the band-edge emission wavelength of approximately 380 nm, the refractive index of ZnO is approximately 2.45 while that of MgO is approximately 1.77. The reflection at the interface between the oxides due to the difference in refractive indices can be modified by the tendency of Mg^{2+} to diffuse into Zn^{2+} sites to form $Zn_{1-x}Mg_xO$.[121,122] In Chapter 5, transmission electron micrographs show the interface region between the MgO and ZnO, which show only a small superlattice region between the two layers. The effective index of the core-shell nanowire structure can be simply calculated as a weighted average. Due to the single-crystal nature of the ZnO nanowires, the faceted surfaces form three degenerate Fabry-Perot cavity modes.

The thickness of the MgO coating, t_{MgO}, that results in a resonant condition can be calculated using straightforward, standing-wave analysis with a slightly modified version of an equation[123] for a square resonant cavity that properly accounts for the hexagonal shape of the ZnO nanowires:

$$m = \frac{\lambda\sqrt{j^2 + k^2 + l^2} - 2(z \times n_z)}{4n_m} \qquad (3.1)$$

Here, z and n_z, and m and n_m, are the thicknesses and refractive indices of the ZnO nanowire and the MgO coatings, respectively. The resonant modes are specified by integers j, k, and l, with the band-edge emission wavelength λ. For ZnO nanowires, approximately 80 - 90 nm in diameter, Figure 3.3.b shows the calculated MgO thicknesses for the lower-order (1,1,0) and the higher-

order (1,2,0) Fabry-Perot modes. The calculations show resonant conditions occurring at thickness values of approximately 20 nm and 60 nm. This agrees well with the measured band-edge emission maxima. Additionally, the visible emission does not show any enhancement over the range of MgO thicknesses. This is also in agreement with the optical cavity explanation since no resonant modes at the ZnO visible emission wavelengths can be excited for these thicknesses of ZnO/MgO core-shell nanowires.

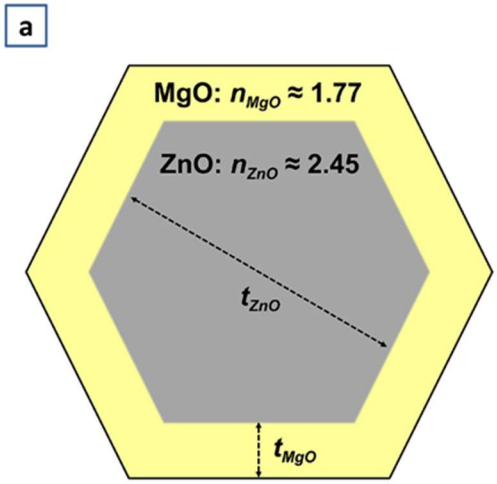

b

ZnO Nanowire Thickness (t_{ZnO}) (nm)	MgO Coating Thickness (t_{MgO}) for Resonance Mode (j,k,l) (nm)	
	(1,1,0) Mode	(1,2,0) Mode
87	21	65
88	20	64
89	20	64
90	19	63
91	18	62
92	18	62
93	17	61
94	16	61
95	16	60
96	15	59

Figure 3.3: a) Cavity diagram of hexagonal core-shell nanowires, and b) calculated MgO thicknesses corresponding to resonant Fabry-Perot cavity modes at specific ZnO core thicknesses for a wavelength of 380 nm.

3.3.3 Optical Cavity Simulations

To determine the mode shape and enhancement factor of the optical field intensity as function of MgO shell thickness, the optical cavity modes of the ZnO/MgO core-shell nanowires are studied further. The optical cavity modes are simulated in a hexagonal cross section of the

core-shell nanowire using finite-element analysis (FEA), as has been done on ZnO nanoneedles by Kirschbrown *et al*.[23] In Kirshbrown *et al*, the allowed optical cavity modes in the changing diameter ZnO exhibited both Fabry-Perot character, as in our calculations, but also whispering gallery modes.[24,124] Here, FEA is conducted on the ZnO/MgO core-shell nanowire to determine the mode-shape and enhancement factor of the optical field intensity as a function of MgO shell thickness using a hexagonal cross section of the core-shell nanowires. The experimentally measured PL enhancement in the core-shell nanowires stems from three interlinked effects of the optical cavity modes: exciton production from the 325 nm light, band-edge exciton emission of the 380 nm light, and size and shape of the core-shell nanowire. All three effects must be considered in order to understand the experimental photoluminescence enhancement.

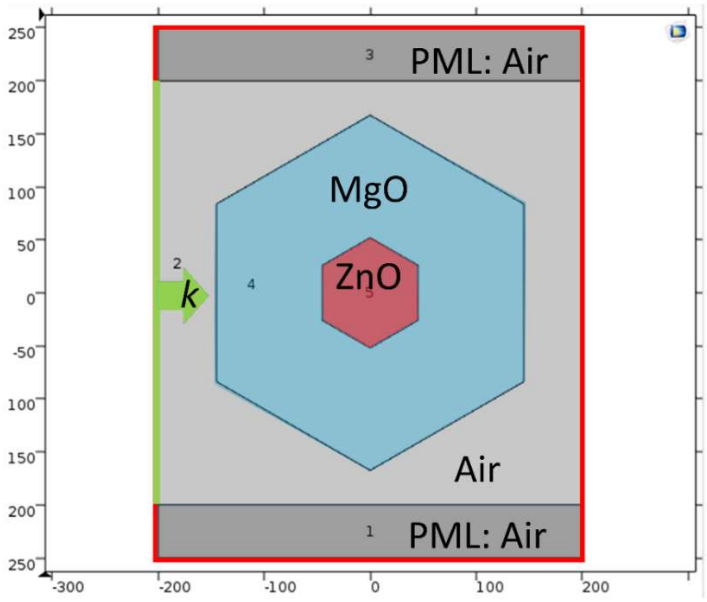

Figure 3.4: Geometry of finite-element simulation. Scale is in nanometers. The ZnO nanowire is 90 nm (red), here with a 100 nm MgO shell (blue), both materials defined by refractive indexes. The region around the nanowire cross section had a refractive index of 1 for air (light and dark grey). The plane wave entered through the green side-wall scattering boundary condition, with wavevector *k* indicated. The red side walls are a second scattering boundary condition to prevent reflections, and the perfectly matched layers (PML)(dark grey regions) further prevent reflections. Finite-elements method was used to solve Maxwell's equations for all regions inside the scattering boundary conditions.

The cavity-mode characterizations of the ZnO/MgO nanowire is computed by FEA using the wave optics module of COMSOL Multiphysics. A two-dimensional cross-section of a ZnO/MgO core-shell nanowire is used to model the cavity, Figure 3.4, and a plane wave is introduced to the system to study the electric field confinement. Two wavelengths are simulated, the λ = 325 nm PL excitation source and the λ = 380 nm ZnO peak UV emission. For simulations of both wavelengths, the ZnO nanowire diameter is held constant while the MgO thickness was varied. The complex refractive indexes for ZnO, MgO, and air are entered using references [125-127].

First, the cavity efficiency of the 325 nm pump wavelength is simulated, as it controls the rate of exciton production in the ZnO nanowires. The intensity is integrated and normalized as in equation 3.2:

$$Normalized\ Intensity\ (t_M, \lambda) = \frac{\iint_0^{A_{ZM}(x,y)} E(x,y)^2 dxdy \ / \ A_{ZM}}{\iint_0^{A_Z(x,y)} E(x,y)^2 dxdy \ / \ A_Z} \qquad (3.2),$$

where $E(x,y)^2$ is proportional to the intensity of the electric field at position (x,y) in the simulation, A_{ZM} is the hexagonal cross-sectional area of the ZnO/MgO core-shell nanowire for a given MgO thickness t_M, A_Z is the hexagonal area of the bare ZnO nanowire cross section, and λ is the wavelength of the simulation. Figure 3.5.a shows the normalized intensity of the simulated 325 nm pump as a function of MgO thickness for a ZnO nanowire core of 90 nm, approximating the average LOP nanowire diameter of 93 nm, Table 2.3. The core-shell nanowire exhibits maximal normalized intensities for the 325 nm pump light at 16 nm and 52 nm of MgO thickness, with the insets showing the mode shapes at the maxima. The lower order mode sets

up a Fabry-perot mode, reflected between the facets of the nanowire,[23,24] while the higher order mode sets up a whispering gallery mode.[23,24]

Second, the normalized intensity of the 380 nm exciton emission is simulated for a 90 nm ZnO core for varying MgO thicknesses (Figure 3.5.b), as an increased intensity of 380 nm emission inside the core-shell nanowire should lead to enhanced PL of the UV near-band-edge emission, due, for example, to the emptying of trap states just below the conduction-band edge. Two maxima of the normalized intensity occur, at 16 nm and 68 nm of MgO thickness. The Figure 3.5.b insets show, again, that the lower order mode shape is Fabry-Perot type, while the higher order mode is whispering gallery type.

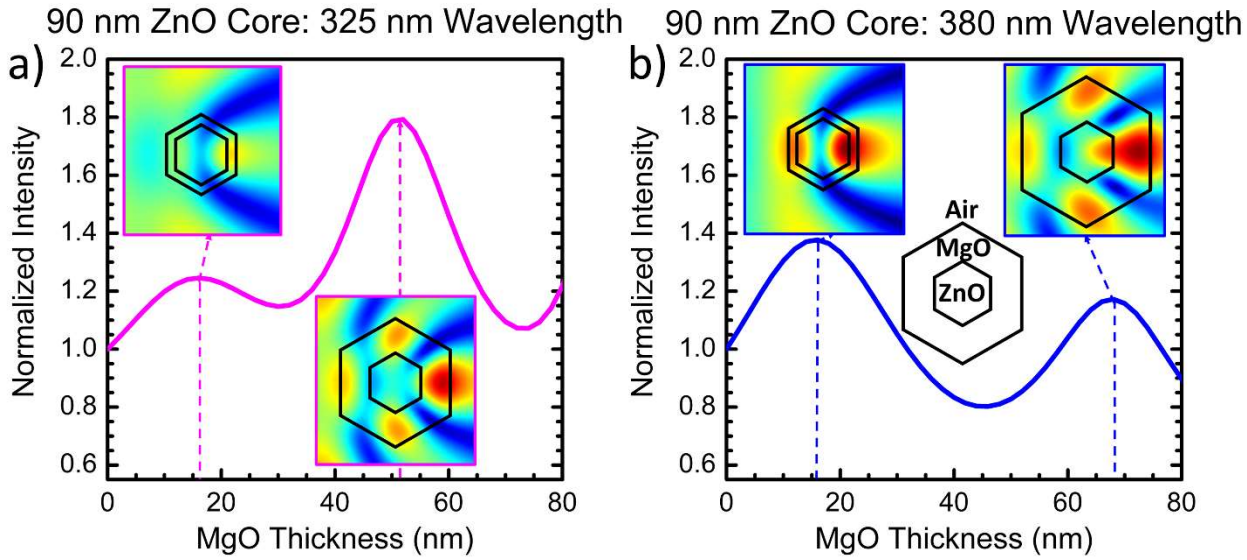

Figure 3.5: Finite-element simulation results of a ZnO/MgO core-shell nanowire cross section. The normalized intensity (equation 3.2), plotted versus MgO thickness for a) the 325 nm ZnO excitation source and b) the 380 nm band-edge emission. Insets in a-b) depict the electric field maps in the ZnO/MgO cross sections at the indicated MgO thicknesses. The black and white schematic in b) indicates the materials assigned to each region in the simulation.

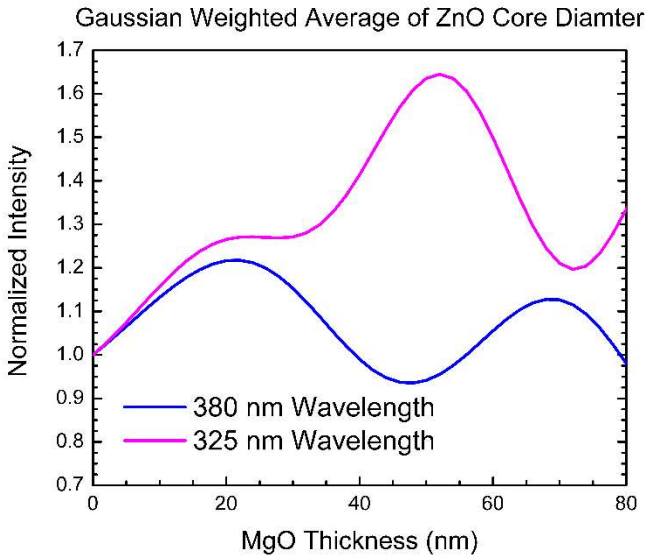

Figure 3.6: The Gaussian weighted averages of the normalized intensities from the varying ZnO core diameter finite-element simulations of the ZnO/MgO core-shell nanowires.

Additional simulations with varying ZnO diameters, from 70 – 110 nm in 5 nm increments, were used to account for the 19 nm standard deviation in the LOP ZnO nanowire size (as calculated in section 2.1.2, Table 2.3). As each experimental PL measurement encompasses a 10 μm diameter spot of nanowires, the resulting PL enhancement at each MgO thicknesses comes from an averaging of the enhancement that occurs from the normalized intensity associated with each ZnO core diameter. This average of the normalized intensity is computed as a Gaussian weighted average, with the 90 nm ZnO core representing the average diameter for the Gaussian, and the 70 nm and 110 nm ZnO core diameters representing one standard deviation away from the average. Figure 3.6 shows the Gaussian weighted averages of the 325 nm and 380 nm wavelengths. For the 325 nm wavelength, the Gaussian weighted average has a much stronger second-order cavity mode than first-order cavity mode and the minimum near 30 nm MgO thickness all but disappears. For the 380 nm wavelength, the two

optical cavity modes that appear are close to the same intensity, however, the higher order mode is at a larger MgO thickness than found in experiment.

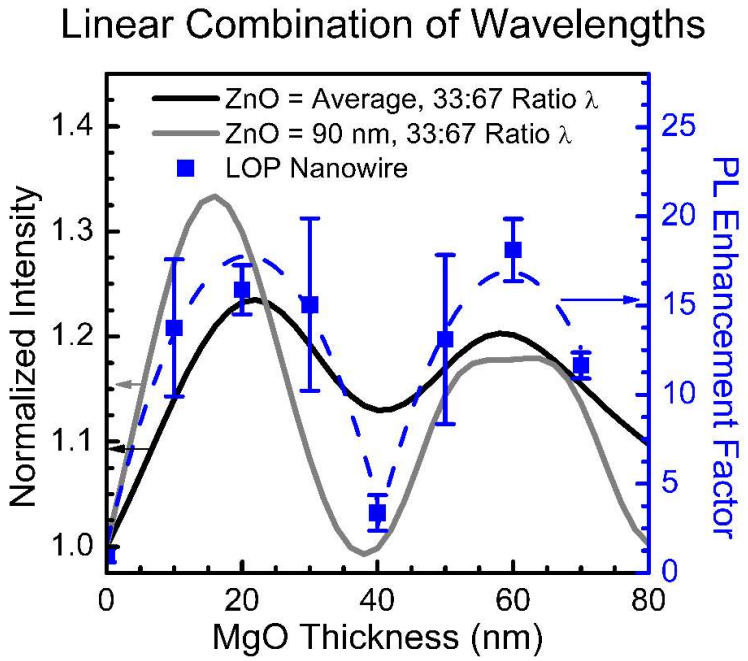

Figure 3.7: Finite-element simulation results of a ZnO/MgO core-shell nanowire cross section. The normalized intensity (Equation 3.2), plotted versus MgO thickness for a linear combination of the 325 nm ZnO band-edge emission and the 380 nm excitation source. An internal quantum efficiency of 50% is used, giving a ratio of 33% to 67 % the 325 nm light to the 380 nm light. The gray line depicts the data for only the 90 nm ZnO core simulation, while the black line depicts the data for the Gaussian weighted average over all the ZnO core diameters. The blue data and right axis of the graph depicts the LOP nanowire 380 nm band-edge photoluminescence enhancement, in order to visually compare the simulation and experimental results.

While simulations of each wavelength individually allow the determination of the optical cavity mode shapes at each PL maximum, neither wavelength alone predicts the MgO thicknesses where the maxima occur experimentally. Thus, the internal quantum efficiency (IQE) of the ZnO nanowires needs to be taken into account by using a linear combination of the 325 nm and the 380 nm simulated normalized intensities. The IQE of the ZnO nanowire

determines the amount of 325 nm light that converts to 380 nm light, with ZnO nanowires having a high IQE, typically between 30 %[128] and 60 %.[129] The gray curve in Figure 3.7 shows the linear combination of the normalized intensities for the 90 nm ZnO nanowire simulations, weighting the 325 nm normalized intensity at 33 % and the 380 nm normalized intensity at 67 %, assuming an IQE of 50 %. A sharp lower-order maximum is at 16 nm MgO thickness and a flat higher-order maximum is at 62 nm MgO thickness. The black curve in Figure 3.7 takes this a step further, taking the same 33:67 ratio of the 325 nm:380 nm wavelengths, however using the Gaussian weighted averages of all the ZnO nanowire diameters simulated for both the 325 nm and 380 nm wavelengths. Two maxima occur in this case at 22 nm and 58 nm MgO thickness.

As is observed in Figure 3.7, the MgO thicknesses of the maxima in the linear combinations of the simulated normalized intensity approximate the MgO thicknesses of the experimental PL enhancement maxima much more closely than the simulations for individual wavelengths. In fact, the simulated curve that most closely matches the shape and MgO thickness of the core-shell nanowire experimental data is the one that takes into account not only the two wavelengths required for the experiment, but also the standard deviation in the ZnO core diameter. However, the simulated peak enhancement for the weighted average of normalized intensity (black line), about 1.25 for 20 nm and 60 nm of MgO thickness, does not match the peak normalized PL intensity, which is about 15 for 20 nm and 60 nm MgO thickness. The order of magnitude difference between simulation and experiment arises because the simulation is only for a single two-dimensional (2D) cross section of the hexagonal core-shell nanowire, while the experiment is for a three-dimensional (3D) nanowire. In a 3D simulation, the intensity in the 2D cross section could be integrated along the length of the nanowire, substantially increasing the calculated peak enhancement for the two optical cavity modes. Additionally, a 3D simulation

would account for the ability of the UV luminescence to propagate along the length of the ZnO nanowire waveguide,[21,22,130-133] allowing for a complete calculation of the experimental enhancement.

Finally, in the simulations in Figure 3.7, the maxima of the higher order whispering gallery mode still has a lower normalized intensity than the lower order Fabry-Perot mode. Differences in the shape of the hexagonal ZnO core nanowire cross section may account for this, as in Dong, *et al*.[24] An elongated hexagonal ZnO core, as seen in some nanowires in Figure 3.1.a, would support a larger number of optical cavity mode shapes, especially whispering gallery modes. Thus, including some fraction of elongated hexagonal cavities in our simulations could increase the peak intensity of the second order cavity mode even further, accounting for the final difference in the two peaks.

Overall, when the optical cavity mode simulations take into account excitation wavelength, emission wavelength, size and shape of the ZnO nanowire, they closely approximate the observed PL enhancement. These 2D simulations give a satisfactory description for the two spatially distinct modes that are associated with enhanced PL at different MgO thicknesses and provide a rough prediction method for the MgO-thickness-dependent PL enhancement. When combined with a waveguiding effect of the UV emission along the length of the nanowires, these optical cavity modes are the most likely mechanism for the bimodal PL enhancement of the ZnO/MgO core-shell nanowires.

3.4 Ag Coated ZnO/MgO Nanowires

3.4.1 Photoluminescence

The ZnO/MgO core-shell nanowires were overcoated with an Ag film, forming 7 nm diameter nanoparticles on the sides of the nanowires, as described in Section 2.1.2, Table 2.4. Figures 3.2.b shows the Ag coated nanowires, displaying the uniform coating across the sample. This nanoparticle film is further characterized in Section 2.1.2.

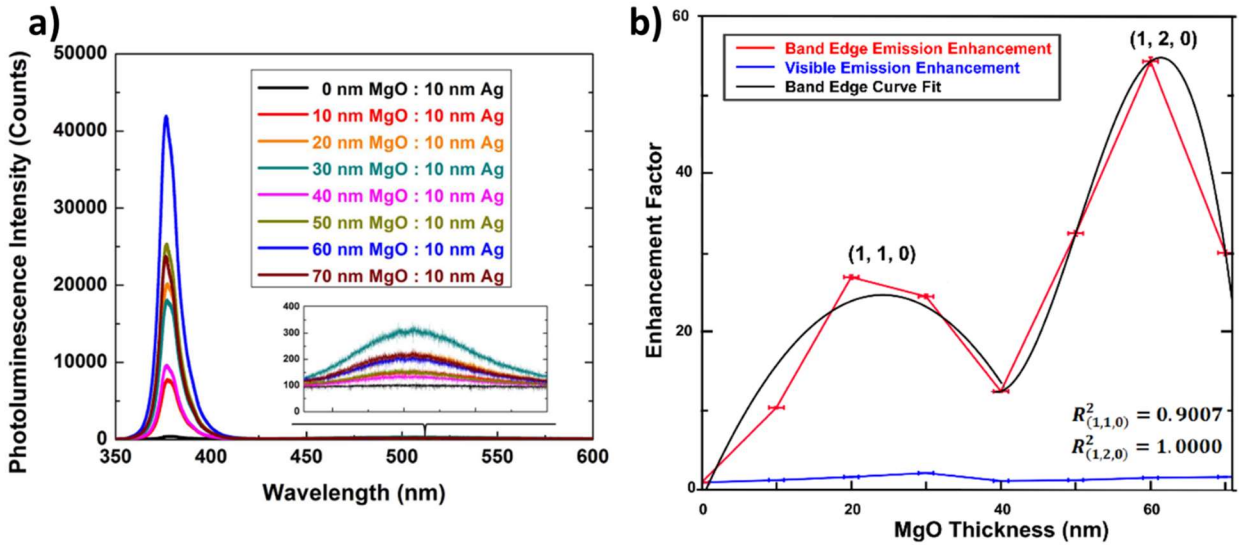

Figure 3.8: a) Photoluminescence spectra of Ag-decorated core-shell nanowires. b) Emission enhancement normalized against the Ag coated ZnO nanowire with 0 nm of MgO spacer. At 20 nm MgO thickness, the band-edge luminescence is enhanced approximately 25 fold while at 60 nm of MgO thickness, the emission is enhanced 55 fold.

Again, the photoluminescence spectra were acquired of the Ag coated sample in each MgO thickness region. Figure 3.8 shows the room-temperature PL spectra of the core-shell ZnO/MgO nanowires functionalized with Ag nanoparticles, with an inset displaying an expanded

view of the visible emission spectra. The band-edge and visible emission peaks are located at 377 nm and 511 nm. Extinction spectra taken of the sample, Figure 2.8, show the LSPs of the Ag nanoparticles on the LOP nanowires are centered at 475 nm. The PL enhancement factors in Figures 3.8.b were calculated from the integrated areas under the emission bands in the PL spectra using a linear baseline and were normalized against the PL spectra from bare ZnO nanowires. Again, there is a bimodal enhancement of the band-edge emission that varies with the thickness of the MgO coating, with maxima at 20 nm and 60 nm MO thickness. However, the enhancement is not uniform across the two optical cavity modes. The lower-order Fabry-Perot mode sees an additional two-fold enhancement over the ZnO/MgO core-shell nanowires, while the higher-order whispering gallery mode sees an additional almost three-fold enhancement. The visible emission enhancement remains centered at unity.

3.4.2 Plasmon Enhancement Mechanisms

Based on the differing shapes and magnitudes of the resonant enhancement for the nanowire structures with and without Ag nanoparticles, we propose that two different mechanisms govern the enhancement at the lower-order optical cavity mode versus at the higher-order optical cavity mode. Both mechanisms stem from Purcell enhancement of the radiative transition rate, where the transition rate is described by Fermi's Golden Rule #2:

$$\Gamma_{p,0} = \frac{2\pi}{\hbar}\left|\langle f|\hat{H}_{int}|i\rangle\right|^2 \rho(\hbar\omega) \qquad (3.3)$$

where $\left|\langle f|\hat{H}_{int}|i\rangle\right|^2$ is the matrix element of the dipole transition from excited to ground state due to the purturbing electromagnetic field, and $\rho(\hbar\omega)$ is the joint density of states of the plasmons and excitons.[28,87]

For the lower-order mode, the additional factor two enhancement seen at 20 nm of MgO thickness when Ag nanoparticles are added to the system is due to the large increase in the density of states from the presence of the LSPR in the Ag nanoparticles. The LSPR of the Ag nanoparticles overlaps with the band-edge emission of the ZnO, especially for the smaller nanoparticles present on the sides of the ZnO nanowires (Section 2.1.2), where the smaller, 7 nm nanoparticles have a blueshifted plasmon resonance from the larger, 23 nm nanoparticles on the tops of the nanowires. This overlap in the LSPR with the ZnO exciton emission results in a Purcell-enhanced radiative recombination rate of the ZnO exciton due to the plasmon-exciton interaction, as described by Equation 3.3, where the addition of the plasmon density of states into the system enhances the radiative emission rate of the ZnO excitons. The increased radiative emission rate of the ZnO nanowire excitons leads to the additional two-fold enhancement of the band-edge photoluminescence.

The additional factor of three enhancement for the ZnO/Mg/Ag nanowires at 60 nm MgO thickness, however, should not be from plasmon-exciton coupling, as the electric field of the LSPR from the Ag nanoparticles will be attenuated when it reaches the ZnO core.[28] Instead, an enhancement occurs due to the larger spatial extent of the whispering gallery modes compared to the Fabry-Perot modes, and the closer proximity of the whispering gallery modes to the surface of the MgO shell and thus the Ag nanoparticles. As light reflects from the exterior facets of the MgO, two scattering mechanism could potentially occur. First, light may be back-scattered by the plasmons into the hexagonal cavity and across the ZnO core, greatly enhancing the interaction cross section of light with the ZnO core. Second, light that has been potentially trapped in the MgO shell cavity may be scattered out of the hexagonal cavity by the plasmons, greatly enhancing the amount of light that can escape the system. These Ag nanoparticle

scattering effects lead to the additional three-fold enhancement observed at 60 nm MgO thickness.

3.4.3 Numerical Analysis

The photoluminescence emission enhancements for both the Ag coated and uncoated ZnO/MgO core-shell nanowires were analyzed numerically to provide additional insight to the MgO thickness dependence of the enhancement. Quadratic and cubic equations were fit to the enhancement curves for increasing MgO thickness. The first two quadratic fits are shown in 3.2.b, the first for for thicknesses $t_{MgO} \leq 40$ nm, and second for $t_{MgO} \geq 40$ nm. The root mean square (RMS) deviations for the ZnO/MgO fits were 1.7 for $t_{MgO} \leq 40$ nm and 1.5 for $t_{MgO} \geq 40$ nm, equations below:

$$p_1(m) = -.03x^2 + 1.4x + 2.7 \tag{3.4}$$

$$p_2(m) = -.03x^2 + 4.7x - 120.2 \tag{3.5}$$

For the enhancement observed in the Ag nanoparticle coated ZnO/MgO core-shell nanowires, both quadratic and cubic terms were needed to fit the data, a quadratic fit for thicknesses $t_{MgO} \leq 40$ nm, and an overwhelmingly quadratic fit with cubic terms for $t_{MgO} \geq 40$ nm. The fitted equations are shown in Figure 3.8.b. The Ag coated ZnO/MgO nanowires had RMS values of 4.8 and 10.7 for the two enhancement regions, respectively, equations below:

$$p_1(m) = -.04x^2 + 2.1x - 1.2 \tag{3.6}$$

$$p_2(m) = -.01x^3 + 1.2x^2 - 58.6x + 903 \tag{3.7}$$

The RMS values for all four fits indicated that the equations were a good fit to the band-edge emission enhancement data.

A cubic fit was only required for the measurements the second-order optical cavity mode at 60 nm MgO thickness that included Ag nanoparticles. This is due to the drastically different enhancement mechanism of this mode when coupled to Ag plasmons. Instead of enhancing the ZnO emission through an enhanced radiative emission rate of the ZnO excitons, at this MgO thickness the plasmons scatter the light that is trapped in whispering gallery modes back into the ZnO core and also out of the nanowire. Thus, additional Fabry-Perot modes can be generated in the core and light that could never escape can emit from the nanowire. These in turn greatly enhance the ZnO band-edge photoluminescence.

3.5 Conclusions

The ZnO/MgO core-shell nanowire structure exhibits optical cavity effects that dramatically enhance the band-edge PL yields in the ultraviolet, while not enhancing visible luminescence due to quenching of surface defects. In addition, the plasmonic enhancement of the band-edge emission at least doubles the PL enhancement due to the resonant cavity effects alone. Moreover, the plasmonic enhancement is MgO thickness dependent, with the lower order Fabry-Perot mode enhanced through Purcell enhancement of the ZnO exciton radiative recombination rate,[28] and the higher-order whispering gallery mode is enhanced from the larger spatial extent of the mode in the MgO shell scattering from interactions with the Ag plasmons. These results establish the core-shell nanowire architecture as an attractive approach to enhance the UV band-edge emission of ZnO for optoelectronic applications.

3.6 Acknowledgements

I thank Prof. Daniel Mayo for writing many of the drafts of this chapter with me as we prepared for submission. I also thank Dan for all his collaborative experimental work on the core-shell nanowires, as these experiments were first conceived during his Master's Thesis work, and we brought them to fruition when I began work in the Haglund lab. I acknowledge the analytical work of our REU student, Ephraim Bililign, as he contributed the experimental enhancement factor fitting functions to this chapter. Thank you Ephraim. I thank Dr. James McBride for his TEM/STEM/EDS imaging and analysis of our samples, which was a needed contribution to respond to reviewers. These were the first of many samples that I brought to James. And I acknowledge the work Prof. Mu and Prof. Haglund put into mentoring, editing, and advising the work done in this chapter.

CHAPTER 4

PLASMON CHARACTERIZATION BY COMPLEMENTARY SPECTROSCOPIES

To examine the Purcell enhancement of the Ag coated ZnO/MgO core-shell nanowires further, a collaboration with Oak Ridge National Lab was formed to characterize the samples with scanning transmission electron microscopy (STEM) cathodoluminescence (CL) measurements and high-angle annular dark field (HAADF) imaging. Cathodoluminescence measurements confirm coupling exists between the Ag plasmons and the ZnO excitons. These Ag coated nanowire CL studies also led to the discovery of a new technique for characterizing nanoparticle plasmon modes. When cathodoluminescence and electron energy loss spectroscopy (EELS) are used together, their complementary nature enables the complete three-dimensional characterization of the plasmon modes of a random morphology nanoparticle, such as the large Ag nanoparticles observed on the low-oxygen pressure (LOP) nanowires. Finite-difference time-domain (FDTD) simulations confirm the experimental results represent an accurate picture of the possible plasmon modes. This work is published:[30]

- J.A. Hachtel, **C.E. Marvinney**, A. Mounti, D. Mayo, R. Mu, S.J. Pennycook, A.R. Lupini, M.F. Chisholm, R.F. Haglund, S.T. Pantelides, *Probing plasmons in three dimensions by combining complementary spectroscopies in a scanning transmission electron microscope.* Nanotechnology, 2016. **27**(15): p. 155202.

4.1 Background

The functionality of plasmonic devices relies heavily on the precise spatial distribution of the near-field enhancement and the spectral distribution of characteristic surface plasmon frequencies.[134-137] Techniques for analyzing and mapping surface plasmons with nanoscale precision are a growing area of nanotechnology research.[105,138-141] Electron-beam techniques, such as electron energy-loss spectroscopy (EELS) and cathodoluminescence (CL) in a scanning transmission electron microscope (STEM), can probe plasmons by inelastic scattering between the fast beam electrons and conduction-band electrons in a nanostructure with sub-nanometer resolution.[142-145] As a result STEM–EELS and –CL have recently been successfully used to map and analyze surface plasmon modes in metallic plasmonic nanostructures and highly doped semiconductors.[146-155] Additionally, EELS and CL have been used in tandem on individual nanoparticles to distinguish radiative from non-radiative plasmonic excitations.[156] In order to access the full, three-dimensional plasmonic response of nanostructures, many researchers have employed tilt series tomography to develop three-dimensional plasmonic maps of the spatial intensity distributions of individual plasmon modes[157-159] and to reconstruct the precise morphology of the structure and simulate its behavior.[160,161]

However, for complex geometries, where the two-dimensional projection of the tilted system is difficult to interpret directly, tomography and computerized reconstructions can be prohibitively difficult or time consuming. Thus, finding a way to use the standard STEM techniques to circumvent these limitations and developing a straightforward way to analyze surface plasmons in three-dimensions, are both desirable objectives.

4.2 Plasmon-Exciton Coupling

In Chapter 3, evidence of plasmon-exciton coupling in the Ag coated ZnO/MgO core-shell nanowires was presented and discussed. To examine the Purcell enhancement of the Ag coated ZnO/MgO core-shell nanowires further, the samples were characterized by STEM-CL measurements and high-angle annular dark field (HAADF) imaging.

4.2.1 Cathodoluminescence Methods

The STEM–CL measurements were taken in a VG-HB601 aberration-corrected STEM operated at 60 kV using a focused beam of above ZnO bandgap energy electrons which excited the plasmonic and luminescent centers within the sample. The CL experiment was operated with a voltage to increase beam-sample interaction and the CL signal-to-noise ratio. A high beam current, ~2 nA, was used in order to maximize signal intensity. The data were collected with a locally (Oak Ridge National Laboratory) built light-collection system, as depicted in Figure 4.1. It features an in-lens, piezo-positioned parabolic mirror subtending approximately a 2 str solid angle, a Hamamatsu R9110 Peltier cooled photomultiplier, and Princeton Instrument Acton 2500 spectrometer equipped with a PIXIS Excellon 100BR. For the CL–spectrum images (SI), the value of each pixel is defined as the integrated intensity across a spectral range of 50 nm. All CL–SI are acquired with 20 s integration time per spectrum. At these long acquisition times, beam damage becomes a significant concern, so pixel size is increased and sub-pixel scanning is applied to reduce the total dose at each point. Both HAADF images and CL measurements were taken together to provide complementary morphology and emission information.

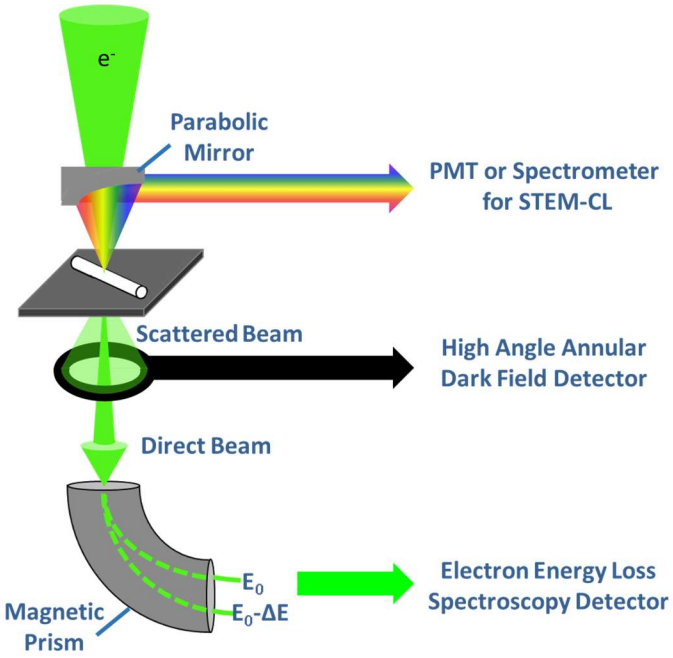

Figure 4.1: Schematic of the scanning transmission electron microscopy (STEM) imaging configuration for the high-angle annular dark field (HAADF), cathodoluminescence (CL), and additionally the electron energy loss spectroscopy (EELS) measurements of the Ag nanoparticles and Ag coated ZnO/MgO core-shell nanowires. *Image courtesy of Jordan Hachtel.*

4.2.2 Plasmon-Exciton Coupling

Individual ZnO/MgO core-shell nanowires, prepared by the contact transfer method (as discussed in Section 2.1.2), were imaged in HAADF mode and CL spectra were acquired. Nanowires with a non-uniform Ag-nanoparticle distribution are shown in Figure 4.2. In the HAADF image, it is clear that areas with high densities of Ag nanoparticles alternate with areas of low densities of Ag nanoparticles. In the corresponding CL-SI, strong intensity of the CL emission in the ZnO nanowire corresponds to the high-density Ag nanoparticle locations in the HAADF image. Conversely, the low density Ag-nanoparticle locations see the lowest intensity

CL emission from the ZnO nanowire. Thus, there is a direct correspondence between enhanced ZnO emission and the presence of the Ag nanoparticles.

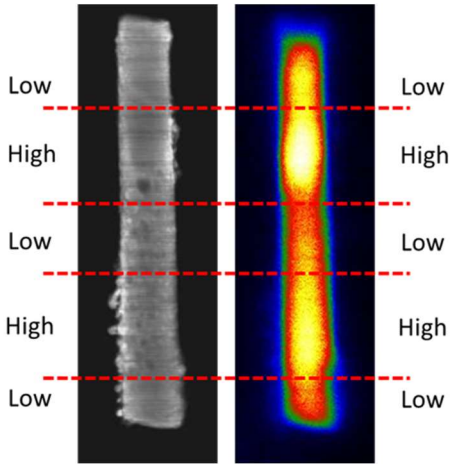

Figure 4.2 (left) High-resolution high-angle annular dark-field (HAADF) and (right) cathodoluminescence (CL) spectrum-images(SI) of an Ag coated ZnO-MgO core-shell nanowire. The HAADF image shows alternating areas of high and low Ag-nanoparticle coverage along the length of the nanowire. The CL-SI shows higher concentration of Ag nanoparticles correspond to the most intense ZnO nanowire emission.

Additional Ag coated ZnO nanowires were fabricated following the techniques outline in Section 2.1 in order to develop additional CL and HAADF results. A thin nanowire with a large Ag nanoparticle was studied to determine if plasmons from an individual nanoparticle can be isolated and if coupling to the ZnO nanowire excitions can be observed on a local scale. Figure 4.3.a-b shows an HAADF and CL-SI image of this a nanowire from this sample. The intensity of the CL emission from the Ag coated nanowire directly corresponds to the position of the two large Ag nanoparticles on the sample, which indicates that plasmon modes in the nanoparticle are being excited by the electron beam.

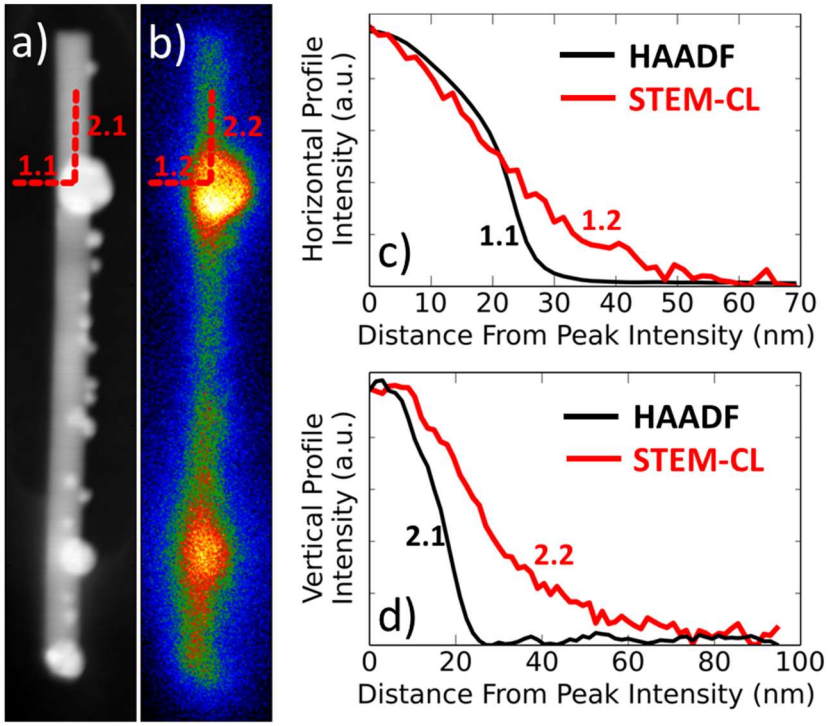

Figure 4.3: Scanning transmission electron microscopy (STEM) of a ZnO nanowire coated with Ag nanoparticles imaged in a) high-angle annular dark field (HAADF) mode and b) STEM cathodoluminescence (CL) mode shown as a spectrum image (SI). Linescans of the intensity of the HAADF image and CL-SI were taken along c) horizontal paths 1.1, 1.2 and d) vertical paths 2.1, and 2.2. The STEM-CL has a broader intensity than the HAADF in both the horizontal and vertical profile, however, in the vertical profile, which runs along the ZnO nanowire, the STEM-CL scan is twice as broad as in the horizontal profile, which runs from the vacuum onto the Ag nanoparticle.

To determine if the excited Ag plasmons are coupled to excited ZnO excitons, two linescans of the HAADF and CL-SI intensity were measured and compared, Figure 4.3.c-d. The first linescan runs perpendicular to the nanowire length, starting in vacuum and ending on the middle of the Ag nanoparticle. It shows that there is enhanced emission in the STEM-CL, visible by the broader width (15 – 20 nm broader) of the Ag nanoparticle in the CL-SI than in the HAADF. This enhanced emission in the vacuum is due to non-local excitation of the Ag nanoparticle, because as the focused electron beam approaches the nanoparticle it may be possible to excite plasmons. The linescan parallel to the ZnO nanowire length running to the middle of the Ag nanoparticle determines if the enhanced emission from the Ag nanoparticle also

has a component due to Ag plasmons coupling to ZnO excitons. Indeed, the width of the CL-SI emission in the vertical direction is 30 – 40 nm broader than the width of the nanoparticle in the HAADF image. This is double the horizontal linescan width, proving that non-local excitation is not the only mechanism leading to enhanced emission from the Ag coated ZnO nanowire, and that there is a coupling between the excitation in the ZnO nanowire and the excitation in the Ag nanoparticle. These STEM-CL data confirm the conclusions based on the photoluminescence data discussed in Chapter 3; that the Ag plasmons enhance the radiative emission rate of ZnO excitons and lead to enhanced emission from the ZnO nanowires, as concluded in Chapter 3.

4.3 Complementary Spectroscopy

This cathodoluminescence study of large Ag nanoparticles on ZnO nanowires leads to the extravagant discovery that random morphology plasmonic nanoparticles can be fully characterized through a study of STEM-CL coupled with STEM-EELS. The combination of spatially-resolved EELS and CL in a STEM can be used to access three-dimensional experimental data for the surface plasmon modes of an individual nanoparticle without need for reconstruction or simulation.[30] The combination EELS/CL embodies a powerful complementarity that can be used to extract three-dimensional information about the plasmonic response not available from either spectroscopy individually, because EELS measures beam-induced electronic excitation, while CL measures radiative decay. In complex nanostructures with non-uniform dimensions, EELS is dominated by volume effects while CL is dominated by surface effects, permitting us to measure and identify distinct plasmon modes in all three dimensions directly from experimental data. We exploit this complementarity to analyze the plasmonic response of Ag nanoparticles that are decorating the ZnO/MgO core/shell nanowires.

We then validate the joint EELS/CL analysis by full-field, finite-difference, time-domain (FDTD) simulations to demonstrate that the peaks observed in the two-dimensional experimental maps have the same spatial profile and peak positions as computed plasmon spectra, and thus correspond to plasmons in all three spatial dimensions.[162] Moving forward, such experiments will not require the corroboration of the FDTD simulations results, as the complementary spectroscopy technique gives a more accurate representation of the 3D plasmonic response of a nanoparticle with random morphology than the simulations do.

4.3.1 Complementary Spectroscopy Methods

The focus of this work is to demonstrate that the combination of the EELS and CL spectroscopies provides information about the surface plasmon modes of a single nanoparticle that cannot be accessed by either technique individually. Here we present the analysis of a single nanoparticle to demonstrate that by the use of STEM EELS/CL the three-dimensional analysis of individual plasmonic elements in a complex multiple-element system can be obtained. The Ag nanoparticles on the chosen ZnO/MgO core-shell nanowire have characteristic lateral dimensions ranging from 2–5 nm to more than 100 nm. Most nanoparticles are roughly hemispherical in shape, but there is no predictable symmetry or orientation with respect to the nanowire axis. A nanowire with a thick MgO shell (~70 nm) was selected to ensure that the nanoparticle is insulated from the wire and isolated from hot-electron-transfer effects and plasmon–exciton interaction with the ZnO.[28] The nanoparticle studied here had high aspect ratios resulting in the splitting of the three dipole modes, and had the most complete data set from which to demonstrate this aspect of the joint EELS/CL analysis.

The STEM-CL spectra were acquired as discussed in Section 4.2 and exhibited in Figure 4.1. Figure 4.1 also shows the HAADF and EELS configuration. The EELS experiments were performed on a Nion Ultrastem200 STEM operated at 200 kV and less than 20 pA, equipped with a Gatan Enfinium EEL spectrometer. For SI a constant background subtraction method was applied, meaning the difference between the integrated intensity from a 0.1 eV range centered at each peak and the integrated intensity across a 0.1 eV background region from just below each peak is the displayed intensity on the SI. We employ this method so that when the background region has a higher integrated intensity than the peak region no signal is recorded. All black pixels correspond to background regions having a higher average intensity than the signal regions. All EELS–SIs are acquired with a 0.2 s integration time. The nanoparticle is re-examined directly after each EELS- and CL- SI acquisition to check that plasmon resonances are relatively unchanged by beam damage. After acquisition, all spectral features were observed to have approximately the same peak amplitudes, locations and widths.

Plasmonic excitations are detected and mapped in different ways in EELS and CL. In plasmon maps generated by both techniques, the spatial location of the plasmon intensity is determined by position of the probe when the fast electrons in the beam scatter inelastically from the conduction-band electrons of the metal.[163-166] However, the plasmon signature measured by EELS is the energy lost during transmission through the sample, which directly relates to the combined sum of the energies for all the excitations generated by each beam electron during transmission. As a result, EELS is sensitive to all plasmons, including 'dark', high-angular-momentum plasmon modes that cannot decay radiatively and high-energy plasmon modes that decay outside the visible spectrum.[167-169] On the other hand, CL spectra incorporate signals only from the radiative decay of the beam-induced excitations. This limits CL to electronic excitations

that effectively out-couple to photons that fall within the detectable range of the spectrometer, thereby directly yielding information about the efficiency of individual plasmon absorption or emission modes.[167,170-172] As a result, the detected plasmonic response can differ greatly when comparing EELS to CL even in the same system, especially in complex geometries with varying thicknesses.

The crux of the current experiment is the determination of the spatial distribution of plasmon response through the construction of a spectrum image (SI) of the nanoparticle and the difference between the SIs collected in STEM–EELS and -CL. When the spatial scan is complete, one obtains a 3D data set with two spatial dimensions and one energy dimension. To form 2D images, slices are taken across the energy dimension, and the integrated intensity over a given spectral range is converted into the pixel intensity, allowing the mapping of specific optical features. The spatial resolution is limited by the confinement of the plasmon to the surface of the nanoparticle, which is 5–10 nm for EELS, and 10 – 20 nm for CL (to avoid damaging the sample due to the larger current used for CL).

4.3.2 Complementary Spectroscopy Results

Differences between plasmon detection in EELS and CL result in some peaks being visible in both spectroscopies, while some are only observed in one or the other. Thus, the complementary nature of EELS and CL spectroscopy are taken advantage of for the duration of this study to determine the three-dimensional plasmonic characteristics of a random morphology nanoparticle.

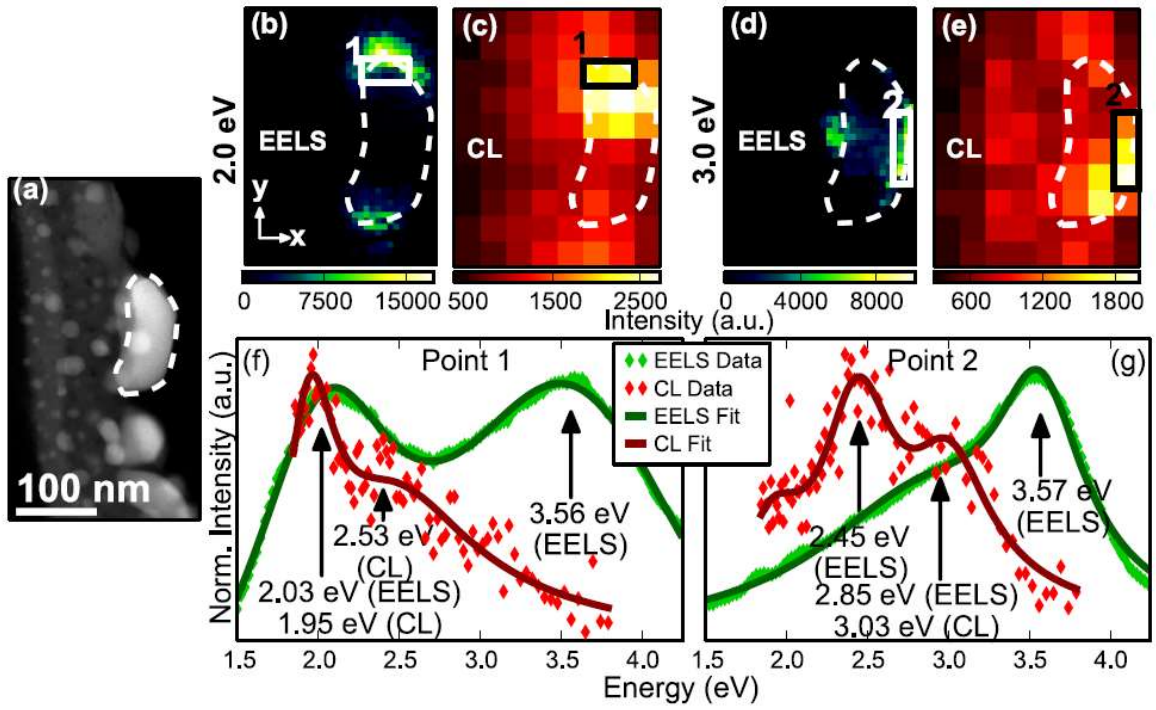

Figure 4.4: Plasmon modes observed in both CL and EELS. a) High-angle annular dark field (HAADF) image of an Ag nanoparticle on the surface of an insulating nanowire. b)–e) Spectrum images (SIs) of the plasmon modes present in both electron energy loss spectroscopy (EELS) and cathodoluminescence (CL). b) EELS and c) CL – SIs respectively, of a long-axis (LA) plasmon mode (along the y-axis) at 2.0 eV. d) EEL and e) CL–SI, respectively, of a short-axis (SA) plasmon mode (along the x-axis) at 3.0 eV. f)-g) Representative spectra are taken from the boxed regions (1 and 2) of maximum intensity of the two spectra.

We start by examining modes present in both spectroscopies. In Figure 4.4 we examine a large random-morphology Ag nanoparticle on the surface of the ZnO/MgO nanowire, comparing the plasmonic modes that appear in both in EELS and CL. The nanoparticle's plasmonic response is mapped in SIs in Figure 4.4.b-e with representative spectra of the plasmon modes being shown in Figure 4.4.f-g. Peaks near 2.0 eV (centered at 2.03 eV in EELS and 1.95 eV in CL) and 3.0 eV (2.87 eV EELS, 3.07 eV CL) appear both in EELS and CL. By comparing the SI slices for these peaks in EELS to the CL slices, the higher detection efficiency and spatial resolution of EELS can be exploited to identify the precise location of the resonance. The 2.0 eV plasmon is localized at the top and bottom of the nanoparticle, while the 3.0 eV peak is localized along the sides, indicating that the nanoparticle exhibits the characteristic response of an

ellipsoidal nanoparticle; the longitudinal dipole surface plasmons are split into top-to-bottom, long-axis (LA) and side-to-side, short-axis (SA) modes. Due to the irregularity of the nanoparticle selected for this measurement, asymmetries are introduced into the detected plasmon intensity. The CL–SIs shows where on the nanoparticle each mode is most strongly excited by the electron beam. The locations of the intensity maxima are confirmed in EELS, where stronger excitation is observed on the right-hand side of the nanoparticle for the SA plasmon, and on the top of the nanoparticle for the LA plasmon.

It is worth noting that both extrema of the plasmonic resonance are observed in EELS, but not in CL, probably due to the lower signal-to-noise ratio in CL. There is still measureable CL intensity at the bottom and left-hand side of the nanoparticle, but the resonance is too weak to be sufficiently distinguished from the background noise. There are two likely root causes for the asymmetry in the plasmon intensities at the nanoparticle edges: a thickness variation in the nanoparticle and the presence of the MgO spacer. The discrepancy in CL intensity between the top and the bottom of the nanoparticle seems to be a result of the non-uniform thickness. The particle is thicker on the top than the bottom, resulting in increased signal from both spectroscopies on the top side of the nanoparticle. The MgO spacer affects all plasmon modes by altering the dielectric environment of the nanoparticle. However, the SA mode, especially when excited from the left side, is particularly affected and suffers a reduced intensity due to the presence of the MgO, which damps the electric field of the plasmon resonance and reduces the electromagnetic coupling to the electron beam.

Next we examine plasmon modes present only in EELS. In Figure 4.4.f-g, peaks at 3.56 eV and 3.57 eV, respectively, were observed in EELS, with no corresponding feature in CL. The data also reveal another such peak at 3.78 eV. Figure 4.5 shows the SIs for each mode and

the spectra corresponding to each. The nature of both of these peaks is well known from previous research; they correspond to the transverse surface plasmon at 3.6 eV (Figure 4.5.b) and the bulk plasmon at 3.8 eV (Figure 4.5.c) of Ag.[149,173] Neither of these two modes are geometry dependent. The bulk plasmon would be observed in any Ag sample, and the transverse plasmon is generally present at the surface of any Ag nanoparticle.[174] The mode can be detected around the entire perimeter of the nanoparticle even where little to no intensity is visible in the SI. The differences in intensity for the transverse plasmon SI arises because the electron beam is transmitted through a thick MgO layer on one side of the nanoparticle, but only through the thin supporting carbon grid on the other, which significantly affects the total detected intensity. The wavelengths corresponding to these plasmons are too far into the ultraviolet to be efficiently detected in the CL spectrometer available in this experiment, while the detectable range of EELS is not limited to the visible regime. However, because they are undetectable in CL we are not able to use the combined CL/EELS for these modes. Their presence in the EELS spectra, however, helps in the combined CL/EELS analysis of the other plasmon modes.

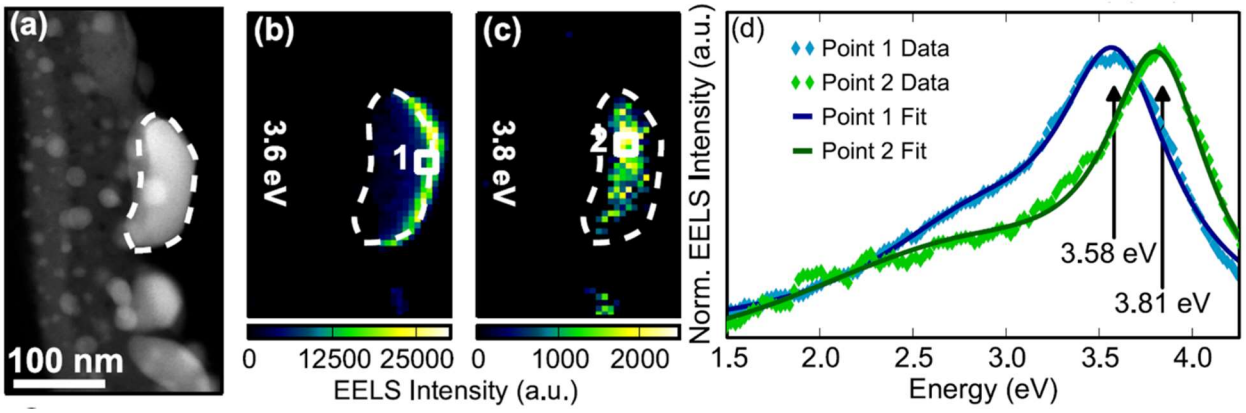

Figure 4.5: Modes observed only in EELS. a) HAADF image of the nanoparticle. b)-c) Spectrum images (SIs) of the two plasmon modes only observed in EELS at 3.6 eV and 3.8 eV, respectively. d) The EEL spectra from points 1 and 2 marked on b) and c). The two peaks refer to the transverse and bulk plasmons modes in Ag.

Finally, we analyze a feature present in CL but not EELS. Figure 4.6, as well as both spectra in Figure 4.4, shows a CL peak near 2.5 eV that has no corresponding EELS peak. From the CL–SI in Figure 4.6.b, it is evident that the 2.5 eV peak has a unique spatial localization, completely distinct from the LA and SA plasmon modes shown in Figure 4.4.c,e, indicating that it must be a separate plasmonic feature. The EEL and CL spectra from the center of the nanoparticle, shown in Figure 4.6.d, demonstrate that the 2.5 eV CL peak centered at 2.48 eV is not observed in EELS, where only the bulk plasmon is detected. Figure 4.6.c shows an EEL–SI at 2.5 eV, and while some intensity can be seen in the SI, those same locations correspond to the high intensity regions of the SA plasmon in Figure 4.4.d. Due to the constant background subtraction method employed in the SI, the tail of a dominant plasmon can result in detected signal in the SI. As a result, the EELS signal detected at 2.5 eV is more likely to be due to the tail of the SA plasmon rather than a unique 2.5 eV plasmon.

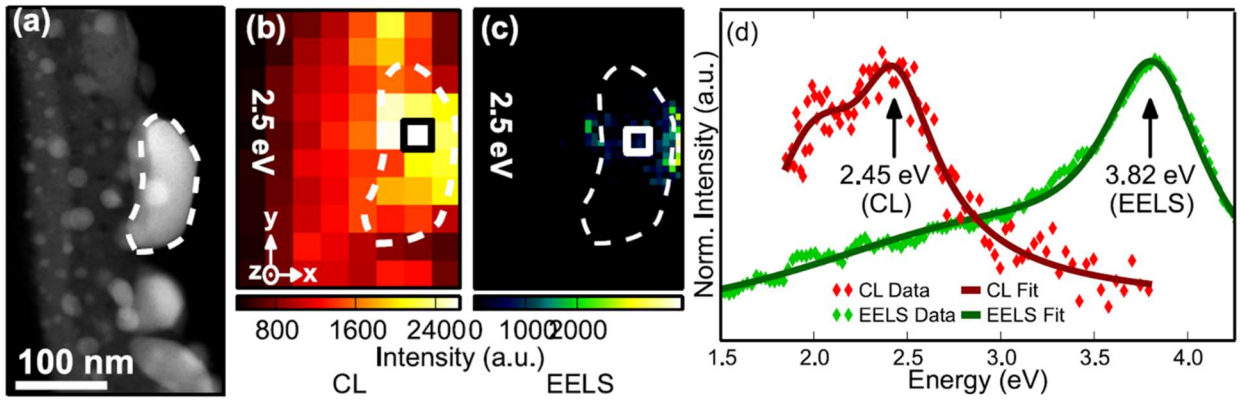

Figure 4.6: Modes observed only in CL. a) HAADF image of nanoparticle. b) CL–SI of the 2.5 eV peak observed in CL but not EELS. c) EEL–SI at 2.5 eV. Intensity is only observed in the EEL-SI in regions where the 3.0 eV SA plasmon has high intensity, thus the 2.5 eV EEL–SI is mainly due to the tail of the SA plasmon. d) CL and EELS spectra from the center of the nanoparticle. Here, the EEL spectra is dominated by the bulk plasmon. CL is dominated by surface effects, demonstrating that the 2.5 eV feature is a surface effect localized above the bulk of the nanoparticle.

In order to understand why the peak is present in one spectroscopy but not the other, we invoke the core distinction between EELS and CL: excitation versus radiative decay. One of the most important consequences of the distinction is how the signals of the two spectroscopies react to multiple electron–sample interactions. First, the total EELS intensity across the entire spectrum decreases when the electron beam interacts with the bulk, since a large portion of the electrons are elastically scattered to high angles and do not enter the spectrometer. Furthermore, EELS requires single-interaction events for the measured energy loss to be directly interpretable. If the beam interacts multiple times with the sample during transmission, the measured energy loss has contributions from each interaction and the true value of each energy-loss event is obscured. Thus, even though the total plasmonic excitation may be strong in a thick part of the sample, the detected plasmonic EELS signal is strongest, and most directly interpretable, along the edge of the nanoparticle. At that spatial location, the electron beam couples via the evanescent plasmon field and excites the plasmon non-locally without interacting with the bulk of the nanoparticle, allowing for efficient single-interaction plasmon excitations.[167]

In contrast to EELS, multiple interactions and elastic scattering do not attenuate the CL signal. Surface plasmons and other radiative decay events are captured regardless of subsequent beam-sample interactions, because emitted photons, rather than transmitted electrons, are detected in CL. In fact, bulk luminescence effects can be attenuated in CL as the emitted photons are subject to reabsorption in the low-skin-depth metals, while surface luminescence, such as that from surface plasmons, is efficiently captured.

In STEM, or any other electron beam technique, the strength of the plasmonic excitation from the electron beam is determined by the strongest inelastic scattering from the surface plasmon mode. However, the strength of the detected EELS intensity is determined by the area

of most efficient, single-interaction excitation, while the detected CL intensity is determined by the strongest plasmonic excitation of the observed mode. So the strongest CL intensity should occur at the thickest part of the nanoparticle where the studied plasmon mode is active (i.e. on the top and bottom of the nanoparticle for the LA mode). Recall that the EEL–SIs show the strongest plasmon intensity outside the boundaries of the nanoparticle while the CL–SIs show the strongest intensity within the boundaries. The distinction between the ways EELS and CL detect plasmons explains why the 2.5 eV plasmon is not observed in EELS.

From the inherent characteristics of the two spectroscopies, it can be said that when the electron beam is transmitting through a thick sample, the EELS signal only shows bulk effects strongly, while the CL can still show the surface effects. Since the 2.5 eV peak is strongly detected in CL, but is unresolvable as an individual peak in EELS, the peak can be determined to be a surface effect localized above the bulk of the nanoparticle. The feature is probably plasmonic, as the CL spectra shown in Figure 4.4 demonstrate it has an amplitude and width comparable to the LA and SA modes. Longitudinal, out-of-plane (OOP) plasmons have been shown to be strongly active in CL, and such a mode would exhibit the type of localization observed in the CL–SI.[171,172,175] The supporting evidence indicates that the 2.5 eV peak is an OOP plasmon mode, and with this identification, we have now determined experimentally the characteristic frequency, spatial distribution, and location of peak intensity for the dominant longitudinal plasmon modes in all three dimensions, without reconstruction or simulation.

4.3.3 Comparison of Experimental and Theoretical Analysis

To confirm the preceding experimental analysis of the plasmon peaks in the random morphology nanoparticle, FDTD simulations were compared to the spectroscopic data. The morphology of the nanoparticle is not precisely known, and hence direct simulation of the exact plasmonic response is not possible. However, approximating the morphology of the nanoparticle in a simpler geometry and comparing simulations to the experimental results can validate the experimental analysis by demonstrating that the simulated plasmon response of the simplified geometry with a precisely known plasmonic response is similar to that of the unknown geometry with an experimentally determined plasmonic response.

In order to approximate the size and shape of the nanoparticle and simulate its plasmonic response, we invoke information about the nanoparticle that has already been established. A half-ellipsoid on an MgO substrate is chosen to represent the nanoparticle for two reasons. Firstly, the shape is likely quasi-ellipsoidal. The splitting of the LA and SA modes is a common feature in ellipsoidal nanoparticles and the splitting observed in this experiment is similar to those established in literature.[176] Secondly, a half-ellipsoid is chosen as opposed to a full ellipsoid since the MgO shell, on which the Ag particle is deposited, is flat. The *x*- and *y*-dimensions of the half-ellipsoid are measured from calibrated scanning transmission electron microscopy images, and are found to be 72 nm and 138 nm, respectively. For the *z*-dimension, the EEL–SI can be used to determine the thickness of the nanoparticle. A thickness map of the nanowire/nanoparticle assembly is generated on each spectrum in the SI,[30] which determines a physical thickness of approximately 100 nm for the Ag nanoparticle.[177] This thickness map also shows that the depth at the top of the nanoparticle is greater than the bottom, which offers a plausible explanation for the localization of the LA plasmon mode at the top of the nanoparticle.

If the nanoparticle is thicker at the top than the bottom, the inelastic scattering cross section for the plasmon should be higher at the top than at the bottom and the detected plasmonic intensity should be stronger. This highlights the importance of a purely experimental analysis for unknown geometries, as morphological variations such as curvature or sharp edges can also affect the plasmonic intensity significantly.[178-180]

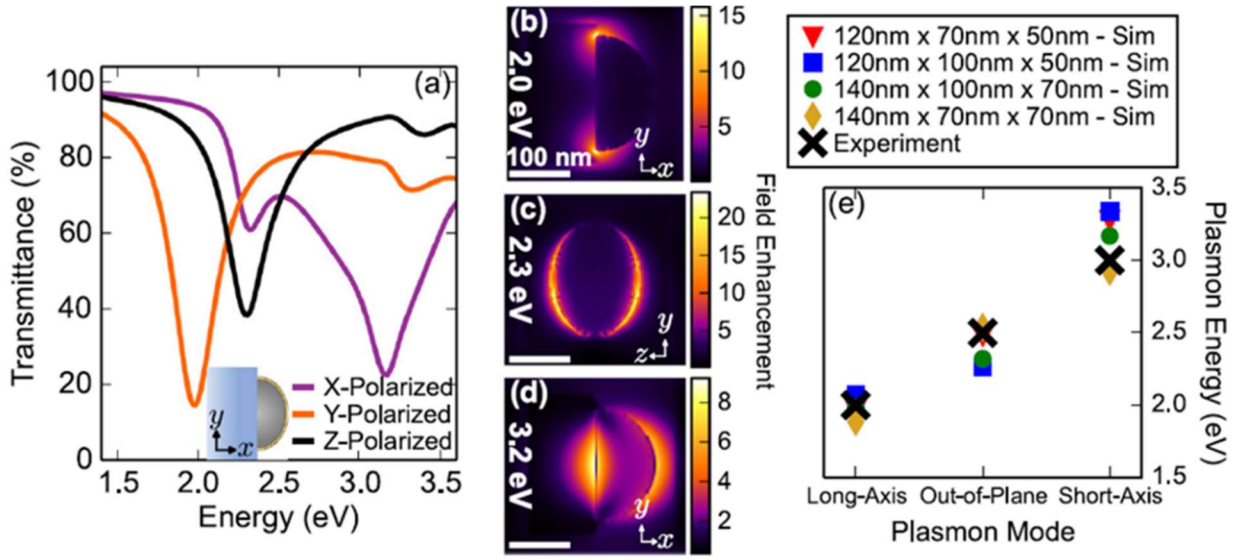

Figure 4.7: The plasmonic response of a half-ellipsoid Ag nanoparticle on a MgO substrate with is determined through finite-difference time-domain calculations. a) Transmission data from plane waves polarized at different orientations to the main axes of the nanoparticle. Three plasmon peaks are observed at 2.0, 2.3 and 3.2 eV. b)–d) The resulting plasmonic field enhancement maps, with modes corresponding to b) a 2.0 eV LA mode, c) a 2.3 eV OOP mode, and d) a 3.2 eV SA mode. Simulations are performed on multiple variations of the nanoparticle size in all three-dimensions. e) The results of these simulations are compared to the values for the three experimental plasmon modes, and the experimental values fall within the predicted range determined from the simulations.

With the approximate dimensions of the nanoparticle determined (140 nm × 100 nm × 70 nm), simulations of the plasmonic response of the nanoparticle become credible. In Figure 4.7, a three-dimensional Maxwell equation solver (Lumerical FDTD Solutions®), is used to analyze Ag half-ellipsoids on an MgO substrate. Additionally, the samples were not kept in vacuum, so a 1.6 nm shell of AgS_2 was included to simulate the experimentally measured effect

of Ag tarnishing in atmosphere.[181] The Maxwell equations were solved for each orientation of the three principal axes of the nanoparticle relative to the polarization of the exciting plane wave. The nanoparticle, and the 170 nm × 170 nm × 80 nm MgO film it was on, were rotated together to allow each polarization to be measured. A 300 nm × 300 nm × 800 nm simulation region was bounded by period boundaries. A plane wave was injected along the z-axis for all simulations, rotating the polarization between x and y and the position of the nanoparticle to achieve all six desired polarization excitations (3 redundant). A wavelength range of 200 – 1200 nm was used for the field transmission, and a mesh with a 2 nm smallest mesh element defined the solution regions. These six-fold simulations were repeated for four nanoparticle sizes due to the unknown morphology of the physical nanoparticle.

The plasmonic response of the system to plane waves polarized along the major axes of the ellipsoid is calculated and shown in Figure 4.7. The resulting transmission data for a nanoparticle, with dimensions of 140 nm × 100 nm × 70 nm, are shown in Figure 4.7.a. The plot exhibits three distinct plasmon peaks appearing at 1.98 eV, 2.32 eV, and 3.17 eV. By plotting the electric field enhancement of the plasmon modes of each resonance (Figures 4.7.b-d) we can see that they correspond to LA (1.98 eV), OOP (2.32 eV), and SA (3.17 eV) plasmon modes. Given that the thickness measurements and the nanoparticle geometry are approximate, the three plasmon modes are also calculated for half ellipsoids of slightly different sizes to establish a spectral range in which each of the plasmons appear. The three other half-ellipsoid dimensions are: 120 nm × 70 nm × 50 nm, 120 nm × 100 nm × 50 nm, and 140 nm × 70 nm × 70 nm. The plasmons corresponding to the half-ellipsoids are: LA-1.97 eV/OOP-2.49 eV/SA-3.29 eV, LA-2.07 eV/OOP-2.26 eV/SA-3.34 eV, and LA-1.88 eV/OOP-2.54 eV/SA-2.92 eV. The simulated and experimental values are plotted together in Figure 4.7.e. It can be seen that the experimental

values of 2.0 eV, 2.5 eV, and 3.0 eV and fall entirely within the range of values established by simulations.

The size variations in the simulated nanoparticles are significantly larger than the predicted error in the experimental measurements of the nanoparticle size, because the precise morphology of the nanoparticle is not known and morphological differences can account for significant variations in the plasmon mode energies as well. A larger range of half-ellipsoid dimensions is taken to establish a larger range over which the various plasmon modes can deviate under geometric variance. The measurements of the nanoparticle size in Hachtel, *et al*,[30] show that while the nanoparticle is not a perfect half-ellipsoid, the geometry is reasonably similar, and the geometrically determined plasmon modes should therefore be similar as well. The agreement between experimental data and the theoretical predictions is not a direct comparison of the two plasmonic models, as much as a sanity check that the experimental analysis is yielding physically reasonable results for a quasi-ellipsoidal structure. The experimental modes falling directly into the range established by the simulations indicate that the experimental joint EELS/CL analysis of the dominant nanoparticle plasmon modes is consistent with the plasmonic behavior of a nanoparticle of similar geometry. Furthermore, the simulations confirm that an experimental analysis based on the complementary physical origin of the two spectroscopic signals, without simulations, on a nanoparticle with an unknown morphology, gives information on the plasmonic response of complex nanostructures. The amount of information obtained in this phenomenological approach is comparable to what is obtainable from an experimental analysis of nanoparticles with predetermined morphologies, undergirded by electromagnetic simulations.

4.4 Conclusions

The combination of STEM-CL and STEM-HAADF measurements confirmed the plasmon-exciton coupling in the Ag coated ZnO/MgO nanowires from Chapter 3. We then further demonstrated, in a single Ag nanoparticle, that the complementary combination of STEM - EELS and - CL allows differences between the two spectroscopy techniques to be analyzed as additional data sets. This complementarity has already been used to categorize 'bright' and 'dark' plasmons,[156] and in the current experiment we demonstrate how the complementary combination of EELS and CL yields a picture of the three-dimensional plasmonic response in a random-morphology nanoparticle. These results demonstrate one potential method for characterizing the complex plasmonic response of the nanoparticles coating our ZnO nanowire systems.

4.5 Acknowledgements

For the microscopy experiments in this chapter, I thank Dr. Jordan Hachtel. This work would not have been possible without his expertise on the STEM-CL and STEM-EELS system at Oak Ridge National Laboratories. I also thank Jordan for preparing the text of this Chapter, minus the section focused on my own simulation work, for publication. I thank Prof. Daniel Mayo for being lead on the collaboration with Jordan while I was away in China. And finally I thank Jordan, Dan, Prof. Richard Haglund, and Prof. Sokrates Pantelides for the in depth discussions we had on plasmonics while working on the submission of this paper.

CHAPTER 5

ZNO-MGO CORE-SHELL NANOWIRE MORPHOLOGY

In this section the effect of the interface quality of ZnO/MgO core-shell nanowires on the ZnO band-edge emission photoluminescence enhancement is examined. ZnO nanowires with an MgO shell exhibit enhanced band-edge photoluminescence (PL), a result previously attributed to passivation of ZnO defects. However, we find that processing the ZnO nanowires under low oxygen partial pressure leads to a PL enhancement dependent on MgO thickness due to the formation of optical cavity modes. Conversely, processing under higher oxygen partial pressure leads to nanowires that support neither mode formation nor band-edge PL enhancement. High-resolution electron microscopy and density-functional calculations implicate the ZnO *m*-plane surface morphology as the key determinant of core-shell structure and cavity-mode optics. A ZnO surface with atomic steps along the *m*-plane in the *c*-axis direction stimulates the growth of a smooth MgO shell that supports guided-wave optical modes and enhanced UV PL. On the other hand, a smoother ZnO surface leads to nucleation of a rough cladding layer which supports neither enhanced UV PL nor optical cavity modes. These results point the way to fabricating ZnO/MgO core-shell nanowires for more efficient UV nanolasers, scintillators, and sensors. This work is published:[32]

- **C.E. Marvinney**, X. Shen, J.R. McBride, D. Critchlow, Z. Li, D.C. Mayo, R.R. Mu, S.T. Pantelides, R.F. Haglund, *Effect of Material Structure on the Photoluminescence of ZnO/MgO Core-Shell Nanowires,* ChemNanoMat, 2018. **4**(3): p. 291-300.

5.1 Background on MgO Thickness Dependent Photoluminescence

Interest in zinc oxide (ZnO) nanowires, given a band gap of 3.37 eV and exciton binding energy of 60 meV, is predicated on the potential for ultraviolet optoelectronic and photonic devices, such as nanolasers and sensors.[1,2,7-9,15,38] Of the various ZnO nanostructures,[8] nanowires offer a highly crystalline nanostructure that in principle supports both guided-wave luminescence[21,22,132] and optical cavity modes.[23,24,123,182] When decorated with metal nanoparticles, the photoluminescence yield can also be enhanced by the Purcell mechanism due to exciton-plasmon coupling.[21,25-27,183,184] Thus, ZnO nanowires are an attractive architecture for optoelectronic and optical devices, because optical confinement and waveguiding can lead to enhanced photoluminescence (PL), electroluminescence, and lasing.[11,33-37,88,185,186]

In addition to strong ultraviolet (UV) band-edge (BE) exciton emission, ZnO also exhibits broadband visible emission due to surface defects and deep trap states.[20,81,82,187] A capping or shell material is often used to passivate these surface defects, reducing the visible defect emission while enhancing the UV BE emission.[188-198] There is general agreement that MgO passivation of ZnO surface defects increases the ratio of band-edge to visible emission. However, previous work has also shown that band-edge PL enhancement also depends on the MgO thickness, and fundamentally different conclusions have been reached about the mechanism that leads to this result.[31,61,119,199,200] The mechanisms for PL enhancement as a function of MgO thickness include passivation of surface dangling bonds (Meng *et al.*[199] and Wu *et al.*[119]), reduced band-bending from type-I band alignment (Meng *et al.*[199] and Shi *et al.*[200]), formation of a quasi-quantum-well-like structure (Shi *et al.*),[200] and lattice mismatch induced strain (Vega *et al.*[61]). In both Wu[119] and Shi,[200] the core-shell nanowire enhancement disappeared for the thickest MgO shells, ascribed to dispersive losses and scattering from the

non-uniform coating formed by the thicker MgO cladding layer. Table 5.1 compares the parameters of the ZnO/MgO core-shell nanowires and the UV band-edge enhancement from references [31,61,119,199,200].

Table 5.1 MgO thickness dependent photoluminescence (PL) enhancement from ZnO/MgO core-shell nanowires (NWs).

Reference	ZnO NW Thickness [nm]	MgO Coating Thickness [nm]	PL Enhancement (Coated NW / Uncoated NW)
Meng *et al.*, 2009[199]	100	10	~ 2.4
		~ 20	~2.5
		~ 40	~ 2.5
Wu *et al.*, 2012[119]	30	25	~10
		~60	1 – 2
Mayo *et al.*, 2014[31]	90	20	15
		40	3
		60	18
Shi *et al.*, 2015[200]	36	5	1 – 2
		15	~ 7
		25	1.3
Vega *et al.*, 2017[61]	60	7	~ 10
		14	~ 50
		20	~ 80

In contrast to references 119,199,200, and 61, Mayo *et al.*[31] showed a bimodal PL enhancement dependent on MgO thickness with a minimum at 40 nm MgO thickness and 15-fold enhancement maxima at MgO thicknesses of 20 nm and 60 nm. This bimodal enhancement, which varies smoothly as a function of MgO thickness was not observed in the other studies,[61,119,199,200] and was attributed to the formation of optical cavity modes.[23,31,123] Thus the formation of optical cavity modes provides a mechanism for enhanced band-edge PL beyond that due to ZnO surface passivation and band bending.

These facts motivate the present experimental and theoretical investigations of the influence of the MgO and ZnO surfaces and morphology on the formation of cavity modes and the concomitant UV PL enhancement. Finite-element analysis shows that the formation of optical modes leads to the observed dependence of ZnO band-edge PL enhancement on MgO thickness. Depending on the surface and interface conditions of the ZnO/MgO core-shell nanowires, either propagation or scattering of the optical cavity modes is allowed, in which either mode propagation leads to PL enhancement, or scattering prevents it. Density-functional theory identifies the particular morphologies of the ZnO/MgO interfaces that provide conditions for either scattering or for propagation of optical modes. These results show that optical performance of the core-shell nanowires depends critically on the processing phase space for the deposition of the ZnO and MgO.

5.2 Photoluminescence

5.2.1 Bare ZnO Nanowires

The two growth protocols for the ZnO nanowire samples are compared in Chapter 2, Table 2.2, showing that the protocols must be situated at slightly different locations on the ZnO temperature-pressure phase diagram. The first growth protocol featured a lower oxygen pressure (LOP), shorter growth time, and higher initial temperature than the second growth protocol, which was named for its higher oxygen pressure (HOP). The longer growth time of the HOP protocol yielded nanowires roughly 60 % longer than those of the LOP protocol (Table 2.3). Other than differences in length, the SEM analysis (methods discussed Section 2.1.1) shows that the two protocols yielded similar nanowires. However, it is well known that even slight changes

in the temperature-pressure conditions can lead to significant changes in the resulting ZnO nanostructure, crystalline quality, and PL.[18-20]

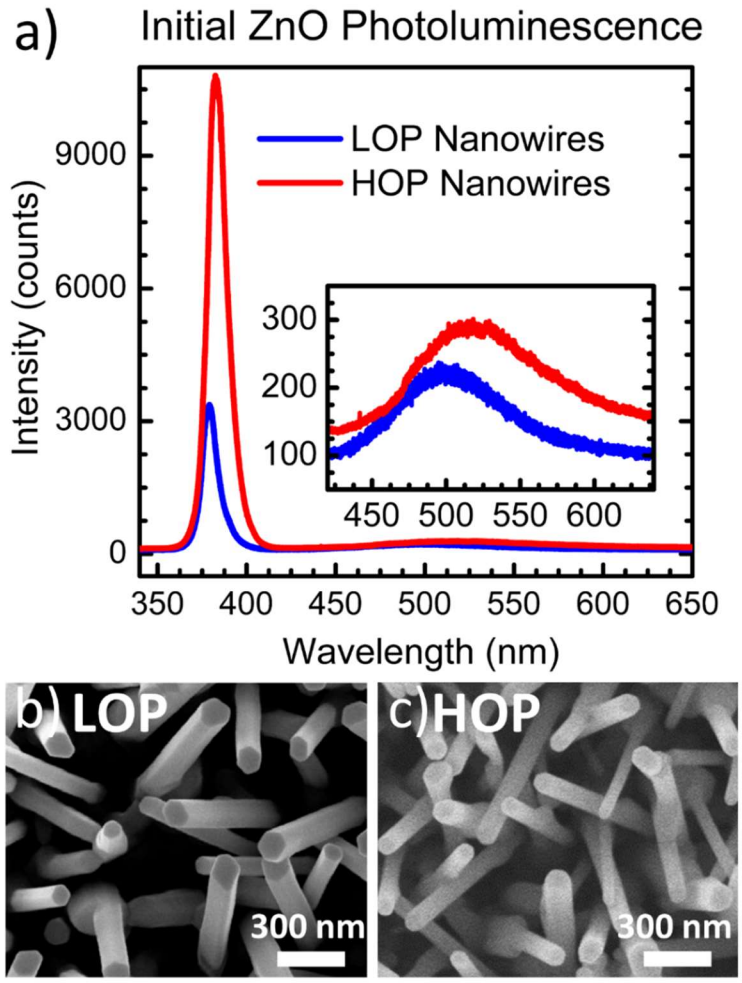

Figure 5.1: (a) Photoluminescence spectra of the bare ZnO LOP and HOP nanowires, with inset showing the intensity range of the visible emission. High resolution scanning electron micrographs (SEM) of a sample grown under (b) LOP protocol (Raith SEM) and (c) HOP protocol (Merlin SEM). The hexagonal shape of the nanowires is clearly visible in both samples, with the (0001) *c*-plane top facet and $(1\bar{1}00)$ *m*-plane sidewall facets of wurtzite ZnO.

These differences in quality are seen in the PL spectra of the LOP and HOP nanowires, Figure 5.1.a. The PL measurements used the 325 nm spectral line of a HeCd laser (Kimmon, 1K

series) as the excitation source. The measured power at the sample is 6.0 mW, focused onto the sample with a 15X UV objective lens. A spectrometer (HORIBA Jobin Yvon LabRAM 800HR) was used with a -40 °C thermoelectrically cooled CCD camera as the detector. Each PL spectrum was collected in the wavelength region from 340 nm – 700 nm using an 1800/mm diffraction grating. The LabSpec Version 5.78.24 software was used to average ten measurements for the LOP nanowires and four for the HOP nanowires, always with an integration time of 0.2 s. Variations in the homogeneity of the ZnO nanowires were accounted for by averaging the total PL yield from multiple locations per MgO thickness region per sample, leading to the calculated variance in the experimental PL enhancement.

In Figure 5.1.a., the ratios of the integrated BE to visible-defect emissions are 1.44 and 3.45 for the LOP and HOP nanowires, respectively. Moreover, the HOP nanowires have more than double the BE-to-visible emission ratio of LOP nanowires, meaning that the ZnO nanowires grown under the HOP protocol exhibit higher crystalline quality and have potentially fewer surface defects than those grown under LOP conditions.[18,20] But in spite of this, the MgO-coated HOP nanowires exhibit *lower* PL enhancement than the MgO-coated LOP nanowires.

5.2.2 ZnO/MgO Core-Shell Nanowires

The ZnO nanowires selected for photoluminescence measurements had almost identical diameters of approximately 90 nm (Table 2.3), thus facilitating optical cavity mode formation when coated with MgO at shell thicknesses from 0 to 70 nm in 10 nm increments (fabrication of the ZnO/MgO core-shell nanowires is given in Section 2.1.2).[31] The bare nanowires exhibit the hexagonal morphology of single-crystal wurtzite ZnO, Figure 5.1.b-c**,** typical of all samples

grown for this study. Simulations of a hexagonal cavity in the LOP nanowire (Section 3.2.4) demonstrate that formation of Fabry-Perot and whispering-gallery optical cavity modes depends critically on the diameter of the combined ZnO/MgO core-shell nanowire structure.[23,31] Indeed, it would be impossible for the very thin core-shell nanowires studied by Shi *et al.* and Wu *et al.* to form the whispering-gallery cavity modes.

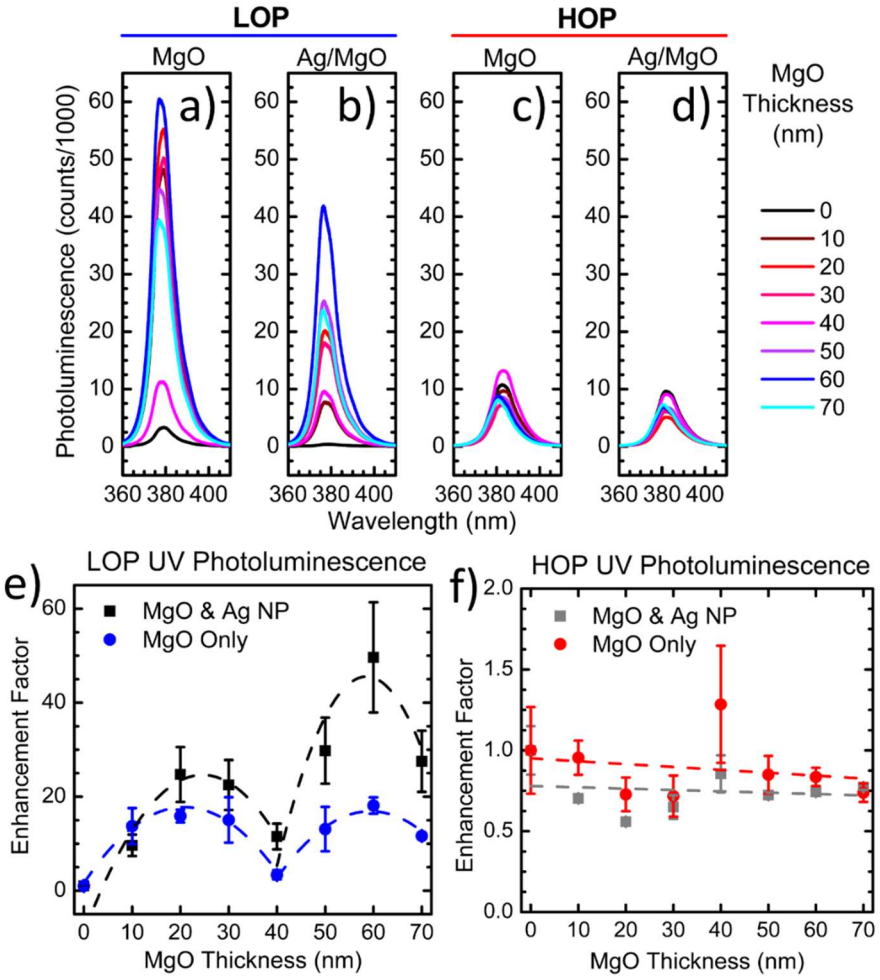

Figure 5.2: Band-edge photoluminescence (PL) of the MgO coated LOP nanowires, without (a) and with (b) an Ag nanoparticle (NP) coating. Band-edge PL of the MgO coated HOP nanowires, without (c) and with (d) an Ag NP coating. e) Normalized enhancement factor of the band-edge PL of the LOP nanowires as the MgO thickness increases, with (black) and without (blue) the Ag NPs. Maxima at 20 nm and 60 nm MgO thickness, dotted lines are quadratic fits to each peak. f) Normalized enhancement factor of the band-edge PL of the HOP nanowires as the MgO thickness increases, with (grey) and without (red) the Ag NPs. Data hover at unity with no enhanced peaks, dotted line is a linear fit to the data.

For both ZnO growth protocols, the band-edge PL spectrum at each MgO thickness was integrated from 360 nm – 420 nm and normalized to the bare nanowire PL, thus generating enhancement factors. The PL spectra and their enhancement factors highlight significant differences between the LOP and HOP nanowires, as seen in Figure 5.2.a,c,e,f. The LOP nanowires show bimodal maxima with enhancement peaks at 20 nm and 60 nm MgO thickness (Figure 5.2.e, blue), indicating the formation of two optical cavity modes. The HOP nanowires, on the other hand, exhibited a band-edge PL enhancement near unity for all MgO thicknesses (Figure 5.2.f, red), thus surprisingly showing no evidence that optical cavity modes are supported in these structures, despite having an ideal ZnO core diameter.

5.2.3 Ag Nanoparticle Coated Nanowires

After characterizing the ZnO/MgO core-shell nanowire photoluminescence, both the LOP and HOP CS nanowires were overcoated with silver nanoparticles in order to study PL enhancement *via* plasmon-exciton coupling, as in Chapter 3.2. The Ag-coated LOP nanowires did show additional enhancement over the bare core-shell nanowires, while there was no PL enhancement in the HOP nanowires coated with Ag nanoparticles (Figure 5.2.b,d,e,f). As the silver nanoparticle coating is not the main focus of this paper, further discussion of Ag plasmons coupling to ZnO excitons is reserved for the end of this chapter in Section 5.5. The lack of enhanced UV PL in the Ag-coated HOP nanowires is further evidence of the importance of optical cavity modes.

5.3 Microstructural Analysis

5.3.1 Transmission Electron Microscopy

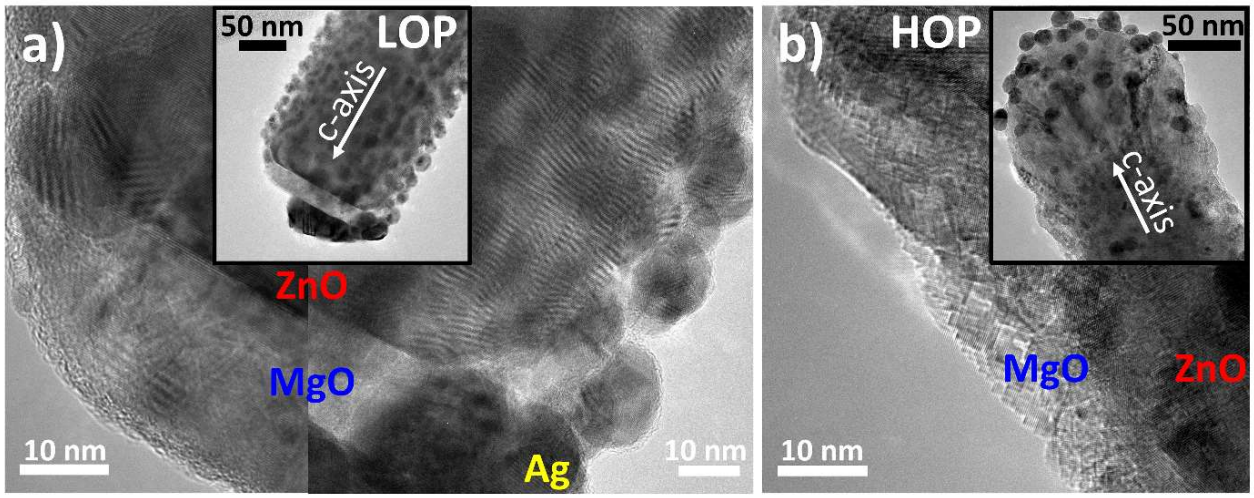

Figure 5.3: Transmission electron micrographs of an Ag- and MgO- coated ZnO a) LOP and b) HOP nanowire. Insets in a) and b) show the zoomed out ZnO/MgO core-shell nanowire. a) The two panel image of the end facet and sidewall of the LOP nanowire shows a smoother ZnO/MgO interface and a smoother outer MgO surface continuing along the nanowire sidewall. b) The HOP nanowire shows an overall rougher surface with many cubic, randomly oriented MgO crystals.

To determine why the photoluminescence spectra of the HOP nanowires do not exhibit the same cavity-mode enhanced PL as the LOP nanowires, the crystal structures of both nanowire growth protocols were studied by transmission electron microscopy (TEM) after all PL studies were completed. For all TEM (Tecnai Osiris, 200 keV), each sample was prepared by pressing a lacy carbon TEM grid directly onto the sample, resulting in a transfer of nanowires from the substrate to the grid. In Figure 5.3, the LOP nanowires showed a smooth MgO coating and a nearly epitaxial interface with the MgO on the ZnO $(1\bar{1}00)$ *m*-plane sidewall and the (0001) *c*-plane top facet. Conversely, the HOP nanowires had a rough, jagged surface along the ZnO *m*-plane sidewall and *c*-plane top facet, with multiple cubic MgO grain orientations evident. A coating of Ag nanoparticles is visible on both samples in the insets of Figure 5.3 (fabrication

of Ag nanoparticles is discussed in Section 2.1.2). Energy dispersive x-ray spectroscopy, Figure 2.9, shows that the MgO shell is of uniform thickness along the length of the ZnO nanowires.

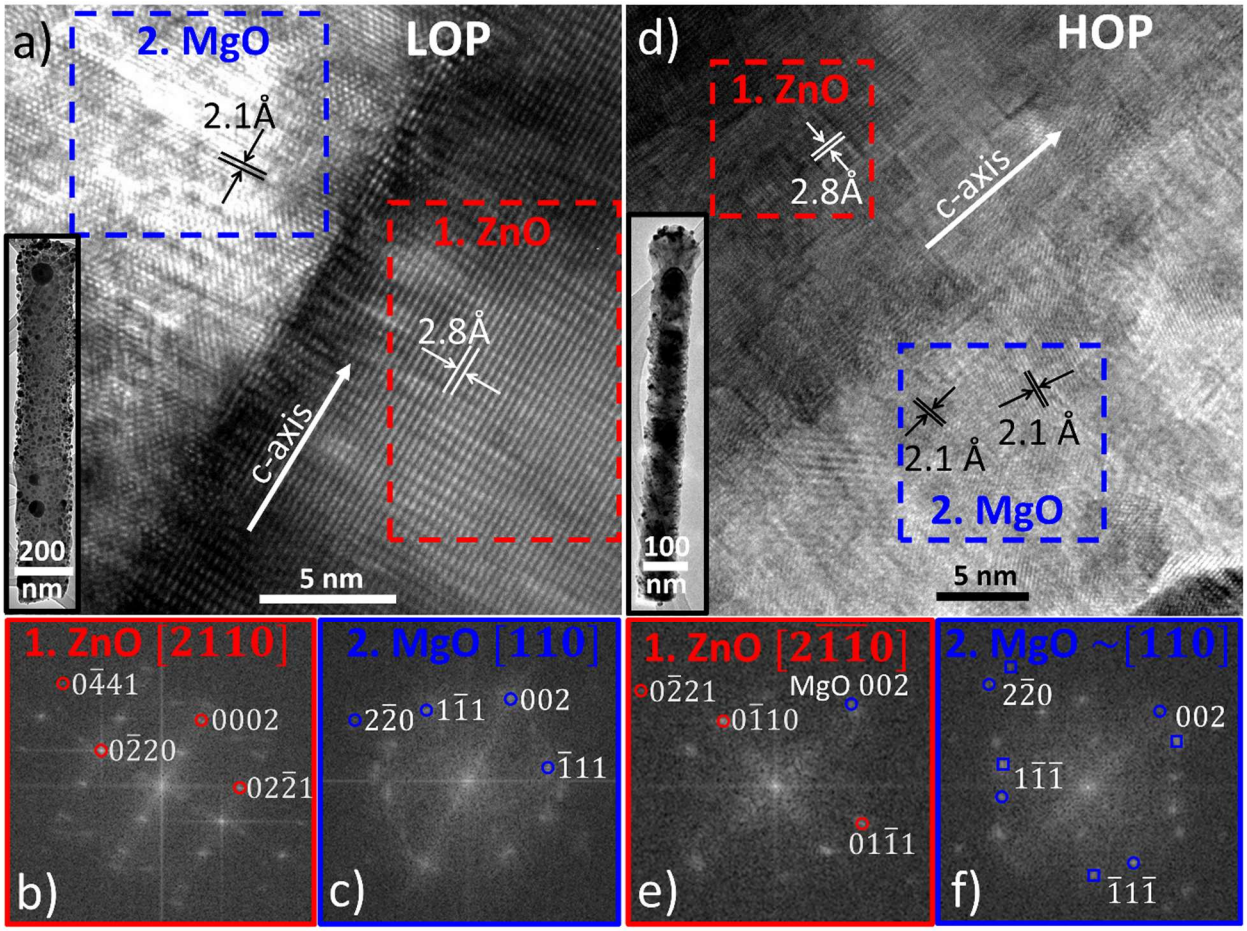

Figure 5.4: Transmission electron micrographs of the ZnO/MgO interface region of a LOP and HOP NW. a) LOP NW: ZnO/MgO interface (inset of the full wire) with highlighted regions - red: the 2.8 Å lattice spacing in the [0002] direction of wurtzite ZnO, blue: the 2.1 Å lattice spacing in the [002] direction of rock-salt MgO. Diffractograms of the highlighted regions - b) red: the $[2\bar{1}\bar{1}0]$ direction of wurtzite ZnO, c) blue: the [110] direction of rock-salt MgO. Lattice planes of the single crystal ZnO wurtzite (red circles) and large-grain epitaxial MgO rock-salt (blue circles) are identified. d) HOP NW: ZnO/MgO interface (inset of the full wire), with highlighted regions - red: the 2.8 Å lattice spacing in the [0002] direction of wurtzite ZnO, blue: the 2.1 Å lattice spacing in two [002] directions of rock-salt MgO. Diffractograms of the highlighted regions - e) red: the $[2\bar{1}\bar{1}0]$ direction of wurtzite ZnO and f) blue: approximately the [110] direction of rock-salt MgO. Lattice planes of the single crystal ZnO wurtzite (red circles) and two orientations of the small-grain epitaxial MgO rock-salt (blue circles and squares) are identified. In both samples, as small superlattice region is observed between the ZnO and MgO.

The boundary region of the ZnO nanowire $(1\bar{1}00)$ *m*-plane with the MgO coating is shown in Figure 5.4 for both samples. In Figure 5.4.a, of a LOP nanowire, uniform lattice fringes are visible in both the ZnO nanowire and the MgO shell near the boundary, with the diffractograms in Figure 5.4.b-c showing high crystallinity of both the ZnO and MgO. Diffractogram spots for wurtzite ZnO and rock-salt MgO are present, highlighted by red and blue circles respectively. The 2.1 Å (002) plane of rock-salt MgO is found to be parallel to the 2.6 Å (0002) plane and perpendicular to the 2.8 Å (100) plane of the wurtzite ZnO. This feature indicates that the MgO grown on LOP ZnO formed large-grain epitaxial crystals. The JCPDS numbers for assigning the ZnO and MgO crystal orientations were 36-1451 and 45-0946.

However, large-grain epitaxial rock-salt MgO growth did not occur in HOP nanowires (Figure 5.4.d-f). Figure 5.4.d and the associated diffractograms in Figure 5.4.e-f show that the ZnO/MgO boundary region is also encased in rock-salt MgO; however, the 2.1 Å (002) planes of the rock-salt MgO have multiple orientations, with only some (002) rock-salt planes parallel to the 2.6 Å (0002) planes of the ZnO. Here blue circles and squares represent two distinct crystal orientations of the MgO, approximately 20° apart in the (110) lattice plane. These results indicate that HOP nanowires favor growth of small-grain epitaxial rock-salt MgO crystals on ZnO, in contrast to the large-grain epitaxial MgO crystals observed on the LOP samples.

5.3.2 Defect Types

The difference in the size of MgO grains on the LOP and HOP nanowires suggests that defects on $(1\bar{1}00)$ *m*-plane surface of the ZnO might play a key role. Indeed, PL of bare LOP and HOP nanowires indicates that there is a different density of *m*-plane surface defects on the

two samples, because the HOP samples had double the band-edge to visible emission ratio of the LOP samples (Figure 5.1.a.), implying higher crystallinity and substantially fewer surface defects in those nanowires. Additionally, Table 2.2 in Chapter 2 shows that the LOP protocol used higher temperature and lower oxygen pressure than the HOP protocol. Higher temperatures lead to increased growth rates,[18] thus to a potential increase in step-edge defects, and the lower oxygen pressure leads to oxygen and zinc point defects.[201] In ZnO, oxygen (310 keV) has a lower displacement threshold than zinc (900 keV), making it more probable that oxygen vacancies would occur rather than zinc vacancies.[202] Therefore, it is reasonable to assume that the LOP samples have more oxygen vacancies on the nanowire surface. The oxygen vacancies could therefore result in *m*-plane surface reconstructions that favor large-grain rock-salt MgO growth. Alternatively, the LOP samples could have increased step-edge defects resulting from the higher growth rate, which in turn could also nucleate the growth of large-grain epitaxial rock-salt MgO on LOP nanowires.

The small-grain MgO crystallites on the HOP nanowires evidently nucleated from fewer surface defects than present in the LOP nanowires. If the ZnO nanowire *m*-plane surface were defect-free, the first few deposited MgO layers would conform to the wurtzite ZnO interface. As the MgO layer grows thicker, it would undergo a structural phase transition to the stable rock-salt phase, since the bulk wurtzite MgO is unstable.[203] Such crystallographic transitions can happen at multiple thicknesses and positions during MgO growth and would result in rock-salt MgO grains with multiple orientations – as shown in the HOP electron micrographs (Figure 5.4). Putting these scenarios together, surprisingly, defects on the ZnO $(1\bar{1}00)$ *m*-plane surface played the critical role in the formation of the smoother MgO shell on LOP nanowires, consistent with density-functional calculations.

5.3.3 Density Functional Calculations

First-principles density functional calculations of the MgO growth on *m*-plane ZnO were carried out using the Perdew–Burke–Ernzerhof (PBE) functional,[204] projector augmented wave (PAW) potentials[205,206] and a plane-wave basis with cutoff energy equal to 400 eV, as implemented in the VASP (Vienna *ab initio* simulation package) code.[207] The structural relaxations were converged to 10^{-3} eV for the total energy difference between two ionic steps. For bulk ZnO, lattice constants $a = 3.260$ Å and $c = 5.218$ Å were obtained, which agree with experimental values of $a = 3.249$ Å and $c = 5.205$ Å.[208] For MgO, the calculated $a = 4.201$ Å agrees with the experimental value of $a = 4.216$ Å.[208] These lattice constants were used to construct a 4x3 supercell of the $(1\bar{1}00)$ *m*-plane surface of the ZnO. A single Γ point (0, 0, 0) was used for Brillouin zone sampling.

Density-functional theory calculations allowed us to explore both point defects (oxygen vacancies) and step-edge defect types on the $(1\bar{1}00)$ *m*-plane surface of ZnO. To investigate the possibility that the $(1\bar{1}00)$ *m*-plane surface would undergo reconstruction due to oxygen vacancies, oxygen atoms were removed from the surface of ZnO and the structure was relaxed. Molecular dynamics (MD) simulations were then run to introduce thermal vibrations about equilibrium positions in the system. Finally, the lattice was relaxed again to be sure that a stable configuration had been found. Throughout this process, the $(1\bar{1}00)$ *m*-plane surface of the wurtzite ZnO showed no surface reconstruction even with half the surface oxygen atoms removed.[32] Therefore, the oxygen vacancies are not responsible for large-grain epitaxial rock-salt MgO growth on LOP nanowires.

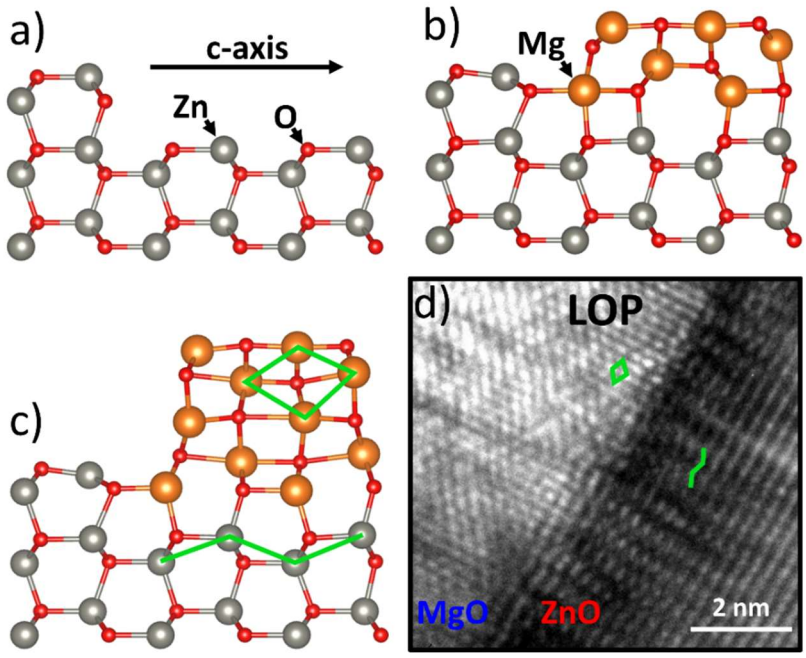

Figure 5.5: Comparison with structure calculations (a-c) and zoom in of LOP ZnO/MgO interface (d). a) The simulated step defect on the ZnO *m*-plane along the *c*-axis (grey Zn and red O atoms). b) The simulated two layer rock-salt MgO growth after structural relaxation (yellow Mg atoms). c) The simulated five layer rock-salt MgO growth after structural relaxation with the diamond structure of rock-salt and the saw tooth structure of wurtzite identified in green. d) Zoom of the interface region of the transmission electron micrograph in Figure 5.4.a of a LOP nanowire, with the diamond structure of the MgO and the sawtooth structure of the ZnO identified with green lines, matching the orientations found in the DFT.

Subsequently, step-edge defects on the ZnO $(1\bar{1}00)$ *m*-plane surface were introduced along the *c*-axis direction, as shown in Figure 5.5.a. Then Mg and O atoms were attached to the step edge, the structure was relaxed, MD simulations were executed, and the final relaxed structure was determined to be a stable configuration, as in Figure 5.5.b. The Mg atoms that nucleated at the step edge showed a tendency to bond at 90˚ – typical of the rock-salt structure. After adding additional Mg and O atoms to the structure at the nucleation site and relaxing the structure, a stable epitaxial layer of MgO was obtained that clearly shows the rock-salt lattice. In Figure 5.5.c., the atoms were aligned to match the orientation of the atoms shown in the TEM of a LOP nanowire from Figure 5.4.a. Figures 5.5.c-d highlight, in green, the diamond

configuration of the rock-salt MgO and the sawtooth configuration of the wurtzite ZnO, confirming that the DFT calculations replicate the observed MgO formation in the LOP nanowires.

Taken together, therefore, the DFT, TEM, and PL calculations and measurements point to the ZnO $(1\bar{1}00)$ *m*-plane surface step-edge defects as not only being correlated with, but also in fact as necessary for the large-grain epitaxial growth of rock-salt MgO on ZnO nanowires.

5.4 Mechanisms Preventing Optical Cavity Mode Photoluminescence Enhancement

5.4.1 Surface Roughness and Scattering

It is necessary to compare the surface roughness of bare ZnO nanowires and the MgO shell, first to confirm the presence of morphological defects experimentally, and second because roughness plays a critical role in optical scattering at the interface between ZnO core and MgO shell and between the MgO shell and air. For both the LOP and HOP growth protocols, the surface roughness of the ZnO *m*-plane and *c*-planes and the MgO top facet and sidewall surfaces was determined by analyzing TEM images with ImageJ, using the arithmetic average of absolute values, $R_a = \frac{1}{n}\sum_{i=1}^{n}|y_i|$, using the absolute value of the deviation y_i averaged over n surface positions. A standard deviation was determined by analyzing multiple images from samples prepared by each of the two nanowire protocols. To calculate the MgO sidewall roughness of the LOP nanowires, measurements from multiple sections of a single image were averaged to determine the standard deviation.

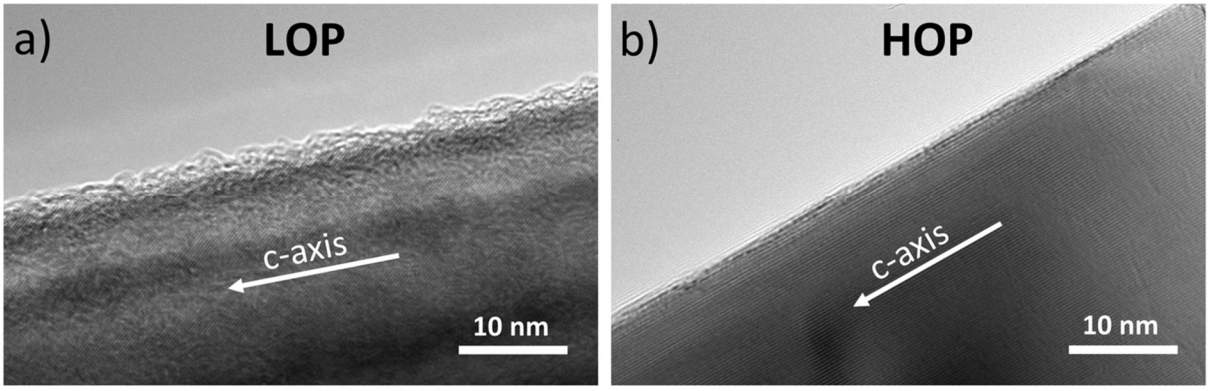

Figure 5.6: Transmission electron micrographs of bare ZnO nanowires in a) a LOP sample and b) a HOP sample. The LOP nanowire shows a rougher $(1\bar{1}00)$ *m*-plane ZnO surface than the HOP nanowire.

Table 5.2: Surface roughness of the bare ZnO nanowires and MgO coating, comparing surface roughness on the nanowire tops to the nanowire sides.

Surface Roughness [nm]	Material	LOP Nanowires	HOP Nanowires
TOP	ZnO	0.38 ± 0.13	0.34 ± 0.15
	MgO	0.29 ± 0.17	0.75 ± 0.20
SIDE	ZnO	0.15 ± 0.02	0.07 ± 0.01
	MgO	0.4 ± 0.1	1.69 ± 0.69

First, TEM analysis of the surface roughness of the $(1\bar{1}00)$ *m*-plane of the bare LOP and HOP ZnO nanowires (Figures 5.6 and 5.7, Table 5.2) shows that the $(1\bar{1}00)$ *m*-plane sidewalls of the LOP nanowires has twice the surface roughness of the HOP nanowires. Additionally, the surface roughness of the *c*-plane nanowire end facets, given in Table 5.2 and visualized in Figure 5.7, shows that the LOP and HOP nanowire end facets have similar roughness values. An increased number of surface defects, including step-edge defects, on the *m*-plane of the ZnO nanowires would lead to a rougher *m*-plane surface in the LOP nanowires. This increased

surface roughness provides the experimental evidence corroborating the DFT analysis, indicating an increase of *m*-plane step-edge defects is indeed likely to be found in the LOP nanowires.

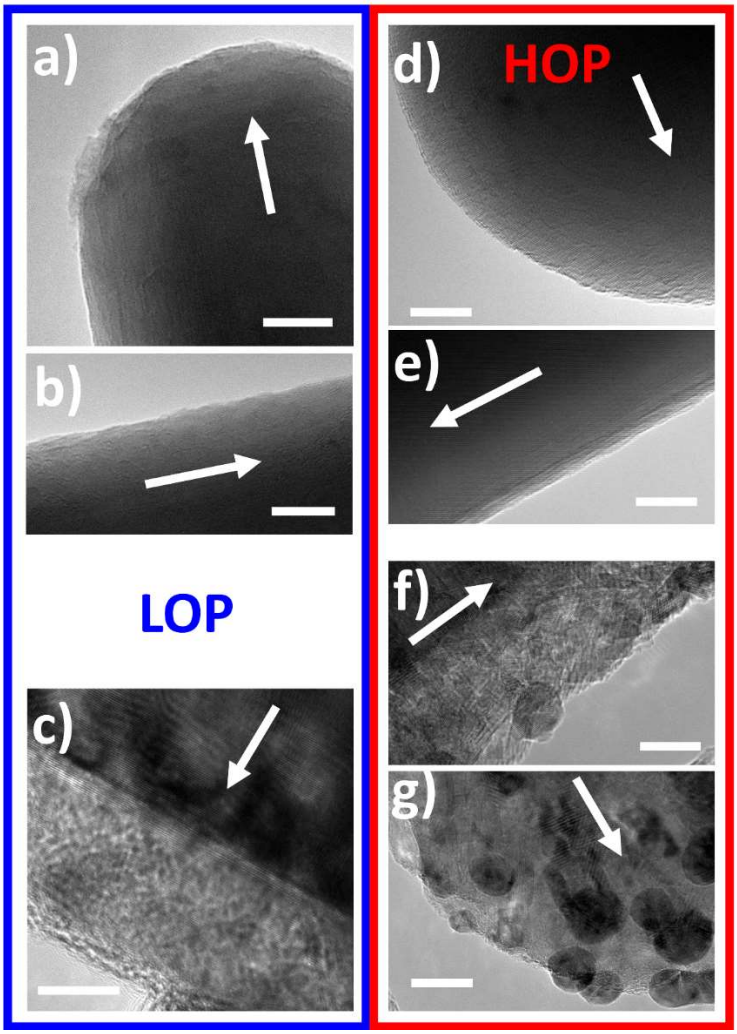

Figure 5.7. Transmission electron micrographs of the ZnO and MgO surface for the surface roughness study. a-c) LOP nanowire. d-g) HOP nanowire. Micrographs a,b,d,e) are of bare ZnO, while c,f, g) show Ag coated MgO/ZnO core-shell nanowires. All scale bars are 10 nm, and the arrows indicate the *c*-axis direction of the ZnO.

Second, the surface roughness of the MgO coatings of the LOP and HOP core-shell nanowires, tabulated in Table 5.2, determines the potential for scattering at the core-shell

nanowire interfaces. As expected from TEM images (Figures 5.3 and 5.8), the large-grain rock-salt MgO crystals on the LOP nanowires had a four-fold smoother sidewall surface and two-fold smoother end facet surface than the small-grain rock-salt MgO crystals on the HOP nanowires. In fact, deposition of the MgO coating increases the sidewall roughness of the LOP nanowires by less than a factor three, while the MgO coated HOP nanowires exhibit a ten-fold increase in sidewall surface roughness. Increased surface roughness, on the scale of nanometers, is known to increase light scattering in waveguides with diameters of order hundreds of nanometers, while scattering is much less important in waveguides with micron diameters.[209-212] Also, the HOP nanowires are 60 % longer than the LOP nanowires, thus increasing the opportunity for scattering of the UV emission. The longer HOP nanowires and the ten-fold increase in surface roughness experienced by the small-grain MgO coating leads to a large increase in scattering at the MgO/air and ZnO/MgO boundaries. This scattering inhibits propagation of optical cavity modes and thus reduces PL enhancement. However, the minimal increase in interface roughness, and thus in scattering, in the MgO coated LOP core-shell nanowires, supports the propagation of the ZnO band-edge emission along the nanowire, leading to the propagation of the optical cavity modes and enhanced PL in the smoother LOP core-shell nanowires.

5.4.2 Step-Index Confinement

While scattering is the primary cause of the lack of PL enhancement in the HOP ZnO/MgO core-shell nanowires (mitigating the propagation of the optical cavity modes), a possible secondary cause of the lack of PL enhancement could be a reduced density in the MgO coating. The refractive index of a material structure depends on the material density, with lower

density structure of a material having a lower refractive index than a higher density structure of that same material.[213] Single crystals have the highest density and thus the highest refractive indexes, with polycrystalline and smaller grain materials having lower refractive indexes, as has been shown with MgO.[214,215] The HOP nanowires grow smaller MgO nanocrystallites with multiple orientations, increasing the number of MgO grain boundaries, leading to a potentially reduced refractive index than in the larger-grain epitaxial MgO grown on the LOP nanowires.

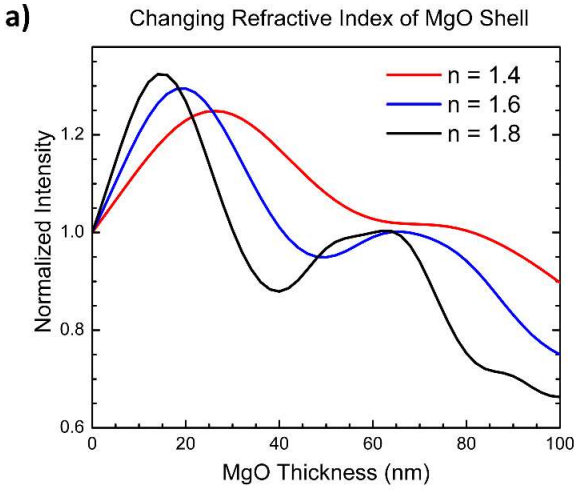

b) Gaussian fits to simulation peaks

Refractive Index	Peak 1			Peak 2		
	Position (nm)	FWHM (nm)	Intensity	Position (nm)	FWHM (nm)	Intensity
1.8	14.62	24.87	0.66	59.07	27.48	0.35
1.6	18.63	31.71	0.60	68.38	34.53	0.31
1.4	25.55	40.69	0.45	78.13	38.05	0.20

Figure 5.8: a) The normalized intensity (Equation 3.2) of ZnO/MgO core-shell nanowires as the refractive index of the MgO shell changes. The normalized intensity here is a linear combination of the 325 nm and 380 nm wavelengths, weighted at 33 % and 67 % respectively (as in main text). At wavelengths of 380 nm – 325 nm, MgO single crystals have a refractive index of 1.77-1.78 (used in the simulations for the main text) here approximated at 1.8. Here we also simulate n = 1.6 and n = 1.4 to demonstrate how the optical confinement changes if the MgO has a lower density. Grain boundaries and smaller grain films have a lower density and thus lower refractive index. b) The Gaussian fit results to the normalized intensities for each refractive index of MgO. The larger the refractive index of the MgO shell, the sharper and more confined to a specific MgO thickness the cavity mode becomes. The Gaussian fits show this, with the intensity of each peak increasing with increased refractive index, and conversely the full width half maximum (FWHM) of each peak decreasing with increased refractive index. This indicates a stronger mode confinement at a specific MgO thickness when the MgO has a larger refractive index.

In order to study how the refractive index of the MgO affected the confinement of the optical cavity modes, finite-element analysis (FEA) simulations were conducted of a ZnO/MgO core-shell nanowire cross section. The set-up for these simulations is the same as that used in Chapter 3, Section 3.2.4. The ZnO core was held at 90 nm, the MgO shell was varied from 2 – 100 nm in 2 nm increments. Simulations were run for both the 325 nm excitation wavelength and the 380 nm ZnO band-edge emission. Here, three of these simulation sets were run, each with a different MgO refractive index.

The refractive index of single crystal MgO at wavelengths of 380 nm – 325 nm is 1.77 – 1.78; small grain and polycrystalline MgO have refractive indexes as low as 1.6 in the visible wavelength region.[214,215] Thus we have compared simulations with refractive indexes of 1.8 (rounding up the refractive index of 1.77-1.78) to those with refractive indices of 1.6 and 1.4 – the latter case where there would be large air voids in a very disordered, nanocrystalline MgO. Results are presented in Figure 5.8, along the parameters of the Gaussians fits to the simulated normalized intensities (normalized intensity in Equation 3.2). When the MgO has a refractive index of 1.8, the optical cavity modes are the most confined to a specific MgO thickness and has the highest peaks in normalized intensity. At a refractive index of 1.6, the normalized intensity of both the lower-order and higher-order cavity modes is reduced, as seen in Figure 5.8.b. The normalized intensity at a refractive index of 1.6 is broadened over more MgO thicknesses, with a larger full-width half-maximum of the Gaussian fit for both the lower-order and higher-order modes. With a refractive index of 1.4, the modes broaden and intensity is reduced even further, becoming much less confined spatially. While a reduced MgO refractive index is not the only reason for the lack of optical cavity mode enhancement in the band-edge PL of the HOP samples, it is a contributing factor. Decreased confinement of the optical cavity modes would

reduce the localized intensity of the modes and thus the number of excitons created in the core-shell nanowire cavities, leading to lower photoluminescence yield than when the optical cavity modes are highly confined.

5.4.3 Electronic Structure

A third potential mechanism reducing PL enhancement in the ZnO/MgO core-shell HOP nanowires is changes in defect density that affect the electronic structure at the ZnO/MgO boundary. The type-I band-alignment of the ZnO/MgO core-shell nanowire leads to reduced band-bending at the ZnO interface, as proposed by Shi *et al*,[200] and can confine the excitons to the ZnO core, shown by Meng, *et al*.[199] Here, it is possible that the small-grain HOP MgO may not quench surface dangling bonds at the ZnO/MgO interface as efficiently as the large-grain LOP MgO.

The band-bending at the ZnO *m*-plane surface occurs as is shown in Figure 5.9.[200] In the bare ZnO nanowires, the surface dangling bonds and adsorbates may act as acceptors, trapping the free conduction band electrons,[216] thus creating the depletion layer and subsequent band bending in Figure 5.9.a. This separates the electron and hole pairs, creating a lower probability of recombination at the ZnO surface. When the MgO coats the surface, it quenches the ZnO surface defects,[119,199] which reduces the band bending (Figure 5.9.b) and allows the electron and hole pairs to be in closer proximity, increasing the probability of the near-band edge exciton radiative recombination.[200]

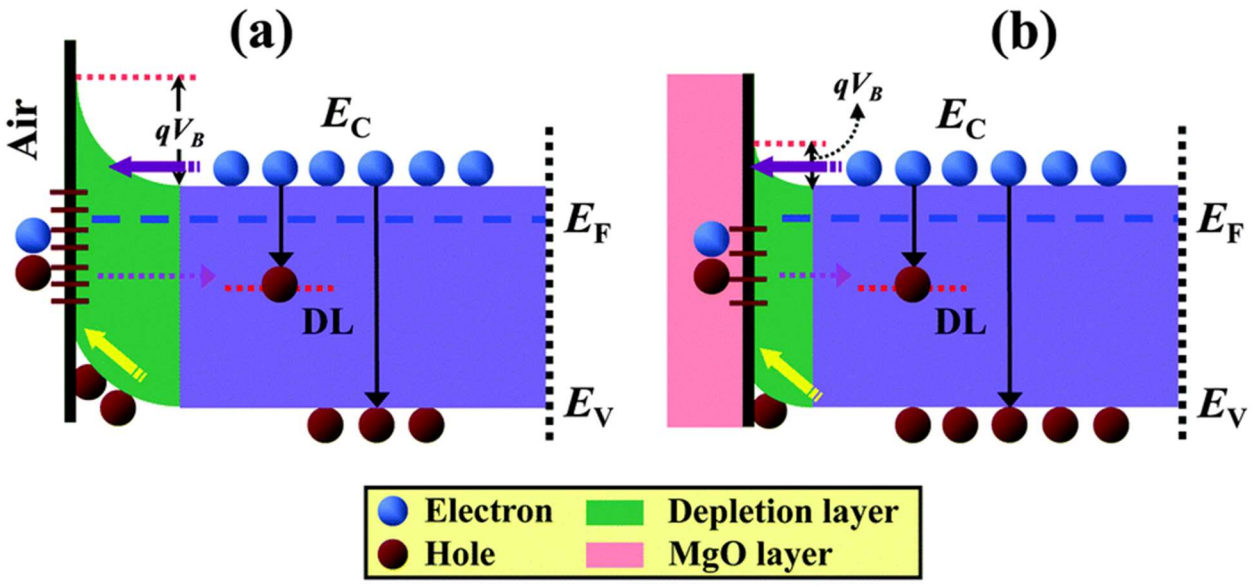

Figure 5.9: Schematic band diagrams of (a) bare and (b) MgO-coated ZnO nanowires. (c) Energy band diagram of a ZnO/MgO heterojunction at thermal equilibrium.[200] (d) Schematic diagram of a ZnO/MgO coaxial nanowire and a proposed quantum-well-like structure for the explanation of enhancement of carrier radiation recombination.[200]

The HOP MgO and LOP MgO have different grain sizes, and this could affect the quenching of the ZnO surface defects. The small grain HOP MgO has more grain boundaries, and thus it is more likely that is does not quench ZnO surface defects as effectively. Less surface defect quenching in the HOP nanowires would create a larger depletion region at the ZnO/MgO boundary, increase the boundary potential,[217] reduce interaction between MgO holes and ZnO electrons, and thus reduce the concentration of excitons in the ZnO core.[200] This, in turn, could lead to a reduction of the photoluminescence enhancement in the MgO coated HOP nanowires.

5.5 Plasmon-Exciton Coupling

When the LOP and HOP core-shell nanowires were overcoated with plasmonic Ag nanoparticles, additional enhancement was seen the LOP nanowires, as shown in Figure 5.2.b and Figure 5.2.e. That additional enhancement from the Ag nanoparticle coating was not observed in the HOP nanowires, shown in Figure 5.2.d,f. Here we recap the mechanisms at play causing the additional enhancement in the LOP nanowires and analyze the converse lack of additional enhancement in the HOP nanowires.

Chapter 2, Section 2.1.3 discusses the size and localized surface-plasmon resonance (LSPR) of the Ag nanoparticles on both samples. Figure 2.8 shows the extinction spectra; the rapid rise in extinction at 380 nm is due to the band-edge absorption of the ZnO. At the risk of oversimplification, we assume that the plasmon resonance occurs at the wavelength where the difference between Ag-coated and uncoated nanowires is a maximum. On the LOP nanowires, the maximum change in extinction with the addition of the Ag nanoparticles was 10^{-3}, as noted in Table 2.4, occurs at a wavelength of 375 nm. On the HOP nanowires, the maximum change in extinction occurred at 405 nm, with a factor of ten smaller change in extinction of 10^{-4} (Table 2.4). The nanoparticles on the LOP nanowires have a much stronger absorption than the nanoparticles on the HOP nanowires. However, the plasmon resonance wavelength of the Ag nanoparticles on the HOP nanowires was much closer to the ZnO band-edge emission wavelength, due possibly to the blue shifting of the resonance with smaller particle size as well as the likelihood that the low nominal deposition thickness of Ag on the HOP nanowires leads to the formation of a large number of nanoparticles too small to be easily seen with the resolution employed in the STEM studies. Those smaller nanoparticles would have a strongly blue-shifted resonance due to quantum-size effects.

For the LOP nanowires, Ag was deposited to a 10 nm nominal thickness, compared to 3 nm nominal thickness on the HOP nanowires. The nanoparticles grow as individual nucleation sites accrete Ag atoms by Ostwald ripening, leading to differences in nanoparticle size: while the diameters of the nanoparticles are relatively close in magnitude, the fact that nanoparticle absorption scales with volume leads to a factor of 2.7 increased absorption per nanoparticle between the LOP and HOP samples. Moreover, the percent coverage of nanoparticles on the sidewalls is significantly different between the LOP and HOP samples: The Ag nanoparticle coverage approaches 70 % coverage on the LOP nanowires compared to 6 % coverage on the HOP nanowires, as shown in Table 2.4. Thus the combined differences in nanoparticle coverage and size implies a factor 30 difference in the plasmon resonance extinction between the two samples.

When Ag nanoparticles are deposited on the LOP nanowires, the total observed enhancement reaches 25-fold and 50-fold at 20 nm and 60 nm MgO thickness, respectively, shown as the black data points in Figure 5.2.e, and discussed in detail in Chapter 3, Section 3.4. This enhancement is due to the Purcell mechanism, increasing the radiative recombination rate of the ZnO excitons by coupling to the nearly resonant Ag plasmons on the sidewalls of the nanowires, with their large density of electronic states .[28,31] The differential enhancement of the Fabry-Perot and whispering-gallery modes is due to the increased interaction of the whispering-gallery modes with the Ag nanoparticles on the nanowire sidewalls, as discussed in Section 3.3, and shown in Figure 3.5. The increased interaction of the plasmons with the whispering gallery modes yields double the PL enhancement at 60 nm MgO thickness, as discussed in Mayo, *et al*.[31]

In the Ag-nanoparticle coated HOP nanowires, one would expect the same Purcell enhancement of the photoluminescence emission to occur, as the nanoparticle size on the sides of

the nanowires is very similar between the HOP and LOP samples. However, no PL enhancement is seen, as shown in the gray data points in Figure 5.2.f., for two possible reasons: The first is that the order of magnitude smaller coverage of the Ag NPs on the ZnO nanowires leads to a significantly reduced interaction probability between the ZnO excitons and the Ag plasmons. This would reduce the overall enhancement, as fewer ZnO excitons would be coupled to the Ag plasmons. The second is that the scattering in the MgO shell, which inhibits waveguiding of the optical cavity modes in the HOP sample, also prevents enhancement of the 380 nm band-edge emission from plasmon-exciton coupling. There is not sufficient evidence in the present experiments to conclude which of these mechanisms most strongly inhibited enhanced PL due to plasmon-exciton coupling in the Ag-coated HOP nanowires, or to conclude that no such enhancement is possible in the HOP nanowires.

5.6 Conclusions

The combination of experiments, calculations, and simulations presented here shows that the ZnO $(1\bar{1}00)$ *m*-plane surface, the structure of the MgO coating at the nanowire boundary, and the photoluminescence enhancement of ZnO/MgO core-shell nanowires all depend critically on the processing locus in the ZnO phase diagram. During ZnO nanowire growth, higher partial oxygen pressures yield smoother ZnO nanowires with increased band-edge photoluminescence, but fewer ZnO *m*-plane step-edge defects. Zinc oxide nanowires with a smooth sidewall inhibits the formation of large-grain epitaxial MgO. The four-fold rougher small-grain MgO shell yielded no significant PL enhancement as the MgO thickness increased. On the other hand, a ZnO nanowire *m*-plane surface twice as rough, grown at lower partial oxygen pressure, formed

large-grain epitaxial MgO, which turns out to be a requirement for the observed, fifteen-fold optical cavity mode enhancement of the ZnO band-edge PL. This is due to decreased scattering from the large-grain epitaxial MgO coating, increased optical confinement of the cavity modes, and more efficient passivation of surface defects. These results point the way to reliable design and fabrication of optical cavity enhanced UV nanolasers, on chip-waveguides, and nanowire scintillators.

5.7 Acknowledgements

This chapter brings together a very large collaboration on ZnO core-shell nanowires. For the collaborative work on the LOP nanowires, I again sincerely thank Prof. Daniel Mayo and Prof. Richard Mu. For work on the HOP nanowires, I thank my REU student, Zhineng Li, who assisted me for the summer I was analyzing the results from the sample presented in this chapter. For the TEM imaging and microscopy analysis, as well as for insight on the reviewer response, I thank Dr. James McBride. For the DFT calculations, I thank a collaboration with Prof. Sokrates Pantelides, which included Prof. Xiao Shen and his REU student, Dominic Critchlow. This paper on the photoluminescence of ZnO core-shell nanowires could not have come together without the combined analysis of the PL, TEM, and DFT work. Additionally, I thank Xiao for writing the DFT section of this paper. Finally, I thank Prof. Richard Haglund for the many versions of this paper he helped me edit and refine.

CHAPTER 6

EXCTION-PHONON COUPLING IN ZNO NANOSTRUCTURES

This chapter is a study of the near-band edge emission between three ZnO nanostructures, that of the original, randomly oriented nanowires grown through the vapor-solid protocol, the vertically-oriented "carpet" nanowires grown through the hydrothermal protocol, and finally, the novel "nanopopcorn" grown on a GaN substrate through a vapor-solid protocol. The temperature dependence of the near-band-edge photoluminescence elucidates the broadening of the UV emission due to exciton-phonon coupling and defect bound excitons, discussing the dependence of the coupling strength on the nanostructure morphology. This work is in preparation for submission.

- **C.E. Marvinney**, A. Ueda, S. Avanesyan, J.R. McBride, E. Hindsman-Curry, H.Y. Xu, R.R. Mu, R.F. Haglund, *Exciton-Phonon Coupling in Zinc Oxide Nanowires and Nanopopcorn,* in preparation.

6.1 Background: Temperature Dependence and Exciton-Phonon Coupling

Temperature-dependent photoluminescence (TD-PL) studies can be used to characterize the crystalline quality of ZnO nanostructures.[1] Some ZnO nanostructures can exhibit a high integrated band-edge to visible emission ratio at room temperature, and a low band-edge to visible emission ratio at low temperature, as the emission due to defects in the sample can become more dominant at lower temperatures.[1,8,218-221]

The room-temperature near-band-edge emission of ZnO is due to the recombination of free excitons, typically the A-exciton emission, and this exciton emission is broadened due to scattering with phonon modes in the sample.[1,7,20,222] The interaction of excitons with phonon modes can indicate variations in sample morphology, with samples with higher surface-defect densities having increased exciton-LO phonon coupling, and samples with higher exciton-acoustic phonon coupling having fewer bulk defects.[1,7,8,20,223,224] In low-temperature PL, the band-edge emission blue shifts due to exciton-phonon interaction, and depending on the defect density, bound exciton and phonon replicas of free and bound exciton emissions become visible, and even dominate the emission.[1,7,8,20,223,224] At the lowest temperatures, the near-band-edge emission is dominated by the bound exciton complexes in the ZnO sample, originating from recombination of excitons trapped at ZnO defects such as neutral and ionized donors and acceptors, and interstitial atoms such as N, Li, and Ga.[1,7]

Temperature-dependent studies of ZnO nanowires[223] have been used to show how differences in growth technique, and thus differences in defect density, lead to variations in the band-edge PL due to increased phonon replicas in samples with increased surface defects. Here, over time, the "old," vapor-solid method and "new," hydrothermal method have been developed for growing ZnO nanowires. Other structures, prominently the novel nanopopcorn, have arisen from experimenting with these growth techniques. Studies of TD-PL and Raman spectroscopy are executed in order determine the types of defects present in ZnO nanowires and nanopopcorn growth through both the vapor-solid and hydrothermal growth techniques. Which of these growth techniques leads to the highest crystalline quality, highest UV emission nanostructures, and will lead the way to efficient UV emission applications from nanolasing to sensing?

6.2 Temperature-Dependence of the UV Photoluminescence of ZnO Nanostructures

6.2.1 Zinc Oxide Nanostructures

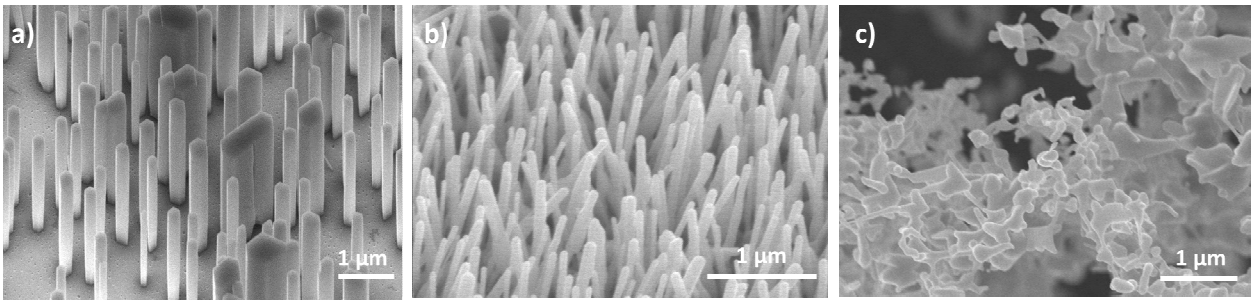

Figure 6.1: Scanning electron micrographs of the ZnO a) vertical nanowires, b) random nanowires, and c) nanopopcorn.

For this study, three distinctly different nanostructures were compared in order to learn how the nanostructures from the hydrothermal growth method and the nanostructures from the vapor-solid growth method compare, in terms of crystallinity and defect density. The first nanostructure is the "new" vertically oriented "carpet" nanowires (referred to as vertical nanowires for this chapter), shown in Figure 6.1.a grown on a *c*-axis p-GaN on *c*-sapphire substrate. The growth parameters for the vertical nanowires are discussed in Chapter 2.2.1. The second nanostructure is the "old" vapor-solid grown, randomly oriented nanowires (referred to as random nanowires for this chapter), shown in Figure 6.1.b grown on a ZnO seed layer on a fused silica substrate. The growth parameters for the random nanowires used for this study are given in Table 2.1, from Chapter 2.1.1. These random nanowires were grown during the vapor-solid nanowire parameter sweep, and thus the conditions these random nanowires were grown under are half-way between those of the LOP nanowires and the HOP nanowires. The third nanostructure for this study is the novel ZnO "nanopopcorn" (referred to as nanopopcorn for this

chapter), shown in Figure 6.1.c grown on an intrinsic *c*-axis GaN on *c*-sapphire substrate. The nanopopcorn has a much higher surface-area-to-volume ratio than the two nanowire samples, with the hydrothermal nanowires having the lowest surface-area-to-volume ratio.

In Chapter 2, x-ray diffraction measurements (XRD) and transmission electron microscopy (TEM) of each type of nanostructure identified the growth directions of the vertical nanowires, random nanowires, and nanopopcorn. The vertical nanowires grow uniformly along the *c*-axis orientation, as in the TEM in Figure 2.14. They are all oriented in the same direction, as in the XRD in Figure 2.15 and the SEM in Figure 6.1.a, indicating epitaxial growth off of the p-GaN substrate. The random nanowires also grow along the *c*-axis orientation (TEM in Figure 2.4), however, they are oriented in many directions, as determined from the XRD (Figure 2.5) and the SEM in Figure 6.1.b. The random orientation of their growth directions is due to the random orientation of the ZnO seed layer that they grow off of. Finally, while the nanopopcorn are crystalline, indicated from both their TEM (Figure 2.12) and XRD (Figure 2.11), their orientation does not appear to be preferential to the substrate orientation or to the ZnO grains they are neighboring, as the nanopopcorn crystals grow in many directions and orientations.

6.2.2 Temperature-Dependent Photoluminescence Methods

For the TD-PL measurements, each sample was mounted in a nitrogen-cooled cryostat (MMR Technologies, Inc, R2300-20). The temperature was varied with a software package from MMR (Version 2.0) and the K-20 programmable temperature controller. Measurements were taken at 15 temperatures ranging from 80 – 300 K. The 325 nm spectral line of a HeCd laser (Kimmon, 1K series) was the excitation source. The measured power at the sample is approximately 6.0 mW, with slight variations from one day to the next due to lack of air

conditioning in the optics lab, focused onto the sample with a 15X UV objective lens. A spectrometer (HORIBA Jobin Yvon LabRAM 800HR) was used with a - 40 °C thermoelectrically cooled CCD camera as the detector. Due to saturation of the detector at low temperature, a D0.6 neutral density filter was used for the vertical nanowire and nanopopcorn measurements (but not for the random nanowire measurements). Each PL spectrum was measured from 340 – 650 nm for the random nanowires and nanopopcorn, and from 340 – 600 nm for the vertical nanowires, due to lack of defect emission in the vertical nanowires. All PL measurements used an 1800/mm diffraction grating and were acquired using the LabSpec Version 5.78.24 software that averaged four measurements with an integration time of 0.2 s.

6.2.3 Visible 'Defect' Emission

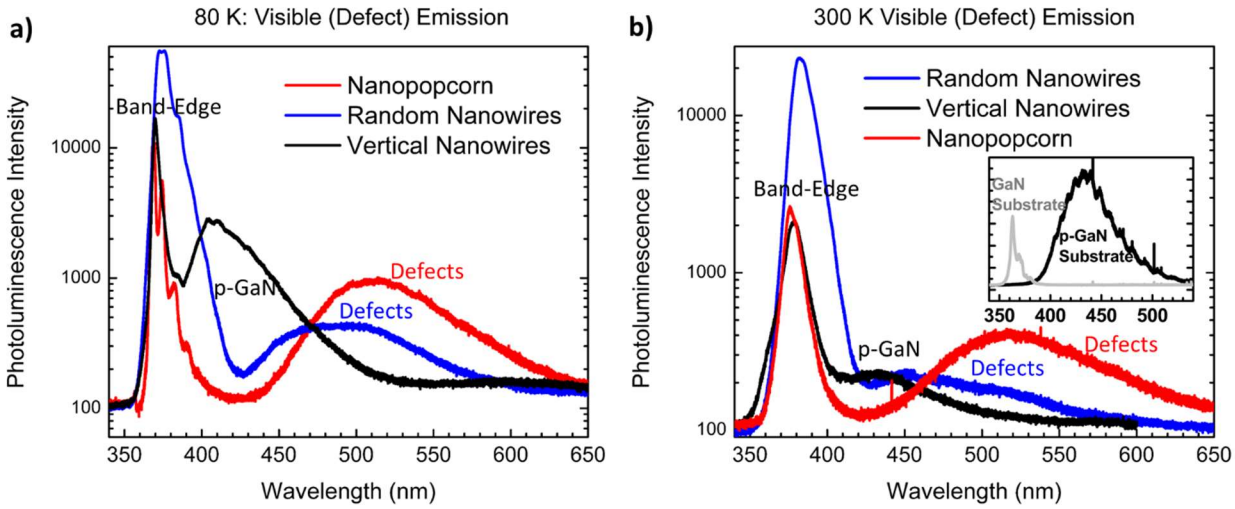

Figure 6.2: The photoluminescence spectra (plotted on a logarithmic scale) of all three samples at a) 80 K and b) 300 K, with inset of substrate emission for p-GaN (vertical nanowires) and GaN (nanopopcorn). The peaks associated with the UV band-edge emission, p-GaN substrate emission (vertical nanowires), and visible defect emission (random nanowires and nanopopcorn) are identified. No GaN substrate emission is observed in the nanopopcorn due to the much stronger ZnO UV emission. A D0.6 filter was used to collect the vertical nanowire and nanopopcorn TD-PL, while no filter was needed for the random nanowires, accounting for the large intensity difference in the UV emission of the structures.

First we look at the ratio of the UV band-edge emission to the visible defect emission to determine qualitative differences between the samples. Figure 6.2 shows the full PL spectral range, from 340 – 650 nm, for all three samples at 80 K and at 300 K. The vertical nanowires have no detectable visible defect emission at either temperature, indicating highly crystalline nanowires. The broad, lower energy emission in the vertical nanowire PL is the p-GaN substrate emission. The random nanowires have a high integrated band-edge to visible emission ratio of 12.29 at 80 K and 10.49 at 300 K, which also indicates highly crystalline nanowires, though potentially with more defects than the vertical nanowires.[20] The randomly oriented nanowires are much thinner than the vertically oriented nanowires, which can lead to surface defects playing a more prominent role in the photoluminescence.[20] Finally, the nanopopcorn has a very low integrated band-edge to visible emission ratio (0.65 at 80 K and 0.72 at 300 K), indicating it is has the highest number of defects of the nanostructures studied. This is unsurprising, given the lack of distinct hexagonal facets in the nanopopcorn, and the much higher surface area of the structure, which can lead to increased surface defect interaction.

6.2.4 Temperature-Dependent Photoluminescence

Figure 6.3 shows the TD-PL of the ZnO vertical nanowires, random nanowires, and nanopopcorn, presented side-by-side for comparison of the general features of the spectra from each sample. Subsequent figures and discussion in Section 6.3 will analyze the details of the TD-PL spectra of each sample. Looking at Figure 6.3.a, the vertical nanowires have a sharp UV emission band, which narrows with decreasing temperature. The PL sideband is the p-GaN substrate emission. However, for the random nanowires, Figure 6.3.b, the broad emission at

room temperature does not narrow to a sharp point in the manner of the vertical nanowires. Instead, multiple lower energy shoulders are visible in the broad PL emission at low temperatures. In the nanopopcorn, Figure 6.3.c, instead of shoulders appearing, the UV peak becomes multiple distinct peaks at low temperatures. These peaks appear to be spaced periodically, reminiscent the TD-PL peaks associated with exciton-phonon coupling.[7,223]

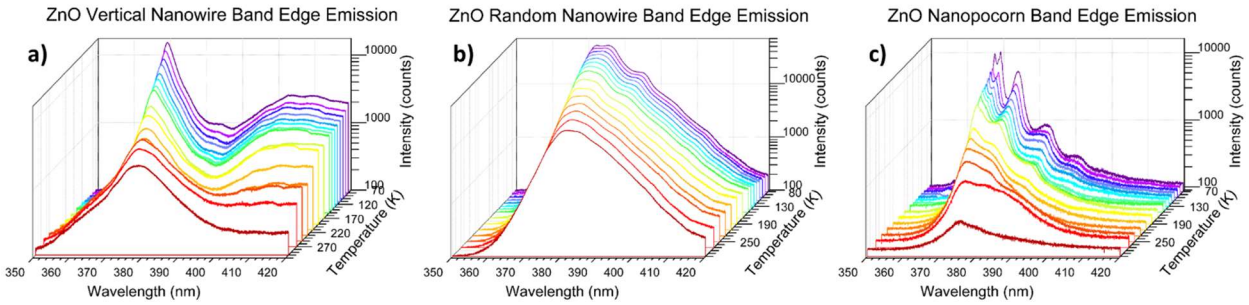

Figure 6.3: Temperature dependent photoluminescence (TD-PL), plotted on a logarithmic scale of a) vertical ZnO nanowires, b) random ZnO nanowires, and c) ZnO nanopopcorn. Subsequent figures will look more closely at the features of the TD-PL, but this overall view shows that the UV emission of each of these three nanostructures have distinct, unique, TD-PL characteristics.

In the TD-PL spectra of each sample in Figure 6.3, the peak UV emission energy blueshifts, increases in intensity, narrows in linewidth as the temperature decreases. In semiconductors, the temperature-dependent linewidth and intensity of the exciton emission depends strongly on exciton phonon-coupling, and the coupling strength can be determined when temperature-dependent measurements are recorded down to helium temperatures.[222] However, exciton-phonon coupling also contributes to the emission blueshift as temperature decreases, and the coupling is resolvable even at nitrogen temperatures.[224] As the semiconductor temperature decreases, the band gap increases (ΔE_g) because of two mechanisms, the first being a smaller

contribution due to temperature-dependent lattice dilation[225] and the second is larger contribution due to electron-phonon interaction.[224] Samples with the largest exciton-phonon coupling see the largest ΔE_g. The temperature (T) dependent contribution of the exciton-phonon (acoustic and optic) interaction to ΔE_g can be characterized by the empirical Varshni equation[223,224]

$$E_g = E_0 - \frac{\alpha T^2}{T + \beta} \qquad (6.1)$$

where E_0 is the energy of the band gap at 0 K, and α and β are the Varshni thermal coefficients; α empirically measures the bandgap energy shift as a function of temperature and β approximates the Debye temperature (T_D) of the sample. Specifically, α describes the $\Delta E_g \propto T^2$ dependence when T is below T_D, and β describes the $\Delta E_g \propto T$ dependence when T is above T_D.[224] The Debye temperature is the empirical low-temperature heat capacity for insulating crystalline solids which describes the cut-off temperature for high energy phonons. Above T_D all vibrational modes contribute to the heat capacity and below T_D only the low energy vibrational modes with wavelengths much longer than the atomic spacing of the crystal lattice need to be considered.[226] For ZnO, T_D is between 399.5 – 440 K.[7]

To study the temperature dependence of the ZnO UV emission, all TD-PL spectra for each sample were fit by a sum of Gaussian functions using Matlab or OriginPro. For the lowest temperatures of the nanopopcorn, the Gaussian function was a sum of up to twelve peaks, while for the highest temperatures of the vertical nanowires, the Gaussian function was a sum of only two peaks. Appendix A shows an example of these fits for each sample. From the literature, the highest-energy shoulder of the UV emission at 80 K is the A-exciton peak.[1,7,223] Figure 6.4 shows the peak positions of the A-exciton emission for the vertical nanowires, random nanowires, and nanopopcorn. The A-exciton emission blueshifts 76.8 meV, 89.2 meV, and

65.4 meV for the vertical nanowires, random nanowires, and nanopopcorn, respectively, all in the typical range for zinc oxide.[1,7] The nanopopcorn has the highest energy A-exciton emission and the random nanowires the lowest, all within typical ZnO UV emission ranges.[1,18,20]

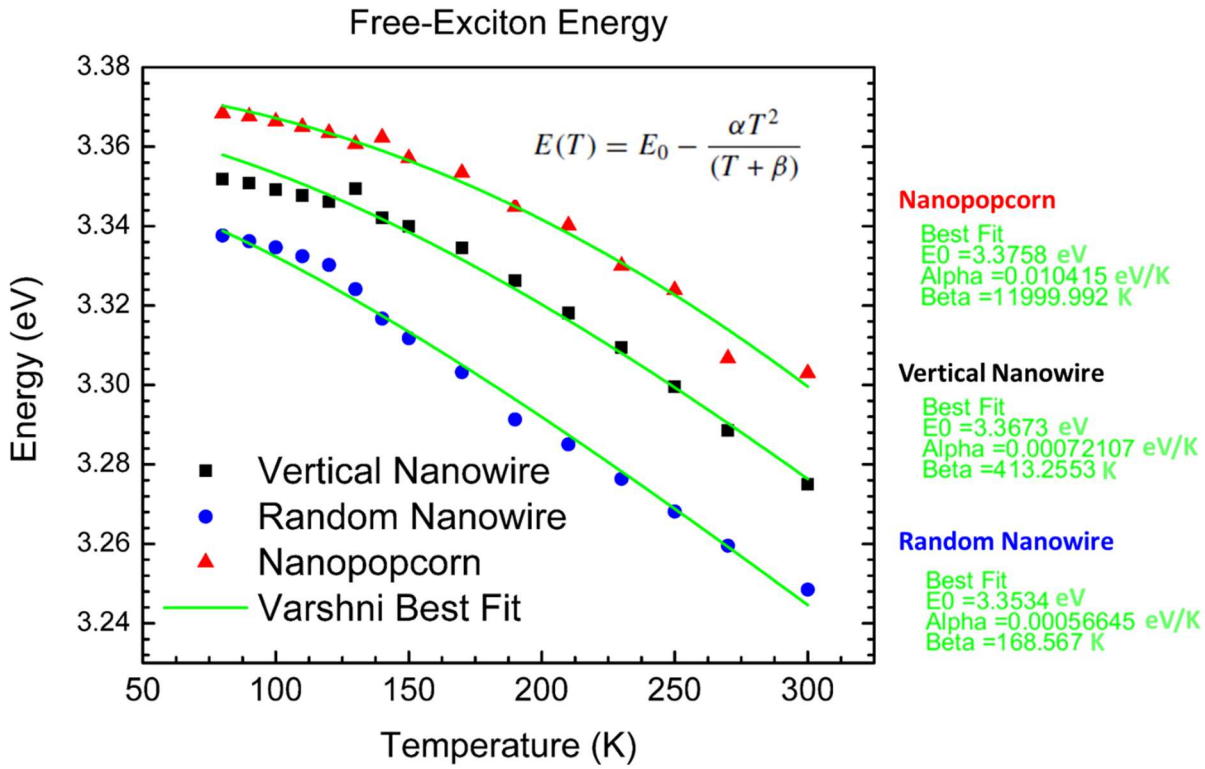

Figure 6.4: The peak positions of the free A-exciton emission in the vertical nanowires, random nanowires, and nanopopcorn, with a best fit to the temperature dependent energy shift using the Varshni equation (Equation 6.1). Constants α and β, as well as the 0 K A-exciton emission, E_0, are given for each sample, determined by the fit.

The temperature-dependent peak energies of the A-exciton are fit with the Varshni equation to determine the 0 K A-exciton transition energy and the Varshni thermal coefficients, and the best fits are plotted in Figure 6.4. Because the TD-PL only goes down to 80 K, and not down to 4 K, a data point was included at 0 K with an estimated A-exciton emission energy of 3.376 eV for the nanopopcorn and vertical nanowires and 3.350 eV for the random nanowires.[7]

For the vertical nanowires, the Gaussian fit of the A-exciton does not match the Varshni best fit at low temperature, indicating that the A-exciton should be at a high energy shoulder of the UV emission peak. Similar Varshni coefficients are found for the random nanowires and vertical nanowires, while the nanopopcorn is the outlier with both a higher 0 K A-exciton emission energy and higher thermal coefficients, even higher than the most defect-rich sample in the study by Mohanta, *et al*.[223] Mohanta, *et al* determined that the ZnO sample with the most surface defects had the highest β, suggesting that the nanopopcorn have more surface defects than the two nanowire structures. Additionally, the fit for the vertical nanowires yields a β equal to the ZnO Debye temperature, as the Varshni equation predicts when the defect level is low.[224]

From the measurements of the blueshift of the A-exciton peak from 300 – 80 K and the estimate of the 0 K A-exciton emission, it is determined that the randomly oriented nanowires have the largest A-exciton peak energy shift, suggesting the strongest exciton-phonon coupling.[224] In some ways, the exciton-phonon coupling is reduced in the nanopopcorn, which has the smallest A-exciton blueshift. However, the nanopopcorn also has the most noticeable LO-phonon replica-like peaks in the TD-PL, shown in Figure 6.3. Next, Raman spectroscopy is used to help determine what coupling mechanisms are at play.

6.2.5 Temperature-Dependent Raman Spectroscopy

Room temperature and low temperature Raman spectra were taken of the vertical nanowires, random nanowires, and nanopopcorn, using the same cryostat, HeCd 325 nm laser, and detector as the TD-PL. The acquisition software (LabSpec Version 5.78.24) was put into Raman acquisition mode (instead of photoluminescence acquisition mode) to measure the

emission in units of inverse centimeters from the excitation wavelength. Scans were taken from 200 - 2400 cm^{-1} with an integration time of 120 s and four scans were averaged to reduce noise.

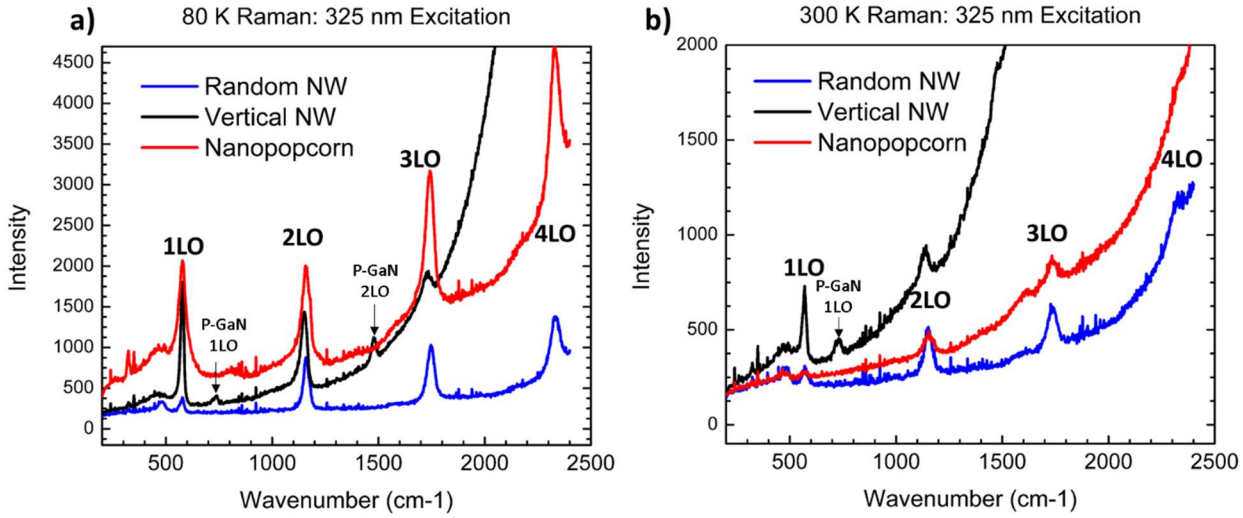

Figure 6.5: Raman spectra of the random nanowires, vertical nanowires, and nanopopcorn taken with a 325 nm excitation at a) 80 K and b) 300 K. Positions of the longitudinal optical (LO) phonon (71 – 73 meV) are assigned, with the p-GaN substrate also contributing an LO phonon mode.

Figure 6.5 shows the Raman spectra of the vertical nanowires, random nanowires, and nanopopcorn at 80 K and 300 K. The two ZnO longitudinal optical phonon modes have energies of 71 – 73 meV, corresponding to 572 – 588 cm^{-1}.[7] All three samples have distinct longitudinal optical phonon peaks for the first to fourth order LO phonon modes. The UV band-edge emission from the vertical nanowires obscures any LO phonon modes higher than third order. The p-GaN substrate of the vertical nanowires also contributes a first and second order LO phonon mode. For the vertical nanowires, the LO phonon modes present at 80 K range from 572 – 584 cm^{-1}, and at 300 K from 568 – 571 cm^{-1}. For the random nanowires, the LO phonon

modes at 80 K and 300 K range from 575 – 588 cm^{-1} and 570 – 588 cm^{-1}, respectively. For the nanopopcorn, the LO phonon modes at 80 K and 300 K range from 576 – 593 cm^{-1} and 570 – 586 cm^{-1}. In all samples the LO phonon energy is lower at higher temperatures, which indicates the ZnO lattice structure expanded with increasing temperature, as is expected in dielectrics.

The intensity of the Raman spectra of the LO phonons varies with nanostructure and with phonon order, meaning the exciton-phonon coupling strength also varies with nanostructure and phonon order. The vertical nanowires have a strong first-order LO phonon with weaker higher order modes at both 80 K and 300 K. The random nanowires have a weak first-order LO phonon, with stronger higher order modes at both temperatures. The LO phonon modes of the nanopopcorn are almost equal in intensity at 80 K, and have a slight redistribution away from the first order mode at 300 K. Overall, the 300 K LO phonon modes are weaker than the 80 K LO phonon modes for all three samples.

Next, for each sample, for both the 80 K and 300 K Raman spectra, the ZnO first to fourth LO phonon modes were fit individually with a single Lorentzian peak (using OriginPro). Examples of these fits are given in Appendix A. The intensity and full-width half-maximum (FWHM) of these fits are shown and discussed in Section 6.3, along with detailed descriptions and peak assignments of the TD-PL of each sample.

6.3 Discussion

6.3.1 Nanopopcorn

As the nanopopcorn has the most distinct TD-PL UV emission peaks, Figure 6.1, we analyze its TD-PL and Raman spectroscopy first, in order to clearly give peak assignments

before moving to the less distinct peaks in the TD-PL spectra of the vertical nanowires and random nanowires.

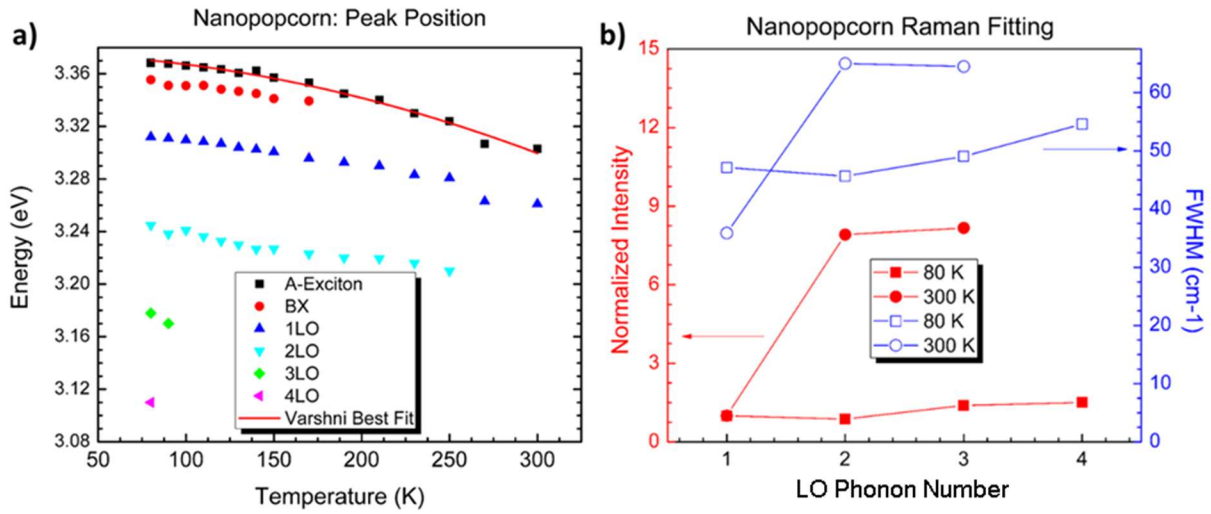

Figure 6.6: Nanopopcorn a) photoluminescence Gaussian fitting and b) Raman spectroscopy Lorentzian fitting. a) Peak positions of the Gaussian fits to the TD-PL spectra, identifying the A-Exciton (with Varshni best fit), bound exciton complexes (BX), and the 1st – 4th LO phonon replicas of the A-exciton. B) Peak intensities and the full-width half-max of Lorentzian fits to the Raman spectra LO phonon peaks 1 - 4 at 80 K and 300 K.

The full UV energy range of the TD-PL was fit with Gaussian functions, shown in Figure 6.6.a. The free A-exciton peak position is shown with the empirical Varshni best fit, which demonstrates that the thermal expansion of the lattice occurs as expected.[226] The energy of the LO phonon of ZnO is 71 – 73 meV,[1,7] and thus TD-PL peak positions spaced approximately the LO phonon energy apart were assigned as free-exciton LO phonon replicas.[1] Looking to the Raman fitting data presented in Figure 6.6.b, at 80 K the LO phonon has the same intensity in its first to fourth order modes, which verifies the presence of four FX-LO phonon replicas in the low temperature spectra. All of these phonon modes are identified in Figure 6.7, redisplaying the TD-PL of the nanopopcorn, now with marked peak positions. At 300 K, the FWHM of the LO

Raman modes in Figure 6.6.b increases, except for the first LO mode. The broadened LO modes can still couple to the free-exciton emission, however, the broadened LO phonon replicas in the TD-PL are less distinct, becoming indistinguishable in the UV band-edge emission at room temperature, as shown in Figure 6.7.

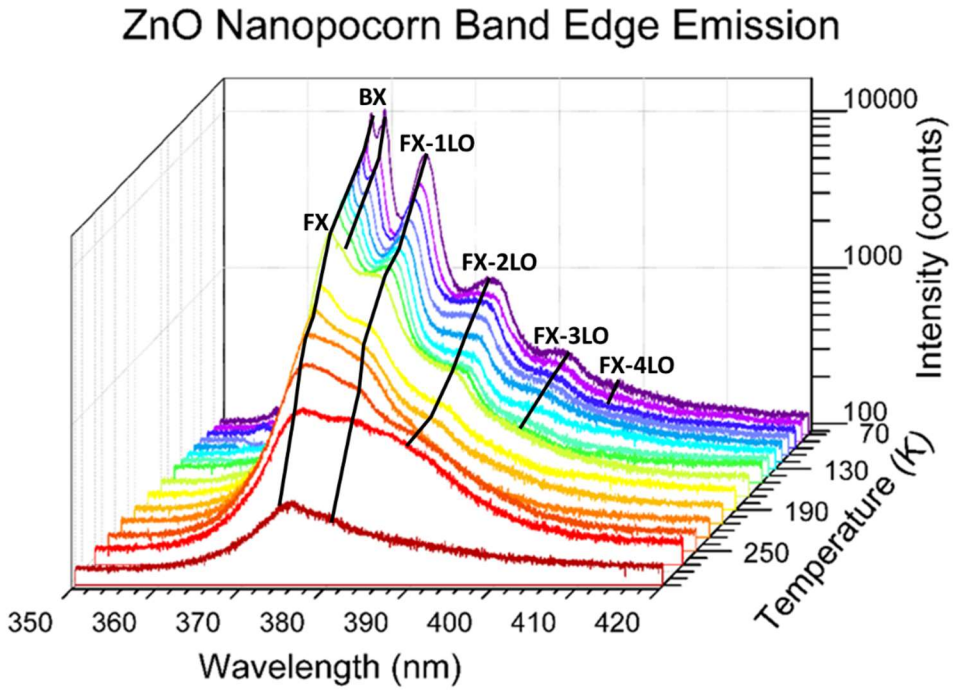

Figure 6.7: ZnO nanopopcorn temperature dependent UV photoluminescence with peak assignments for the free-exciton (FX), bound exciton complexes (BX), and free-exciton longitudinal phonon replicas FX-(1-4)LO.

So far, the TD-PL peak assignments have yet to identify the one set of Gaussian peaks that were not either the free exciton or the free-exciton phonon replicas, starting at 3.355 eV at 80 K, Figure 6.6.a. This peak is actually a superposition of bound exciton emissions.[7,223] Fitting the ZnO nanopopcorn 80 K PL spectrum (using a function of twelve Gaussians, Appendix A) shows that there are at least two sharply defined bound exciton peaks at 3.3599 eV and

3.3555 eV, with a third, less pronounced shoulder at 3.3518 eV. Additionally, the sharp peak above the A-exciton emission is also a bound exciton, at 3.3703 eV. The ZnO defects, such as oxygen and zinc vacancies/interstitials and other interstitial atoms, trap the free exciton at lower temperatures, localizing the bound exciton to the defect site.[7] This localization leads to the sharper emission of the ZnO bound excitons because they do not scatter and broaden significantly from interaction with acoustic phonons.[1] The nanopopcorn was grown on GaN, and Ga defects in ZnO have a known 3.598 eV emission, thus the 3.599 eV peak is assigned to a Ga bound exciton.[1,227] The strongest peak at 3.555 eV is attributed to neutral acceptor (commonly Na and Li) bound excitons, and other neutral acceptor bound excitons can be attributed to the 3.3518 eV shoulder.[1,227,228] The highest energy bound exciton (3.3703 eV) is typically attributed to B excitons bound to the neutral donor.[1,8,220,221]

Overall, for the nanopopcorn, the presence of the strong bound exciton emission lines, coupled to the highest intensity visible emission of the three samples, shows that the nanopopcorn has a significant number of defects. The presence of the strong A-exciton to LO-phonon coupling indicates the presence of surface defects.[223] Alternatively, a smaller change in the A-exciton emission energy with temperature indicates less coupling of the A-exciton and phonons, suggesting that while the A-exciton to LO-phonon coupling is strong, the A-exciton coupling to other phonons, such as the lower energy acoustic phonons, could be much weaker. The presence of the large number of defects in the nanopopcorn suggests that acoustic phonons could propagate shorter distances in the nanopopcorn, as the phonons scatter from the numerous defect centers.[229] These overall data conclude that the ZnO nanopopcorn nanostructure is defect rich, with both surface and bulk defects.

6.3.2 Random Nanowires

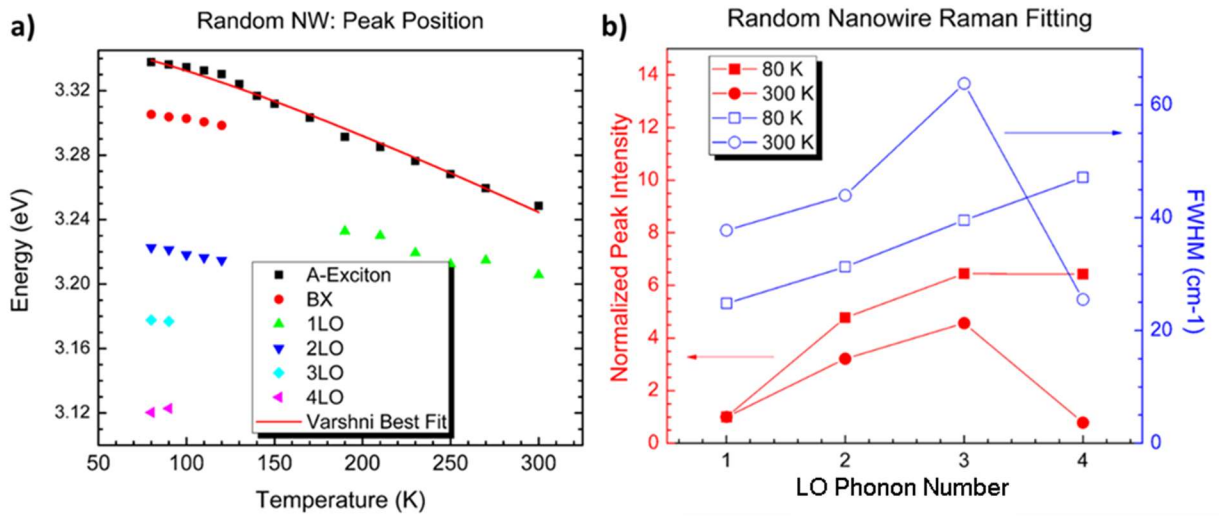

Figure 6.8: Random Nanowire a) photoluminescence Gaussian fitting and b) Raman spectroscopy Lorentzian fitting. a) Peak positions of the Gaussian fits to the TD-PL spectra, identifying the A-Exciton (with Varshni best fit), bound excitons complexes (BX), and the 1st – 4th LO phonon replicas of the A-exciton. B) Peak intensities and the full-width half-max of Lorentzian fits to the Raman spectra LO phonon peaks 1 - 4 at 80 K and 300 K.

Next we analyze the TD-PL and Raman spectra of the random nanowires. The same Gaussian fits that were used to determine the A-exciton peak energies also fit peaks to the rest of the UV energy range, Figure 6.8.a (Appendix A). The free A-exciton peak position is shown with its Varshni best fit. Shoulders in the UV emission, fit with Gaussian functions, were found to be approximately the LO phonon energy apart, and thus were again assigned as free-exciton LO phonon replicas.[1] However, the first-order LO phonon mode is missing. Looking to the Raman fitting data presented in Figure 6.8.b, at 80 K the first-order LO phonon has a much smaller intensity than the second, third, and fourth order modes, which verifies both the presence of the three higher FX-LO phonon replicas in the low temperature spectra and the lack of an FX-1LO replica. All of these modes are identified in Figure 6.9, redisplaying the TD-PL of the

random nanowires, now with marked peak positions. At 300 K, the FWHM of the LO Raman modes increases, except for the fourth LO mode, which decreases. In the same manner as the nanopopcorn, the broadened LO modes still couple to the free-exciton emission, with only the first LO mode distinguishable from the Gaussian function of the UV band-edge emission at room temperature, as marked in Figure 6.9.

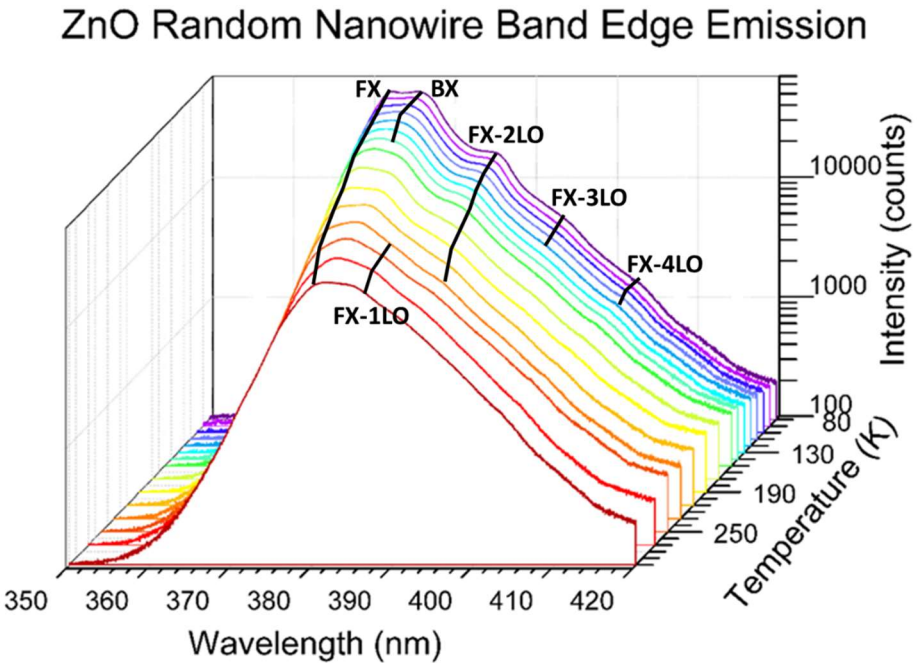

Figure 6.9: ZnO random nanowire temperature dependent UV photoluminescence with peak assignments for the free-exciton (FX), bound exciton complexes (BX), and free-exciton longitudinal phonon replicas FX-(1-4)LO.

The red data points in Figure 6.8 are from a broad Gaussian fitting to the TD-PL spectra and represent a superposition of defect bound excitons in the random nanowires, shown as the first shoulder to the A-exciton emission in Figure 6.9. This bound exciton emission is centered at 3.305 eV at 80 K, which is typically attributed to surface states.[1,219] However, the fit is a

broad Gaussian peak, so it is most likely a combination of multiple surface states and other bound excitons.

The random ZnO nanowires have the largest free-exciton energy shift with temperature. They also have a strong A-exciton to LO phonon coupling present in the TD-PL. This data combined suggests that the random nanowires have the overall strongest exciton-phonon coupling. The large A-exciton to LO phonon coupling suggests the presence of surface defects,[223] confirmed by the surface bound exciton emission. The presence of excitons bound to surface defects without any excitons bound to intrinsic bulk defects, suggests that the random nanowires have fewer bulk defects that the nanopopcorn. When this is combined with the fact that the random nanowires have the largest A-exciton energy shift, it suggests that the random nanowires are a highly crystalline structure that can allow acoustic phonons to propagate farther and thus interact with more bulk excitons,[229] for stronger exciton-acoustic phonon coupling. Increased coupling with acoustic phonons is not the only potential explanation for the large blue-shift of the A-exciton at lower temperature, however, because coupling to other phonon modes or a larger change in the lattice spacing are additional factors.[224] Additionally, this broadening of the UV emission obscures the LO phonon replica peaks, causing the phonon replica emissions to appear as shoulders in the TD-PL instead of as distinct peaks. Thus, it is determined that the random nanowires have few bulk defects, leading to their strong A-exciton UV emission and lack of a strong visible emission centered at 520 nm (Figure 6.2). The random nanowires do have many surface defects, which leads to the strong LO-phonon replicas at low temperature.

6.3.3 Vertical Nanowires

Finally, the TD-PL and Raman spectra of the vertical nanowires are analyzed. Again, Gaussians functions were fit to the full energy range, Figure 6.10.a. The free A-exciton peak position is shown with its Varshni best fit, indicating that thermal expansion occurs in the sample, as expected. Three Gaussian functions were fit to the sharp UV emission peak at low temperature (Appendix A), with the highest energy assigned to the free A-exciton emission, and the second highest to that of bound excitons. The bound exciton emission is centered at 3.325 eV at 80 K, which has been assigned to structural defect bound excitons, common in annealed ZnO nanowires grown at low temperature, such as the vertical nanowires.[1,230]

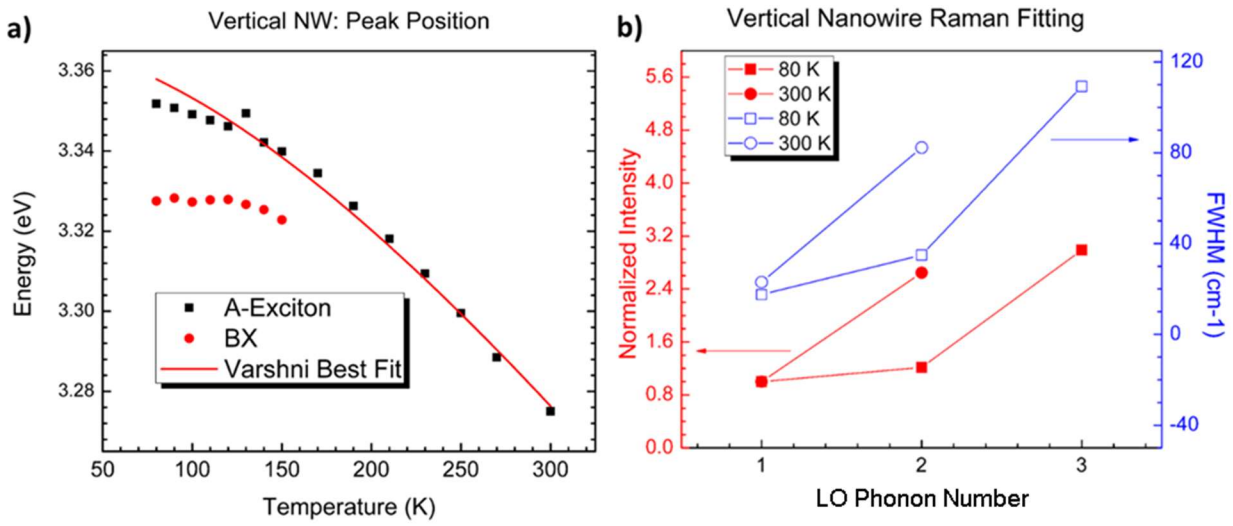

Figure 6.10: Vertical Nanowire a) photoluminescence Gaussian fitting and b) Raman spectroscopy Lorentzian fitting. a) Peak positions of the Gaussian fits to the TD-PL spectra, identifying the A-Exciton (with Varshni best fit) and bound excitons complexes (BX), no LO phonon replicas were fit through Gaussian fitting. B) Peak intensities and the full-width half-max of Lorentzian fits to the Raman spectra LO phonon peaks 1 - 3 at 80 K and 300 K.

In the fit, the third Gaussian was not centered at an energy typical for a phonon replica (not shown in Figure 6.10.a), however, a shoulder is visible at 80 K and above that appears to be the first LO phonon replica of the A-exciton, assigned as such in Figure 6.11. Looking to the Raman fitting data presented in Figure 6.10.b, at 80 K the first order LO phonon has a much larger intensity than any of the other LO phonon replicas, which indicates that it is most likely present as a shoulder in the UV emission peak. All of these identified emissions are indicated in Figure 6.11, along with locating the p-GaN emission (as measured in Figure 6.2.b, inset). The lack of higher-order LO phonon Raman peaks confirms the lack of distinct LO-phonon replicas at any temperature, though a visible second shoulder (not fit with a Gaussian) is at the right position to be the second-order LO phonon replica.

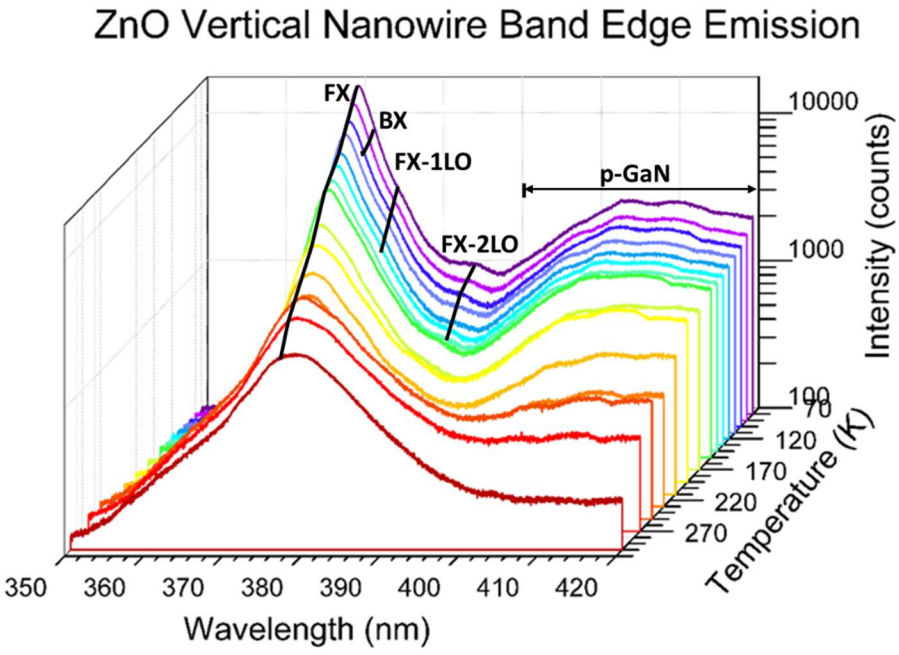

Figure 6.11: ZnO random nanowire temperature dependent UV photoluminescence with peak assignments for the free-exciton (FX), bound exciton complexes (BX), and free-exciton longitudinal phonon replicas FX-(1-2)LO. The FX-LO phonon replicas are assigned by eye, from 2 shoulders in the data at approximately 70 meV spacings.

Putting these data together, the vertical nanowires have very few defects in comparison to the other two ZnO nanostructures. The vertical nanowire A-exciton emission does not couple strongly to higher order LO phonons, indicating fewer surface defects.[223] Structural defects do exist, from the energy position of the bound excitons, but the free exciton emission at 80 K is still much more prevalent than any individual bound exciton emission. Additionally, the presence of the structural defects might decrease the exciton-acoustic phonon coupling in the sample,[229] which could lead to the smaller shift in free exciton energy with temperature than what was seen in the random nanowires, which had the largest energy shift.

6.4 Conclusions

The temperature-dependent photoluminescence and Raman spectra illuminated the defect types in three ZnO nanostructures, that of nanopopcorn, random nanowires, and vertical nanowires. The ZnO nanopopcorn have the most defects, with both bulk and surface defects in the nanostructure leading to strong exciton-LO phonon coupling in the TD-PL, sharp bound exciton emissions in the TD-PL, and the largest visible emission. The random nanowires have only surface defects, indicated by the strong coupling between the A-exciton and LO phonon and confirmed by the position of the bound exciton emission. The random nanowires also had largest A-exciton energy shift, which could be caused by an overall stronger exciton-phonon coupling than the other two structures. This suggests that other phonons, such as acoustic phonons, also strongly couple to the exciton emission. Acoustic phonons have a longer propagation length in crystals with fewer bulk defects, indicating that the random nanowires should have few bulk defects, as the high band-edge-to-visible emission ratio of the TD-PL

already indicates. Finally, the vertical nanowires showed almost no evidence of surface defects, with no visible emission and small coupling to higher order LO-phonons. This led to the sharpest UV band-edge emission of all three nanostructures, with only structural defects present.

Overall, this research shows that the nanowire morphology of ZnO is preferable for UV emission applications, and the vertically oriented ZnO nanowires have the strongest, most defect free emission, ideal for nanolasers applications.[231] The ZnO nanopopcorn, on the other hand, is a very porous, defect-rich structure, and may be ideal for random lasing applications.[39]

6.5 Acknowledgements

This chapter has fewer collaborations than the rest of my work. However, I thank Prof. Akira Ueda for all his assistance in getting the cryostat chamber working for these experiments. Additionally, I thank Prof. Sergey Avanesyan for training and helping me with time-resolved spectroscopy of these samples, even though a complete set of time-resolved measurements did not come to fruition before my defense due to the low signal to noise ratio of the current experiment design, and thus are not included here. I thank Eion Hindsman-Curry, a summer REU student, for working with me on the microscopy analysis of the nanopopcorn. Finally, I thank my advisors, Prof. Richard Mu, and especially Prof. Richard Haglund, for spending time analyzing the results of each new data set with me.

CHAPTER 7

OUTLOOK: TOWARDS ZINC OXIDE LASING

This chapter presents two applications of the vertically oriented "carpet" ZnO nanowires, using plasmon-exciton coupling to enhance the UV band edge emission of nanowire devices. The first application is that of plasmon enhanced UV light-emitting diodes. The second application is UV nanolasing in ZnO nanostructures, where vertically-oriented nanowires can support a Fabry-Perot lasing cavity, and nanopopcorn could support random lasing. Coating these structures in metal nanoparticles will enable studies of plasmon-exciton coupling in ZnO lasing, moving toward efficient on-chip UV nanolasers.

7.1 ZnO Nanowire Applications

7.1.1 Application Overview

Light-emitting diodes (LEDs) and laser diodes using semiconductor nanowire architectures are attractive because of their high crystallinity and electron transport properties, strong optical confinement, high directionality, and waveguided emission.[232-239] Zinc oxide is regarded as a promising material for UV light-emitting devices, with recent reports on ZnO nanowire waveguide-type LEDs and lasers.[33,34,239-242] Lai *et al* fabricated a UV LED based on a vertically-oriented ZnO nanowire array, obtaining waveguided electroluminescence (EL).[240] Plasmons-exciton coupling has been demonstrated as an UV emission enhancement mechanism in a ZnO nanowire LED by Liu *et al*.[62] Additionally, Zhu *et al* achieved electrically pumped waveguide lasing with a ZnO nanowire array homojunction diode.[242]

Ultraviolet lasing from ZnO nanowires nanolasers was first demonstrated by Huang *et al*[11] in 2001, and has been a topic on great interest since,[11,34,63,97,243] but only recently has lasing been shown in plasmon-exciton coupled ZnO nanowire systems.[25,26,243] A recent study by Lu *et al* has shown lowering of the lasing threshold of ZnO hexagonal microtowers due to coupling to Al nanoparticle plasmons.[26] Additionally, Sidiropoulos *et al*[25] used a metal thin film coupled to single ZnO nanowire to study plasmon-exciton coupled systems in order to confine light pulses for sub-diffraction limited, high-intensity emission. These plasmon-exciton coupled systems with Fabry-perot cavity lasing[35,231,244] have not been studied in uniformly oriented "carpet" ZnO nanowire arrays. A vertical nanowire array is an ideal waveguide and gain medium for laser cavities, direct integration for optical components, and even on-chip optical-integrated photonic devices.[2,245,246] Such an array has been experimentally shown using GaN nanowires for a dielectric microcavity.[247] An additional lasing demonstration has been shown in densely packed ZnO nanoparticles, by Appavoo *et al*, with no cavity present; instead the mechanism for population inversion and enhanced emission was that of random lasing.[39]

7.1.2 Plasmon Enhanced Light-Emitting Diodes

A silver nanoparticle-coated ZnO LED has been demonstrated that exhibits enhanced UV electroluminescence and photoluminescence. The ZnO LED used hydrothermally grown, vertically-oriented ZnO nanowires. Exciton-plasmon coupling occurs in the LED due to a waveguide-like propagation of the exciton or the exciton-polariton along the length of the ZnO nanowire. This work was funded by the NSF East Asia and Pacific Summer Institute, and is published:[21]

- C. Zhang, **C.E. Marvinney**, H.Y. Xu, W.Z. Liu, C.L. Wang, L.X. Zhang, J.N. Wang, J.G. Ma, Y.C. Liu, *Enhanced waveguide-type ultraviolet electroluminescence from ZnO/MgZnO core/shell Nanorod array light-emitting diodes* via *coupling with Ag nanoparticles localized surface plasmons*. Nanoscale, 2015. **7**(3): p.1073-1080.

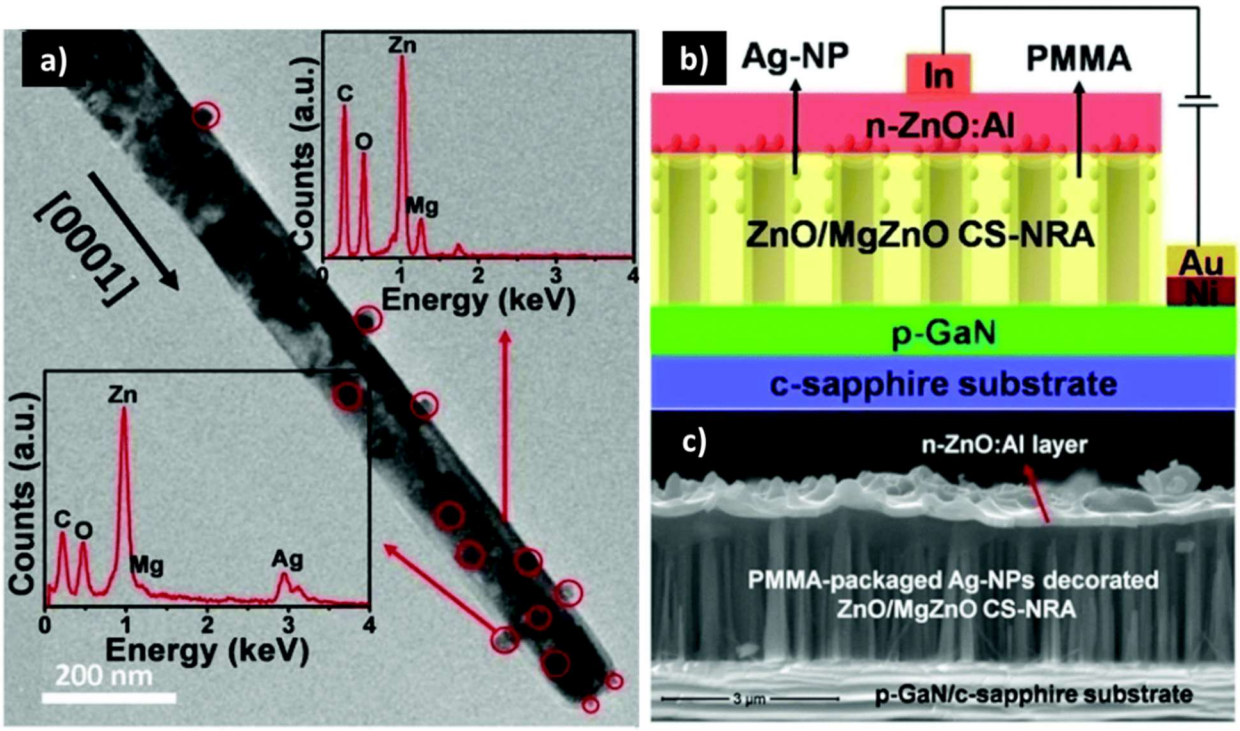

Figure 7.1: a) Typical TEM image of a single ZnO/MgZnO CS-NR with Ag-NP decoration; the two insets show the energy-dispersive x-ray spectroscopy energies collected from the CS-NR and an Ag-NP. The Ag-NP cluster at the tops of the CS-NR. b)-c) structural schematic diagram and a typical cross-sectional SEM image of the Ag-NPs decorated CS-NRA LED device.

Localized surface plasmon (LSP) enhanced waveguide-type ultraviolet light-emitting diodes (LEDs) were fabricated by sputtering Ag nanoparticles (Ag-NP) onto ZnO/MgZnO core-shell nanorod array (CS-NRA)/p-GaN heterostructures. The vertically oriented ZnO nanowires (Chapter 2, Figure 2.13) were grown via a low temperature hydrothermal method (Section 2.2.1)

and MgZnO was deposited using pulsed laser deposition.[21] The coated nanowires are shown in Figure 7.1.a, with the Ag nanoparticles primarily coating the tops of the CS-NR due to the sputtering deposition process. The finished device is shown in Figure 7.1.b-c. The Ag-NP coated CS-NRA was packaged in PMMA, and transparent conductive n-ZnO:Al layer was deposited on top using pulsed laser deposition.[21] Metals Ni/Au and In were deposited as the p-type and n-type contact electrodes, respectively.

Before LED device fabrication, photoluminescence measurements were taken of the Ag coated and uncoated CS-NRA to determine if plasmon-exciton coupling existed in the system. The Ag-coated sample exhibited a ~10-fold enhancement of the ZnO UV PL over the bare ZnO NRA, as seen in Figure 7.2.a. This significant improvement is ascribed to a spectral overlap between the ZnO UV luminescence and the Ag LSP resonance extinction, as shown in the inset of Figure 7.2.a. This inset describes the dependence of the enhancement ratio (Ag-NP coated to uncoated CS NRA) on the emission wavelength. The spectral overlap indicates the possibility of resonant coupling between ZnO excitons/polaritons and Ag LSPs, especially at the tops of the NRA where the Ag-NPs are clustered.

After fabrication of the LED CS-NRA device shown in Figure 7.1.b-c and described in Zhang *et al*,[21] the electroluminescence (EL) of the Ag-coated versus uncoated device was studied. As seen in Figure 7.2.b, a ~9-fold enhancement of ZnO UV EL was demonstrated by the Ag-NP decorated LED compared with the device without Ag-NPs. The inset describes the enhancement ratio at the 10 mA injection current. Overall, Figure 7.2.b. highlights the three emission bands present in the CS-NRA LED, the 380 nm ZnO exciton emission, the 435 nm p-GaN Mg-acceptor emission, and the 545 nm ZnO defect emission. The 380 nm ZnO exciton emission is enhanced nine-fold while the 435 nm peak is only enhanced four-fold. The most

effective EL enhancement is in the wavelength range from 380 – 400 nm, matching the photoluminescence enhancement curves seen in the inset of Figure 7.2.a. This suggests that the PL and EL enhancement curves arise from the same mechanism. Additionally, an increased spontaneous emission rate, from 61 ps to 6 ps, observed in time-resolved spectroscopy of the Ag-nanoparticle coated samples, indicating that the ZnO EL enhancement and PL enhancement was attributed to LSP–exciton/polariton coupling.[21]

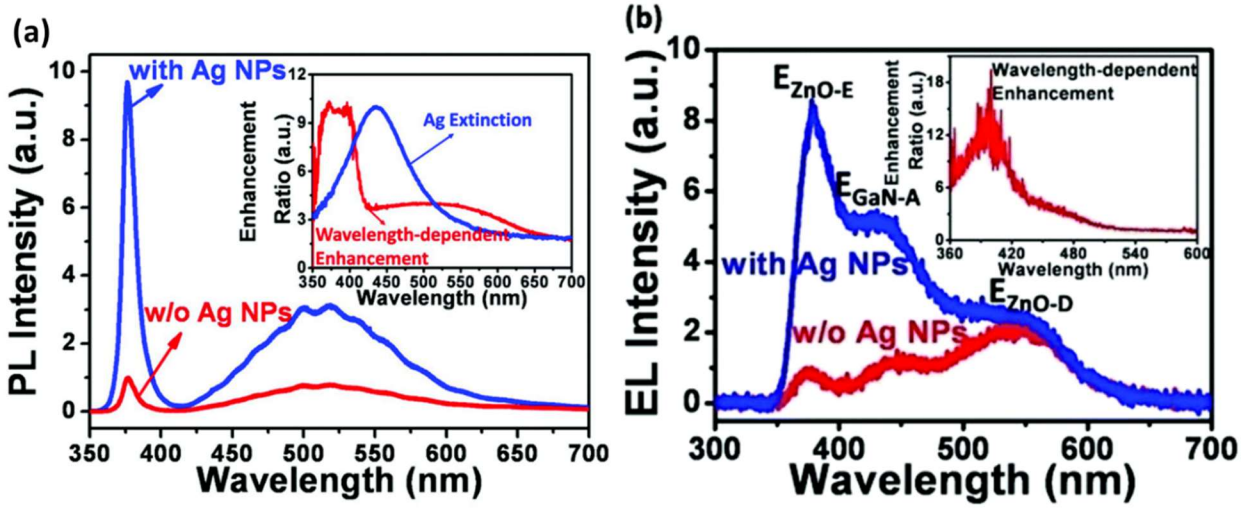

Figure 7.2: (a) PL spectra of ZnO/MgZnO CS-NRAs with (blue line) and without (red line) Ag-NPs. The 325 nm line of a He–Cd laser was employed as the excitation source. The inset shows the extinction spectrum of coated Ag-NPs (blue line) and the dependence of the PL enhancement ratio on the emission wavelength (red line). (b) EL spectra of the devices with (blue line) and without (red line) Ag-NPs obtained at the injection current of 10 mA; the inset shows the dependence of the EL enhancement ratio on the emission wavelength.

In the Ag-NP coated CS-NRA, direct exciton-plasmon coupling can be achieved in the photoluminescence measurements because in the PL measurement technique the ZnO excitons are excited primarily near the tops of the ZnO nanowires, where the Ag-NP plasmons are concentrated. However, in the electroluminescence LED design this coupling is difficult to achieve because of the "remote" separation between the Ag-LSPs at the top of the nanowires and

electron–hole pairs in the active region at bottom of the nanowires, located between the ZnO and p-GaN. Thereby, two possible models involving the dynamic process of interactions among excitons, photons, and LSPs, were established to understand the selective enhancement of ZnO EL, as seen in Figure 7.3.c-d. The first process is exhibited if waveguiding of the ZnO exciton occurs along the length of the ZnO nanowire, enabling the excitons to couple to the Ag plasmons. The second process is exhibited if polariton migration occurs along the length of the nanowire, enabling the exciton-polariton to interact with the Ag plasmons. Figure 7.3.a-b shows the angle-dependent EL measurements and as finite-difference time-domain (FDTD) simulations that confirmed the existence of a waveguide-type EL transmission mode along the NR's axial direction. The waveguide-type EL confirms that both coupling mechanisms are possible in the Ag-NP coated ZnO CS NRA.

In summary, a near-UV LED prototype device based on ZnO/MgZnO CS-NRA/p-GaN heterostructures was demonstrated in which the vertically-oriented ZnO nanowires act as an optical waveguide. Both the UV PL and EL was selectively enhanced by coupling with Ag LSPs. Two dynamic processes are attributed to the enhancement of the UV emission enhancement of the Ag-NP coated ZnO core-shell nanowire arrays, that of LSPR–exciton and LSPR–polariton coupling. This system is ideal for future efficient UV optoelectronic and all-optical applications. In particular, the vertical ZnO nanowire array is ideal for lasing applications, where the plasmonic nanoparticle coating can be used to reduce the lasing threshold[184] for more efficient on-chip lasing applications.

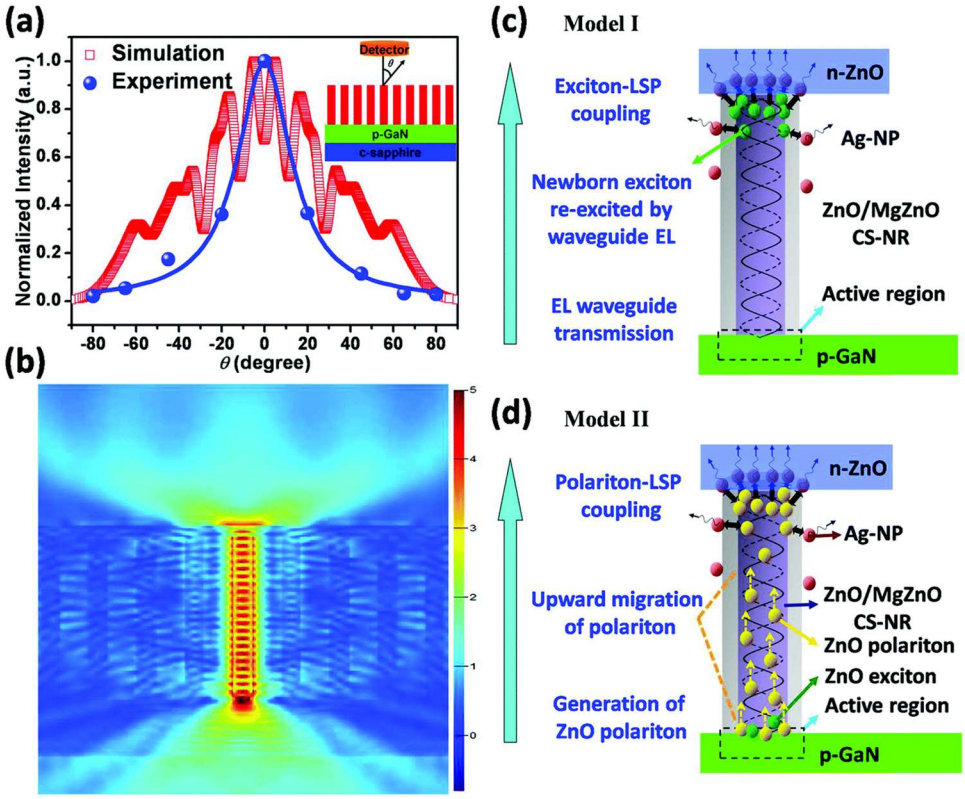

Figure 7.3: (a) The measured (blue ball) and simulated (red square) angle-dependence of the EL intensity for a CS-NRA LED; the inset exhibits the schematic diagram of the angle-dependent EL measurement configuration. (b) FDTD simulation of the EL intensity spatial distribution from a single NR optical waveguide. (c) and (d) Two models showing the dynamic process of interactions among excitons, photons, and LSPs in an Ag-NPs decorated CS-NR.

7.1.3 Towards Plasmon Enhanced ZnO Nanostructure Lasing

The logical extension of the above work on plasmon enhanced ZnO LEDs is to study plasmon enhanced ultraviolet lasing from ZnO nanostructures. The research will be focused on two possible nanostructures for nanolasing applications. First, the lasing characteristics of the vertically-oriented ZnO nanowires will be studied, both coated and uncoated with plasmonic nanoparticles to study the influence of plasmon-exciton coupling on the lasing emission and threshold power. These vertically-oriented nanowires can created a Fabry-Perot laser cavity, due to the reflective, faceted ends of the nanowires.[35,231,244] Figure 7.4 shows a schematic of the

optimal design of the plasmonic nanowire nanolasers that will be studied with optical pumping. At present, preliminary experiments are underway on the already grown vertically-oriented ZnO nanowires. This experiment studies the UV lasing of the nanowires using the 355 nm line of a Nd:YAG nanosecond pulsed laser. When completed, the work will be published with the following collaborators and any future contributors:

- C.E. Marvinney, K. Hallman, J. Robinson, Y. Cai, S. Avanesyan, H.Y. Xu, R.R. Mu, R.F. Haglund

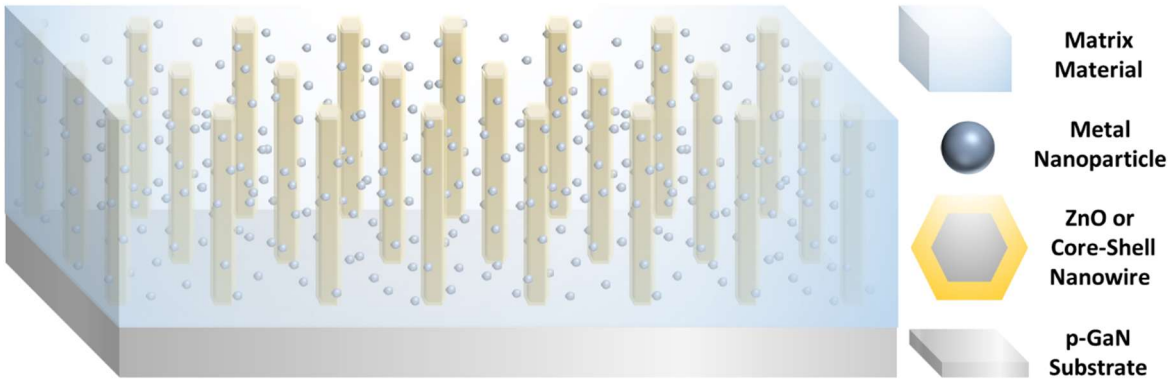

Figure 7.4: Vertical ZnO nanowire nanolasers design. A matrix material (polymer, i.e. PMMA) encapsulates the nanoparticle, dispersing them between the nanowires. Controlling the density of the metal nanoparticles will optimize the ZnO UV lasing.

The second research direction is that of random lasing in the ZnO nanopopcorn, as the nanopopcorn have a similar morphology to nanoparticle films that have previously demonstrated random lasing.[39] Plasmon-exciton coupling with the nanopopcorn structure would enable control of the lasing threshold, and is a promising direction for a second phase of the nanopopcorn random lasing research.

7.2 Acknowledgements

For the LED work in this chapter, I thank my collaborators at Northeast Normal University, Prof. Yichun Liu, Prof. Haiyang Xu, Dr. Cen Zhang, and Dr. Weizhen Liu, for their offer for me to work with them on this project, allowing me to help analyze the results and edit the manuscript for the experiments they were already conducting. I especially thank Cen Zhang for the majority of the writing of the paper this section is parsed from and for making the figures presented in Section 7.1.2. For the lasing work in this Chapter, I thank my collaborators at Vanderbilt Univeristy. First, I thank Kent Hallman for providing his expertise on laser design. Second, I thank Joshua Robinson, an REU student, for designing the laser set-up. Third, I thank Yujia Cai, and undergraduate, for doing initial experiments with Kent and I on this project. Finally, I thank Prof. Haglund, Prof. Sergey Avanesyan, and Kent Hallman for their interest in continuing or teaching various parts of this project when I have left, provided there is a willing graduate student to pick up the main project.

APPENDIX

A. Temperature-Dependent Photoluminescence and Raman Fitting

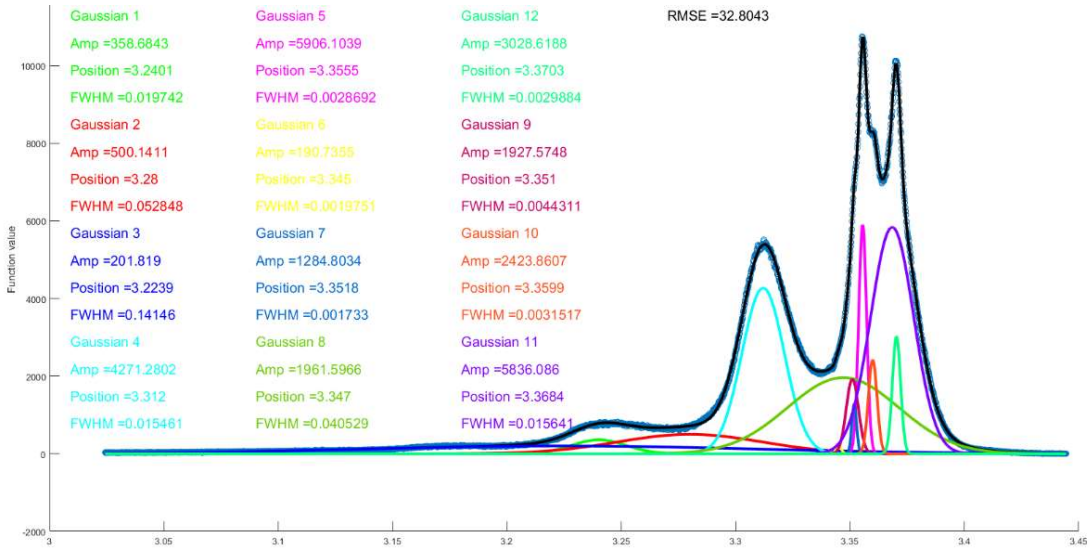

Figure A.1: Experimental photoluminescence intensity versus energy (eV) of ZnO nanopopcorn at 80 K (blue circles), with a sum of twelve Gaussian functions (Matlab fit) overlaid on the experimental data in black. Each Gaussian is independently shown with a color matching to the text describing the amplitude, position, and full-width half-maximum (FWHM) of the Gaussian.

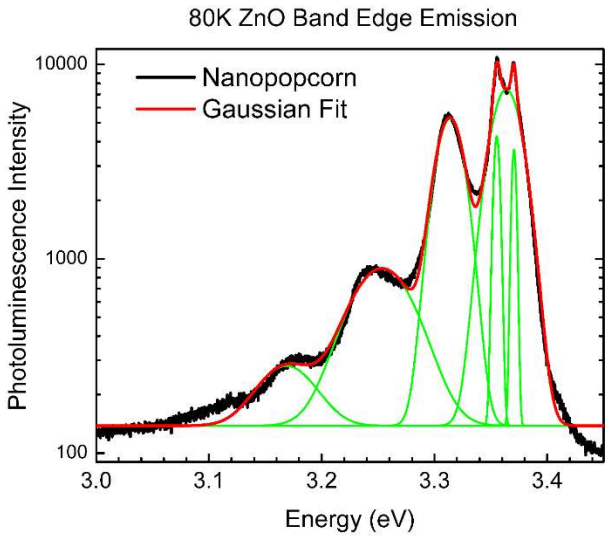

Figure A.2: Photoluminescence intensity versus energy (eV) of random ZnO nanowires at 80 K (black line), with a sum of six Gaussian functions overlaid in red on the experimental data. Each Gaussian is independently shown in green, fit using OriginPro.

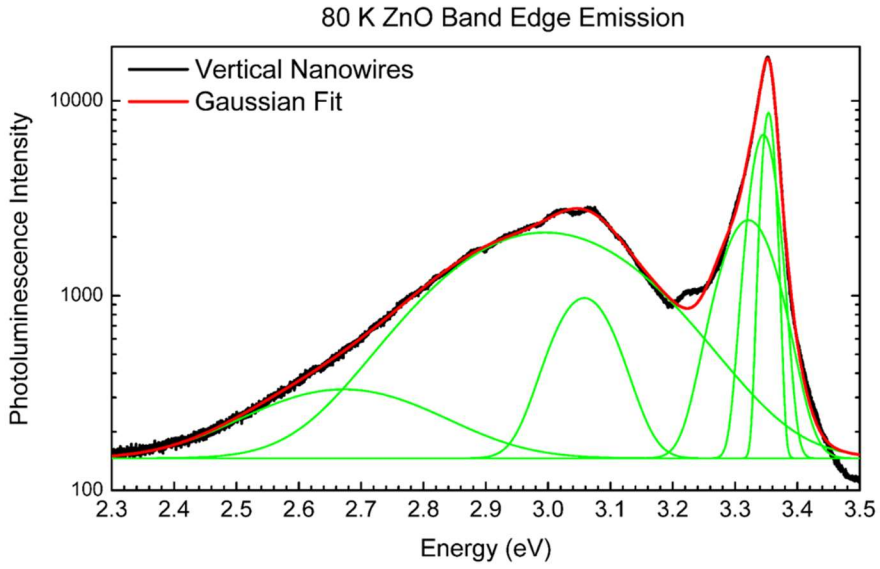

Figure A.3: Photoluminescence intensity versus energy (eV) of vertical ZnO nanowires at 80 K (black line), with a sum of six Gaussian functions overlaid in red on the experimental data. Each Gaussian is independently shown in green, fit using OriginPro.

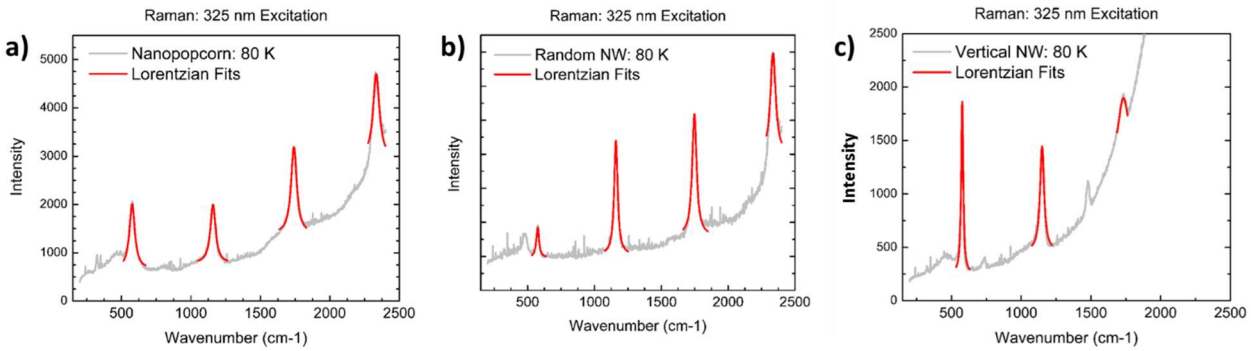

Figure A.4: Raman intensity versus wavenumber (cm-1) of ZnO nanostructures at 80 K (black line), with individual Lorentzian fits to each LO phonon mode of ZnO, fit using OriginPro: a) nanopopcorn, b) random nanowires, c) vertical nanowires.

REFERENCES

1 Djurišić, A., Ng, A. & Chen, X. ZnO nanostructures for optoelectronics: material properties and device applications. *Progress in Quantum Electronics* **34**, 191-259 (2010).

2 Lorenz, M. *et al.* The 2016 oxide electronic materials and oxide interfaces roadmap. *Journal of Physics D: Applied Physics* **49**, 433001 (2016).

3 Moezzi, A., McDonagh, A. M. & Cortie, M. B. Zinc oxide particles: Synthesis, properties and applications. *Chemical Engineering Journal* **185**, 1-22 (2012).

4 Ober, J. A. Mineral commodity summaries 2017. (US Geological Survey, 2017).

5 Wang, Z. L. Zinc oxide nanostructures: growth, properties and applications. *Journal of Physics: Condensed Matter* **16**, R829 (2004).

6 Janotti, A. & Van de Walle, C. G. Fundamentals of zinc oxide as a semiconductor. *Reports on progress in physics* **72**, 126501 (2009).

7 Klingshirn, C. F., Waag, A., Hoffmann, A. & Geurts, J. *Zinc oxide: from fundamental properties towards novel applications*. Vol. 120 (Springer Science & Business Media, 2010).

8 Özgür, Ü. *et al.* A comprehensive review of ZnO materials and devices. *Journal of applied physics* **98**, 041301 (2005).

9 Huang, J. *et al.* ZnO p–n Homojunction Random Laser Diode Based on Nitrogen-Doped p-type Nanowires. *Advanced Optical Materials* **1**, 179-185 (2013).

10 Kumar, R., Al-Dossary, O., Kumar, G. & Umar, A. Zinc oxide nanostructures for NO2 gas–sensor applications: a review. *Nano-Micro Letters* **7**, 97-120 (2015).

11 Huang, M. H. *et al.* Room-temperature ultraviolet nanowire nanolasers. *science* **292**, 1897-1899 (2001).

12 Law, M., Greene, L. E., Johnson, J. C., Saykally, R. & Yang, P. D. Nanowire dye-sensitized solar cells. *Nat. Mater.* **4**, 455-459, doi:10.1038/nmat1387 (2005).

13 Fan, J. C., Sreekanth, K., Xie, Z., Chang, S. & Rao, K. V. p-Type ZnO materials: theory, growth, properties and devices. *Progress in Materials Science* **58**, 874-985 (2013).

14 Tsukazaki, A. *et al.* Repeated temperature modulation epitaxy for p-type doping and light-emitting diode based on ZnO. *Nat. Mater.* **4**, 42-46 (2005).

15 Yoo, J. *et al.* Single crystalline ZnO radial homojunction light-emitting diodes fabricated by metalorganic chemical vapour deposition. *Nanotechnology* **28**, 394001 (2017).

16 Amano, H., Kito, M., Hiramatsu, K. & Akasaki, I. P-type conduction in Mg-doped GaN treated with low-energy electron beam irradiation (LEEBI). *Japanese Journal of Applied Physics* **28**, L2112 (1989).

17 Amano, H. *Growth of GaN on Sapphire by Low Temperature Deposited Buffer Layer and Realization of P-Type GaN by Mg-Doping Followed by LEEBI Treatment*, <http://www.nobelprize.org/nobel_prizes/physics/laureates/2014/amano-lecture.html> (2014).

18 Zuniga-Perez, J. *et al.* Ordered growth of tilted ZnO nanowires: morphological, structural and optical characterization. *Nanotechnology* **18**, 195303 (2007).

19 Song, J., Wang, X., Wang, X., Riedo, E. & Wang, Z. L. Systematic study on experimental conditions for large-scale growth of aligned ZnO nanwires on nitrides. *The Journal of Physical Chemistry B* **109**, 9869-9872 (2005).

20 Djurišić, A. B. & Leung, Y. H. Optical properties of ZnO nanostructures. *small* **2**, 944-961 (2006).
21 Zhang, C. *et al.* Enhanced waveguide-type ultraviolet electroluminescence from ZnO/MgZnO core/shell nanorod array light-emitting diodes via coupling with Ag nanoparticles localized surface plasmons. *Nanoscale* **7**, 1073-1080 (2015).
22 Johnson, J. C., Yan, H., Yang, P. & Saykally, R. J. Optical cavity effects in ZnO nanowire lasers and waveguides. *The journal of physical chemistry B* **107**, 8816-8828 (2003).
23 Kirschbrown, J. R., House, R. L., Mehl, B. P., Parker, J. K. & Papanikolas, J. M. Hybrid Standing Wave and Whispering Gallery Modes in Needle-Shaped ZnO Rods: Simulation of Emission Microscopy Images Using Finite Difference Frequency Domain Methods with a Focused Gaussian Source. *The Journal of Physical Chemistry C* **117**, 10653-10660 (2013).
24 Dong, H. *et al.* Geometry dependent evolution of the resonant mode in ZnO elongated hexagonal microcavity. *Scientific reports* **6** (2016).
25 Sidiropoulos, T. P. *et al.* Ultrafast plasmonic nanowire lasers near the surface plasmon frequency. *Nature Physics* **10**, 870-876 (2014).
26 Lu, J. *et al.* Plasmon-mediated exciton–phonon coupling in a ZnO microtower cavity. *Journal of Materials Chemistry C* **4**, 7718-7723 (2016).
27 Wei, J., Jiang, N., Xu, J., Bai, X. & Liu, J. Strong coupling between ZnO excitons and localized surface plasmons of silver nanoparticles studied by STEM-EELS. *Nano letters* **15**, 5926-5931 (2015).
28 Haglund, R. F., Lawrie, B. J. & Mu, R. Coupling of photoluminescent centers in ZnO to localized and propagating surface plasmons. *Thin Solid Films* **518**, 4637-4643 (2010).
29 Lawrie, B. J., Kim, K.-W., Norton, D. P. & Haglund Jr, R. F. Plasmon–exciton hybridization in ZnO quantum-well Al nanodisc heterostructures. *Nano letters* **12**, 6152-6157 (2012).
30 Hachtel, J. A. *et al.* Probing plasmons in three dimensions by combining complementary spectroscopies in a scanning transmission electron microscope. *Nanotechnology* **27**, 155202 (2016).
31 Mayo, D. C. *et al.* Surface-plasmon mediated photoluminescence from Ag-coated ZnO/MgO core–shell nanowires. *Thin Solid Films* **553**, 132-137 (2014).
32 Marvinney, C. E. *et al.* Effect of Material Structure on Photoluminescence of ZnO/MgO Core-Shell Nanowires. *ChemNanoMat* **4**, 291-300, doi:10.1002/cnma.201700313 (2018).
33 Liu, C. *et al.* Electrically pumped near-ultraviolet lasing from ZnO/MgO core/shell nanowires. *Applied Physics Letters* **99**, 063115 (2011).
34 Chu, S. *et al.* Electrically pumped waveguide lasing from ZnO nanowires. *Nature nanotechnology* **6**, 506-510 (2011).
35 Kong, J. *et al.* Use of distributed Bragg reflectors to enhance Fabry–PÚrot lasing in vertically aligned ZnO nanowires. *Applied Physics A* **110**, 23-28 (2013).
36 Baek, H. *et al.* ZnO nanolasers on graphene films. *Applied Physics Letters* **108**, 263102 (2016).
37 Li, J. *et al.* Single Mode ZnO Whispering-Gallery Submicron Cavity and Graphene Improved Lasing Performance. *ACS nano* **9**, 6794-6800 (2015).

38 Cook, A. L., Carson, C. S., Marvinney, C. E., Giorgio, T. D. & Mu, R. R. Sensing trace levels of molecular species in solution via zinc oxide nanoprobe Raman spectroscopy. *Journal of Raman Spectroscopy* **48**, 1116-1121 (2017).
39 Appavoo, K., Liu, X., Menon, V. & Sfeir, M. Y. Excitonic lasing in solution-processed subwavelength nanosphere assemblies. *Nano letters* **16**, 2004-2010 (2016).
40 Kim, S.-K., Jeong, S.-Y. & Cho, C.-R. Structural reconstruction of hexagonal to cubic ZnO films on Pt/Ti/SiO 2/Si substrate by annealing. *Applied Physics Letters* **82**, 562-564 (2003).
41 Pauling, L. *The nature of the chemical bond and the structure of molecules and crystals: an introduction to modern structural chemistry*. Vol. 18 (Cornell university press, 1960).
42 Phillips, J. Bonds and bands in semiconductors (Academic, New York, 1973). *Google Scholar* (1979).
43 Blachnik, R. *et al.* (Springer, Berlin, 1999).
44 Wang, Z. L. ZnO nanowire and nanobelt platform for nanotechnology. *Materials Science and Engineering: R: Reports* **64**, 33-71 (2009).
45 Voss, T., Svacha, G. T., Mazur, E., Müller, S. & Ronning, C. The influence of local heating by nonlinear pulsed laser excitation on the transmission characteristics of a ZnO nanowire waveguide. *Nanotechnology* **20**, 095702 (2009).
46 Neumann, U., Grunwald, R., Griebner, U., Steinmeyer, G. & Seeber, W. Second-harmonic efficiency of ZnO nanolayers. *Applied physics letters* **84**, 170-172 (2004).
47 Chang, Y.-T. *et al.* Excellent piezoelectric and electrical properties of lithium-doped ZnO nanowires for nanogenerator applications. *Nano Energy* **8**, 291-296 (2014).
48 Araneo, R., Rinaldi, A., Notargiacomo, A., Pea, M. & Celozzi, S. Advanced mechanical and electrical characterization of piezoelectric ZnO nanowires for electro-mechanical modeling of enhanced performance sensors. *Sensors and Actuators A: Physical* **244**, 166-173 (2016).
49 Damen, T. C., Porto, S. & Tell, B. Raman effect in zinc oxide. *Physical Review* **142**, 570 (1966).
50 Serrano, J. *et al.* Pressure dependence of the lattice dynamics of ZnO: An ab initio approach. *Physical Review B* **69**, 094306 (2004).
51 Serrano, J. *et al.* Dispersive phonon linewidths: the E 2 phonons of ZnO. *Physical review letters* **90**, 055510 (2003).
52 Thoma, K., Dorner, B., Duesing, G. & Wegener, W. Lattice dynamics of ZnO. *Solid State Communications* **15**, 1111-1114 (1974).
53 Hewat, A. Lattice dynamics of ZnO and BeO. *Solid State Communications* **8**, 187-189 (1970).
54 Gao, P. X. & Wang, Z. L. Nanopropeller arrays of zinc oxide. *Applied physics letters* **84**, 2883-2885 (2004).
55 Kong, X. Y. & Wang, Z. L. Spontaneous polarization-induced nanohelixes, nanosprings, and nanorings of piezoelectric nanobelts. *Nano Letters* **3**, 1625-1631 (2003).
56 Cao, L. *et al.* Engineering light absorption in semiconductor nanowire devices. *Nature materials* **8**, 643-647 (2009).
57 Fonoberov, V. A. & Balandin, A. A. ZnO quantum dots: physical properties and optoelectronic applications. *Journal of Nanoelectronics and Optoelectronics* **1**, 19-38 (2006).

58 Yang, L. *et al.* Enhanced Electroluminescence from ZnO Quantum Dot Light-Emitting Diodes via Introducing Al2O3 Retarding Layer and Ag@ ZnO Hybrid Nanodots. *Advanced Optical Materials* (2017).
59 Vasireddi, R., Javvaji, B., Vardhan, H., Mahapatra, D. & Hegde, G. Growth of zinc oxide nanorod structures: pressure controlled hydrothermal process and growth mechanism. *Journal of Materials Science* **52**, 2007-2020 (2017).
60 Liu, D. *et al.* A simple route to scalable fabrication of perfectly ordered ZnO nanorod arrays. *Nanotechnology* **18**, 405303 (2007).
61 Vega, N. *et al.* The shell effect on the room temperature photoluminescence from ZnO/MgO core/shell nanowires: exciton–phonon coupling and strain. *Nanotechnology* **28**, 275702 (2017).
62 Liu, W. Z. *et al.* Enhanced ultraviolet emission and improved spatial distribution uniformity of ZnO nanorod array light-emitting diodes via Ag nanoparticles decoration. *Nanoscale* **5**, 8634-8639 (2013).
63 Wille, M. *et al.* Carrier density driven lasing dynamics in ZnO nanowires. *Nanotechnology* **27**, 225702 (2016).
64 Liu, W. *et al.* Heteroepitaxial growth and spatially resolved cathodoluminescence of ZnO/MgZnO coaxial nanorod arrays. *The Journal of Physical Chemistry C* **114**, 16148-16152 (2010).
65 Vayssieres, L. Growth of arrayed nanorods and nanowires of ZnO from aqueous solutions. *Advanced Materials* **15**, 464-466 (2003).
66 Greene, L. E. *et al.* Low-temperature wafer-scale production of ZnO nanowire arrays. *Angewandte Chemie International Edition* **42**, 3031-3034 (2003).
67 Huang, M. H. *et al.* Catalytic growth of zinc oxide nanowires by vapor transport. *Advanced Materials* **13**, 113-116 (2001).
68 McCluskey, M. D. & Jokela, S. J. Defects in ZnO. *Journal of Applied Physics* **106**, 071101, doi:10.1063/1.3216464 (2009).
69 Derenzo, S. E., Weber, M. J., Bourret-Courchesne, E. & Klintenberg, M. K. The quest for the ideal inorganic scintillator. *Nuclear Instruments and Methods in Physics Research Section A: Accelerators, Spectrometers, Detectors and Associated Equipment* **505**, 111-117, doi:10.1016/s0168-9002(03)01031-3 (2003).
70 Fox, M. *Optical Properties of Solids*. 2 edn, Vol. 3 416 (Oxford University Press, 2010).
71 Morkoç, H. & Özgür, Ü. General properties of ZnO. *Zinc Oxide: Fundamentals, Materials and Device Technology*, 1-76 (2009).
72 Vogel, D., Krüger, P. & Pollmann, J. Ab initio electronic-structure calculations for II-VI semiconductors using self-interaction-corrected pseudopotentials. *Physical Review B* **52**, R14316 (1995).
73 Zwicker, G. & Jacobi, K. Experimental band structure of ZnO. *Solid state communications* **54**, 701-704 (1985).
74 Laskowski, R. & Christensen, N. E. Ab initio calculation of excitons in ZnO. *Physical Review B* **73**, 045201 (2006).
75 Hümmer, K. Interband magnetoreflection of ZnO. *physica status solidi (b)* **56**, 249-260 (1973).
76 Zhao, Q. *et al.* Deep-level emissions influenced by O and Zn implantations in ZnO. *Applied Physics Letters* **87**, 211912 (2005).

77 Wang, Y., Ren, F., Kim, H., Pearton, S. & Norton, D. Incorporation and drift of hydrogen at low temperatures in ZnO. *Applied Physics Letters* **90**, 092116 (2007).
78 Lin, B., Fu, Z. & Jia, Y. Green luminescent center in undoped zinc oxide films deposited on silicon substrates. *Applied Physics Letters* **79**, 943-945 (2001).
79 Shalish, I., Temkin, H. & Narayanamurti, V. Size-dependent surface luminescence in ZnO nanowires. *Physical Review B* **69**, 245401 (2004).
80 Djurišić, A. *et al.* Photoluminescence and electron paramagnetic resonance of ZnO tetrapod structures. *Advanced Functional Materials* **14**, 856-864 (2004).
81 Leung, Y. *et al.* Green emission in ZnO nanostructures—Examination of the roles of oxygen and zinc vacancies. *Applied Surface Science* **271**, 202-209 (2013).
82 Park, C., Lee, J. & Chang, W. S. Geometrical Separation of Defect States in ZnO Nanorods and Their Morphology-Dependent Correlation between Photoluminescence and Photoconductivity. *The Journal of Physical Chemistry C* **119**, 16984-16990 (2015).
83 Maier, S. A. *Plasmonics: fundamentals and applications*. (Springer Science & Business Media, 2007).
84 Lu, J. *et al.* Improved UV photoresponse of ZnO nanorod arrays by resonant coupling with surface plasmons of Al nanoparticles. *Nanoscale* **7**, 3396-3403 (2015).
85 Purcell, E. M. in *Confined Electrons and Photons: New Physics and Applications* (eds Elias Burstein & Claude Weisbuch) 839-839 (Springer US, 1995).
86 Koenderink, A. F. On the use of Purcell factors for plasmon antennas. *Optics letters* **35**, 4208-4210 (2010).
87 Fox, M. *Optical properties of solids*. Vol. 3 (Oxford university press, 2010).
88 Liu, W. *et al.* Effect of SiO2 Spacer-Layer Thickness on Localized Surface Plasmon-Enhanced ZnO Nanorod Array LEDs. *ACS applied materials & interfaces* **8**, 1653-1660 (2016).
89 Nakamura, S., Mukai, T., Senoh, M. & Iwasa, N. Thermal annealing effects on p-type Mg-doped GaN films. *Japanese Journal of Applied Physics* **31**, L139 (1992).
90 Khan, M. A., Chen, Q., Skogman, R. & Kuznia, J. Violet-blue GaN homojunction light emitting diodes with rapid thermal annealed p-type layers. *Applied physics letters* **66**, 2046-2047 (1995).
91 Pearton, S., Ren, F., Zhang, A. & Lee, K. Fabrication and performance of GaN electronic devices. *Materials Science and Engineering: R: Reports* **30**, 55-212 (2000).
92 Vayssieres, L. On the design of advanced metal oxide nanomaterials. *International Journal of Nanotechnology* **1**, 1-41 (2004).
93 Young Bae, M., Whon Min, K., Yoon, J., Kim, G.-T. & Sook Ha, J. Electronic properties of light-emitting pn hetero-junction array consisting of p+-Si and aligned n-ZnO nanowires. *Journal of Applied Physics* **113**, 084310 (2013).
94 Chen, X. *et al.* GaN/MgO/ZnO heterojunction light-emitting diodes. *Thin Solid Films* **527**, 303-307 (2013).
95 Li, G. *et al.* Synthesis and characterization of p–n homojunction-containing zinc oxide nanowires. *Nanoscale* **5**, 2259-2263 (2013).
96 Wang, C.-S., Lin, H.-Y., Lin, J.-M. & Chen, Y.-F. Surface-plasmon-enhanced ultraviolet random lasing from ZnO nanowires assisted by Pt nanoparticles. *Applied Physics Express* **5**, 062003 (2012).
97 Liu, X.-Y., Shan, C.-X., Wang, S.-P., Zhang, Z.-Z. & Shen, D.-Z. Electrically pumped random lasers fabricated from ZnO nanowire arrays. *Nanoscale* **4**, 2843-2846 (2012).

98 Hassan, J., Mahdi, M., Chin, C., Abu-Hassan, H. & Hassan, Z. A high-sensitivity room-temperature hydrogen gas sensor based on oblique and vertical ZnO nanorod arrays. *Sensors and Actuators B: Chemical* **176**, 360-367 (2013).
99 Na, C. W., Woo, H.-S., Kim, I.-D. & Lee, J.-H. Selective detection of NO 2 and C 2 H 5 OH using a Co 3 O 4-decorated ZnO nanowire network sensor. *Chemical Communications* **47**, 5148-5150 (2011).
100 Jung, M., Kim, S. & Ju, S. Enhancement of green emission from Sn-doped ZnO nanowires. *Optical Materials* **33**, 280-283 (2011).
101 Sun, L., He, H., Liu, C. & Ye, Z. Highly efficient orange emission in ZnO: Se nanorods. *Journal of Applied Physics* **108**, 124313 (2010).
102 Burke, P. J., Li, S. & Yu, Z. Quantitative theory of nanowire and nanotube antenna performance. *IEEE transactions on nanotechnology* **5**, 314-334 (2006).
103 Kwon, M. K. *et al.* Surface-plasmon-enhanced light-emitting diodes. *Advanced Materials* **20**, 1253-1257 (2008).
104 Dreaden, E. C., Alkilany, A. M., Huang, X., Murphy, C. J. & El-Sayed, M. A. The golden age: gold nanoparticles for biomedicine. *Chemical Society Reviews* **41**, 2740-2779 (2012).
105 Zhang, R. *et al.* Chemical mapping of a single molecule by plasmon-enhanced Raman scattering. *Nature* **498**, 82-86 (2013).
106 Pillai, S. *et al.* Enhanced emission from Si-based light-emitting diodes using surface plasmons. *Applied physics letters* **88**, 161102 (2006).
107 Ferry, V. E., Sweatlock, L. A., Pacifici, D. & Atwater, H. A. Plasmonic nanostructure design for efficient light coupling into solar cells. *Nano letters* **8**, 4391-4397 (2008).
108 Sonnefraud, Y., Leen Koh, A., McComb, D. W. & Maier, S. A. Nanoplasmonics: engineering and observation of localized plasmon modes. *Laser & Photonics Reviews* **6**, 277-295 (2012).
109 Jin, D. *et al.* Quantum-spillover-enhanced surface-plasmonic absorption at the interface of silver and high-index dielectrics. *Physical review letters* **115**, 193901 (2015).
110 Akselrod, G. M. *et al.* Leveraging nanocavity harmonics for control of optical processes in 2D semiconductors. (2015).
111 Knight, M. W., Sobhani, H., Nordlander, P. & Halas, N. J. Photodetection with active optical antennas. *Science* **332**, 702-704 (2011).
112 Atwater, H. A. & Polman, A. Plasmonics for improved photovoltaic devices. *Nat. Mater.* **9**, 205-213 (2010).
113 Miroshnichenko, A. E., Flach, S. & Kivshar, Y. S. Fano resonances in nanoscale structures. *Reviews of Modern Physics* **82**, 2257 (2010).
114 Novotny, L. & Van Hulst, N. Antennas for light. *Nature photonics* **5**, 83-90 (2011).
115 Lawrie, B. J., Kim, K. W., Norton, D. P. & Haglund, R. F., Jr. Plasmon-exciton hybridization in ZnO quantum-well Al nanodisc heterostructures. *Nano Lett* **12**, 6152-6157, doi:10.1021/nl3029784 (2012).
116 Fang, Y. *et al.* Behind the change of the photoluminescence property of metal-coated ZnO nanowire arrays. *Applied Physics Letters* **98**, 033103 (2011).
117 Park, S., An, S., Mun, Y., Kim, H. W. & Lee, C. Enhanced luminescence of Ag-decorated ZnO nanorods. *Journal of Materials Science: Materials in Electronics* **24**, 4906-4912 (2013).

118 Li, J. *et al.* Enhanced ultraviolet emission from ZnS-coated ZnO nanowires fabricated by self-assembling method. *The Journal of Physical Chemistry B* **110**, 14685-14687 (2006).
119 Wu, Y., Wu, W., Zou, X., Xu, L. & Li, J. Growth and great UV emission improvement of highly crystalline quality core–shell ZnO/MgO nanowires. *Materials Letters* **84**, 147-150 (2012).
120 Yang, H., Yu, S., Li, G. & Wu, T. Random lasing action of randomly assembled ZnO nanowires with MgO coating. *Optics express* **18**, 13647-13654 (2010).
121 Xue, M., Guo, Q., Wu, K. & Guo, J. Initial oxidation and interfacial diffusion of Zn on faceted MgO (111) films. *Langmuir* **24**, 8760-8764 (2008).
122 Jiang, Q., Zheng, H., Wang, J., Long, H. & Fang, G. Structural and Optical Characterization of ZnO/Mg x Zn1–x O Multiple Quantum Wells Based Random Laser Diodes. *ACS applied materials & interfaces* **4**, 7043-7046 (2012).
123 Jin, C., Kim, H., Ryu, H.-Y., Kim, H. W. & Lee, C. Subwavelength optical resonant cavity-induced enhancement of the near-band-edge emission from ZnO-core/SnO2-shell nanorods. *The Journal of Physical Chemistry C* **115**, 8513-8518 (2011).
124 Gargas, D. J. *et al.* Whispering gallery mode lasing from zinc oxide hexagonal nanodisks. *ACS nano* **4**, 3270-3276 (2010).
125 Postava, K. *et al.* Spectroscopic ellipsometry of epitaxial ZnO layer on sapphire substrate. *Journal of Applied Physics* **87**, 7820-7824 (2000).
126 Stephens, R. E. & Malitson, I. H. Index of refraction of magnesium oxide. *Journal of Research of the National Bureau of Standards* **49**, 249-252 (1952).
127 Vedam, K. & Kim, S. Y. Simultaneous determination of refractive index, its dispersion and depth-profile of magnesium oxide thin film by spectroscopic ellipsometry. *Applied optics* **28**, 2691-2694 (1989).
128 Chen, J., Aé, L., Aichele, C. & Lux-Steiner, M. C. High internal quantum efficiency ZnO nanorods prepared at low temperature. *Applied Physics Letters* **92**, 161906 (2008).
129 Gargas, D. J., Gao, H., Wang, H. & Yang, P. High Quantum Efficiency of Band-Edge Emission from ZnO Nanowires. *Nano Letters* **11**, 3792-3796, doi:10.1021/nl201850k (2011).
130 Yan, R., Gargas, D. & Yang, P. Nanowire photonics. *Nature photonics* **3**, 569-576 (2009).
131 Li, W. *et al.* Angular dependent luminescence of individual suspended ZnO nanorods. *Applied Physics Letters* **93**, 023117 (2008).
132 Manekkathodi, A. *et al.* Integrated optical waveguide and photodetector arrays based on comb-like ZnO structures. *Nanoscale* **5**, 12185-12191 (2013).
133 Zhang, A., Zheng, G. & Lieber, C. M. in *Nanowires* 143-175 (Springer, 2016).
134 Stockman, M. I. Nanofocusing of optical energy in tapered plasmonic waveguides. *Physical review letters* **93**, 137404 (2004).
135 Prodan, E., Radloff, C., Halas, N. J. & Nordlander, P. A hybridization model for the plasmon response of complex nanostructures. *science* **302**, 419-422 (2003).
136 Oulton, R. F. *et al.* Plasmon lasers at deep subwavelength scale. *Nature* **461**, 629-632 (2009).
137 Fei, Z. *et al.* Gate-tuning of graphene plasmons revealed by infrared nano-imaging. *arXiv preprint arXiv:1202.4993* (2012).
138 Novotny, L. & Stranick, S. J. Near-field optical microscopy and spectroscopy with pointed probes. *Annu. Rev. Phys. Chem.* **57**, 303-331 (2006).

139 Fang, Y., Seong, N.-H. & Dlott, D. D. Measurement of the distribution of site enhancements in surface-enhanced Raman scattering. *Science* **321**, 388-392 (2008).
140 Peppernick, S. J., Joly, A. G., Beck, K. M. & Hess, W. P. Plasmon-induced optical field enhancement studied by correlated scanning and photoemission electron microscopy. *The Journal of chemical physics* **138**, 154701 (2013).
141 Kociak, M. *et al.* Seeing and measuring in colours: Electron microscopy and spectroscopies applied to nano-optics. *Comptes Rendus Physique* **15**, 158-175 (2014).
142 Chang, J.-J. & Langreth, D. C. Deep-hole excitations in solids. I. Fast-electron-plasmon effects. *Physical Review B* **5**, 3512 (1972).
143 Schmeits, M. & Dambly, L. Fast-electron scattering by bispherical surface-plasmon modes. *Physical review B* **44**, 12706 (1991).
144 Muller, D. & Silcox, J. Delocalization in inelastic scattering. *Ultramicroscopy* **59**, 195-213 (1995).
145 Gerchikov, L. G., Ipatov, A. N., Solov'yov, A. V. & Greiner, W. Excitation of multipole plasmon resonances in clusters by fast electron impact. *Journal of Physics B: Atomic, Molecular and Optical Physics* **31**, 3065 (1998).
146 Yamamoto, N., Araya, K. & de Abajo, F. G. Photon emission from silver particles induced by a high-energy electron beam. *Physical Review B* **64**, 205419 (2001).
147 Nelayah, J. *et al.* Mapping surface plasmons on a single metallic nanoparticle. *Nature Physics* **3**, 348-353 (2007).
148 Chaturvedi, P., Hsu, K., Kumar, A., Mabon, J. C. & Fang, N. Imaging of plasmonic modes of silver nanoparticles using high-resolution cathodoluminescence spectroscopy. *arXiv preprint arXiv:0906.1077* (2009).
149 Guiton, B. S. *et al.* Correlated optical measurements and plasmon mapping of silver nanorods. *Nano Letters* **11**, 3482-3488 (2011).
150 Scholl, J. A., Koh, A. L. & Dionne, J. A. Quantum plasmon resonances of individual metallic nanoparticles. *Nature* **483**, 421-429 (2012).
151 García de Abajo, F. J. Graphene Plasmonics: Challenges and Opportunities. *ACS Photonics* **1**, 135-152, doi:10.1021/ph400147y (2014).
152 Kociak, M. & Stéphan, O. Mapping plasmons at the nanometer scale in an electron microscope. *Chemical Society Reviews* **43**, 3865-3883 (2014).
153 Jarrett, J. W., Zhao, T., Johnson, J. S. & Knappenberger Jr, K. L. Investigating plasmonic structure-dependent light amplification and electronic dynamics using advances in nonlinear optical microscopy. *The Journal of Physical Chemistry C* **119**, 15779-15800 (2015).
154 Liu, Z. *et al.* Multispectral spatial and frequency selective sensing with ultra-compact cross-shaped antenna plasmonic crystals. *Sensors and Actuators B: Chemical* **215**, 480-488 (2015).
155 Kruk, S. *et al.* Enhanced Magnetic Second-Harmonic Generation from Resonant Metasurfaces. *ACS Photonics* **2**, 1007-1012, doi:10.1021/acsphotonics.5b00215 (2015).
156 Losquin, A. *et al.* Unveiling nanometer scale extinction and scattering phenomena through combined electron energy loss spectroscopy and cathodoluminescence measurements. *Nano Lett* **15**, 1229-1237 (2015).
157 Nicoletti, O. *et al.* Three-dimensional imaging of localized surface plasmon resonances of metal nanoparticles. *Nature* **502**, 80-84 (2013).

158 Li, G. *et al.* Spatially mapping energy transfer from single plasmonic particles to semiconductor substrates via STEM/EELS. *Nano Lett* **15**, 3465-3471 (2015).
159 Atre, A. C., Dionne, J. A., Brenny, B., Coenen, T. & Polman, A. (Google Patents, 2015).
160 Perassi, E. M. *et al.* Using highly accurate 3D nanometrology to model the optical properties of highly irregular nanoparticles: a powerful tool for rational design of plasmonic devices. *Nano letters* **10**, 2097-2104 (2010).
161 Hernández-Garrido, J. *et al.* Exploring the benefits of electron tomography to characterize the precise morphology of core–shell Au@ Ag nanoparticles and its implications on their plasmonic properties. *Nanoscale* **6**, 12696-12702 (2014).
162 Egerton, R. F. *Electron energy-loss spectroscopy in the electron microscope*. (Springer Science & Business Media, 2011).
163 Heitmann, D. Radiative decay of surface plasmons excited by fast electrons on periodically modulated silver surfaces. *Journal of Physics C: Solid State Physics* **10**, 397 (1977).
164 Hofmann, C. E. *et al.* Plasmonic modes of annular nanoresonators imaged by spectrally resolved cathodoluminescence. *Nano letters* **7**, 3612-3617 (2007).
165 De Abajo, F. G. Optical excitations in electron microscopy. *Reviews of modern physics* **82**, 209 (2010).
166 Losquin, A. & Kociak, M. Link between cathodoluminescence and electron energy loss spectroscopy and the radiative and full electromagnetic local density of states. *Acs Photonics* **2**, 1619-1627 (2015).
167 Chu, M.-W. *et al.* Probing bright and dark surface-plasmon modes in individual and coupled noble metal nanoparticles using an electron beam. *Nano letters* **9**, 399-404 (2008).
168 Mazzucco, S. *et al.* Ultralocal modification of surface plasmons properties in silver nanocubes. *Nano letters* **12**, 1288-1294 (2012).
169 Myroshnychenko, V. *et al.* Plasmon spectroscopy and imaging of individual gold nanodecahedra: a combined optical microscopy, cathodoluminescence, and electron energy-loss spectroscopy study. *Nano letters* **12**, 4172-4180 (2012).
170 Koh, A. L. *et al.* Electron energy-loss spectroscopy (EELS) of surface plasmons in single silver nanoparticles and dimers: influence of beam damage and mapping of dark modes. *ACS nano* **3**, 3015-3022 (2009).
171 Zhu, X. *et al.* Confined three-dimensional plasmon modes inside a ring-shaped nanocavity on a silver film imaged by cathodoluminescence microscopy. *Physical review letters* **105**, 127402 (2010).
172 Coenen, T., Arango, F. B., Koenderink, A. F. & Polman, A. Directional emission from a single plasmonic scatterer. *Nat. Commun* **5**, 2 (2014).
173 Bosman, M., Keast, V. J., Watanabe, M., Maaroof, A. I. & Cortie, M. B. Mapping surface plasmons at the nanometre scale with an electron beam. *Nanotechnology* **18**, 165505 (2007).
174 Li, G. *et al.* Examining substrate-induced plasmon mode splitting and localization in truncated silver nanospheres with electron energy loss spectroscopy. *The journal of physical chemistry letters* **6**, 2569-2576 (2015).

175 Coenen, T., Vesseur, E. J. R., Polman, A. & Koenderink, A. F. Directional emission from plasmonic yagi–uda antennas probed by angle-resolved cathodoluminescence spectroscopy. *Nano letters* **11**, 3779-3784 (2011).
176 Kim, J., Lee, G. J., Park, I. & Lee, Y. P. Finite-difference time-domain numerical simulation study on the optical properties of silver nanocomposites. *Journal of nanoscience and nanotechnology* **12**, 5527-5531 (2012).
177 Iakoubovskii, K., Mitsuishi, K., Nakayama, Y. & Furuya, K. Mean free path of inelastic electron scattering in elemental solids and oxides using transmission electron microscopy: Atomic number dependent oscillatory behavior. *Physical Review B* **77**, 104102 (2008).
178 Losquin, A. *et al.* Experimental evidence of nanometer-scale confinement of plasmonic eigenmodes responsible for hot spots in random metallic films. *Physical Review B* **88**, 115427 (2013).
179 Bosman, M. *et al.* Encapsulated annealing: enhancing the plasmon quality factor in lithographically–defined nanostructures. *Scientific reports* **4**, 5537 (2014).
180 Talebi, N. *et al.* Excitation of mesoscopic plasmonic tapers by relativistic electrons: phase matching versus eigenmode resonances. *ACS nano* **9**, 7641-7648 (2015).
181 McMahon, M., Lopez, R., Meyer, H. M., Feldman, L. & Haglund, R. Rapid tarnishing of silver nanoparticles in ambient laboratory air. *Applied Physics B: Lasers and Optics* **80**, 915-921 (2005).
182 Li, C. *et al.* Nonpolar InGaN/GaN Core–Shell Single Nanowire Lasers. *Nano letters* **17**, 1049-1055 (2017).
183 Pal, A. K. & Mohan, D. B. Multi-angle ZnO microstructures grown on Ag nanorods array for plasmon-enhanced near-UV-blue light emitter. *Nanotechnology* **28**, 415707 (2017).
184 Wang, Y. *et al.* Plasmon enhancement for Vernier coupled single-mode lasing from ZnO/Pt hybrid microcavities. *Nano Research* **10**, 3447-3456 (2017).
185 Chen, B. *et al.* Graphene coated ZnO nanowire optical waveguides. *Optics Express* **22**, 24276-24285, doi:10.1364/OE.22.024276 (2014).
186 Sergent, S. *et al.* Nanomanipulating and Tuning Ultraviolet ZnO-Nanowire-Induced Photonic Crystal Nanocavities. *ACS Photonics* **4**, 1040-1047 (2017).
187 Grinblat, G., Capeluto, M., Tirado, M., Bragas, A. & Comedi, D. Hierarchical ZnO nanostructures: Growth mechanisms and surface correlated photoluminescence. *Applied Physics Letters* **100**, 233116 (2012).
188 Fang, X. *et al.* Ultraviolet Electroluminescence from ZnS@ ZnO Core–Shell Nanowires/p-GaN Introduced by Exciton Localization. *ACS applied materials & interfaces* **8**, 1661-1666 (2016).
189 Grinblat, G., Borrero-González, L., Nunes, L. A. d. O., Tirado, M. & Comedi, D. Enhanced optical properties and (Zn, Mg) interdiffusion in vapour transport grown ZnO/MgO core/shell nanowires. *Nanotechnology* **25**, 035705 (2013).
190 Zhang, Y. *et al.* Photoluminescence enhancement of ZnO nanowire arrays by atomic layer deposition of ZrO 2 layers and thermal annealing. *Physical Chemistry Chemical Physics* **18**, 16377-16385 (2016).
191 Mudusu, D. *et al.* Electrical properties of polycrystalline and single crystalline nickel layer capped ZnO nanowires. *Current Applied Physics* **17**, 1699-1706 (2017).

192 Mo, X. *et al.* Unusual electroluminescence from n-ZnO@ i-MgO core–shell nanowire color-tunable light-emitting diode at reverse bias. *Physical Chemistry Chemical Physics* **16**, 9302-9308 (2014).
193 Azzez, S. A. *et al.* Preparation of high quality Mg doped ZnO nanorod arrays with enhanced optical properties by MgO passivation. *Optik-International Journal for Light and Electron Optics* **127**, 9250-9258 (2016).
194 Yang, S. *et al.* Identification and characteristics of ZnO/MgO core-shell nanowires. *AIP Advances* **5**, 037122 (2015).
195 Zhang, Y. *et al.* Facile synthesis and enhanced luminescent properties of ZnO/HfO 2 core–shell nanowires. *Nanoscale* **7**, 15462-15468 (2015).
196 Norek, M., Zaleszczyk, W., Łuka, G., Budner, B. & Zasada, D. Tailoring UV emission from a regular array of ZnO nanotubes by the geometrical parameters of the array and Al 2 O 3 coating. *Ceramics International* **43**, 5693-5701 (2017).
197 Gao, M. *et al.* Synthesis and characterization of aligned ZnO/MgO core–shell nanorod arrays on ITO substrate. *Applied Physics B* **112**, 539-545 (2013).
198 Jin, C., Kim, H., Hong, C., Lee, J. & Lee, C. Luminescence properties of MgO-sheathed and annealed ZnO nanowires. *Current Applied Physics* **11**, S60-S64 (2011).
199 Meng, X., Peng, H., Gai, Y. & Li, J. Influence of ZnS and MgO shell on the photoluminescence properties of ZnO core/shell nanowires. *The Journal of Physical Chemistry C* **114**, 1467-1471 (2009).
200 Shi, Z.-F. *et al.* Photoluminescence performance enhancement of ZnO/MgO heterostructured nanowires and their applications in ultraviolet laser diodes. *Physical Chemistry Chemical Physics* **17**, 13813-13820 (2015).
201 Gu, Y., Li, X., Zhao, J., Yu, W. & Gao, X. Structure and photoresponse characteristics of ZnO thin films grown at high oxygen partial pressure. *Journal of Crystal Growth* **308**, 1-4, doi:http://dx.doi.org/10.1016/j.jcrysgro.2007.07.016 (2007).
202 Locker, D. & Meese, J. Displacement thresholds in ZnO. *IEEE Transactions on Nuclear Science* **19**, 237-242 (1972).
203 Limpijumnong, S. & Lambrecht, W. R. Theoretical study of the relative stability of wurtzite and rocksalt phases in MgO and GaN. *Physical Review B* **63**, 104103 (2001).
204 Perdew, J. P., Burke, K. & Ernzerhof, M. Generalized gradient approximation made simple. *Physical review letters* **77**, 3865 (1996).
205 Blöchl, P. E. Projector augmented-wave method. *Physical review B* **50**, 17953 (1994).
206 Kresse, G. & Joubert, D. From ultrasoft pseudopotentials to the projector augmented-wave method. *Physical Review B* **59**, 1758 (1999).
207 Kresse, G. & Furthmüller, J. Efficient iterative schemes for ab initio total-energy calculations using a plane-wave basis set. *Physical review B* **54**, 11169 (1996).
208 Zhu, Y. *et al.* Electronic structure and phase stability of MgO, ZnO, CdO, and related ternary alloys. *Physical Review B* **77**, 245209 (2008).
209 Melati, D., Melloni, A. & Morichetti, F. Real photonic waveguides: guiding light through imperfections. *Advances in Optics and Photonics* **6**, 156-224, doi:10.1364/AOP.6.000156 (2014).
210 Jaberansary, E. *et al.* Scattering loss estimation using 2-D Fourier analysis and modeling of sidewall roughness on optical waveguides. *IEEE Photonics Journal* **5**, 6601010-6601010 (2013).

211 Seibert, C. S., Liang, D., Hall, D. C. & Shellenbarger, Z. A. in *Lasers and Electro-Optics, 2008 and 2008 Conference on Quantum Electronics and Laser Science. CLEO/QELS 2008. Conference on.* 1-2 (IEEE).
212 Lee, K. K., Lim, D. R., Kimerling, L. C., Shin, J. & Cerrina, F. Fabrication of ultralow-loss Si/SiO 2 waveguides by roughness reduction. *Optics letters* **26**, 1888-1890 (2001).
213 Laatar, F., Hassen, M., Maaloul, N., Khirouni, K. & Ezzaouia, H. Correlation between microstructural and optical properties of silicon thin films grown onto porous alumina by plasma–enhanced CVD method. *Journal of Alloys and Compounds* **658**, 337-347 (2016).
214 Ho, I.-C., Xu, Y. & Mackenzie, J. D. Electrical and optical properties of MgO thin film prepared by sol-gel technique. *Journal of Sol-Gel Science and Technology* **9**, 295-301 (1997).
215 Zhu, D. *et al.* Effects of incidence angle on the structure and properties of cathodic vacuum arc deposition MgO thin films. *Materials Chemistry and Physics* **134**, 1167-1171 (2012).
216 Li, Q., Wan, Q., Liang, Y. & Wang, T. Electronic transport through individual ZnO nanowires. *Applied Physics Letters* **84**, 4556-4558 (2004).
217 van Dijken, A., Meulenkamp, E. A., Vanmaekelbergh, D. & Meijerink, A. The kinetics of the radiative and nonradiative processes in nanocrystalline ZnO particles upon photoexcitation. *The Journal of Physical Chemistry B* **104**, 1715-1723 (2000).
218 Tam, K. *et al.* Defects in ZnO nanorods prepared by a hydrothermal method. *The Journal of Physical Chemistry B* **110**, 20865-20871 (2006).
219 Fallert, J. *et al.* Surface-state related luminescence in ZnO nanocrystals. *Journal of Applied Physics* **101**, 073506 (2007).
220 Teke, A. *et al.* Excitonic fine structure and recombination dynamics in single-crystalline ZnO. *Physical Review B* **70**, 195207 (2004).
221 Boemare, C., Monteiro, T., Soares, M., Guilherme, J. & Alves, E. Photoluminescence studies in ZnO samples. *Physica B: Condensed Matter* **308**, 985-988 (2001).
222 Zhang, X., Taliercio, T., Kolliakos, S. & Lefebvre, P. Influence of electron-phonon interaction on the optical properties of III nitride semiconductors. *Journal of Physics: Condensed Matter* **13**, 7053 (2001).
223 Mohanta, S. *et al.* Emission characteristics of ZnO nanorods on nanosilicon-on-insulator: competition between exciton–phonon coupling and surface resonance effect. *Journal of Physics D: Applied Physics* **43**, 145404 (2010).
224 Varshni, Y. P. Temperature dependence of the energy gap in semiconductors. *physica* **34**, 149-154 (1967).
225 Bardeen, J. & Shockley, W. Deformation potentials and mobilities in non-polar crystals. *Physical Review* **80**, 72 (1950).
226 Kittel, C. Introduction to Solid State Physics. *University of Pennsylvania Law Review* **154**, 477 (2005).
227 Meyer, B. *et al.* Bound exciton and donor–acceptor pair recombinations in ZnO. *physica status solidi (b)* **241**, 231-260 (2004).
228 Gutowski, J., Presser, N. & Broser, I. Acceptor-exciton complexes in ZnO: A comprehensive analysis of their electronic states by high-resolution magnetooptics and excitation spectroscopy. *Physical Review B* **38**, 9746 (1988).
229 Narayanaamurti, V. Phonon optics and phonon propagation in semiconductors. *Science* **213**, 717-723 (1981).

230 Bekeny, C. *et al.* Influence of ZnO seed crystals and annealing on the optical quality of low-temperature grown ZnO nanorods. *Journal of Applied Physics* **102**, 044908 (2007).
231 Ma, Y., Guo, X., Wu, X., Dai, L. & Tong, L. Semiconductor nanowire lasers. *Advances in Optics and Photonics* **5**, 216-273 (2013).
232 Jewell, J. *et al.* Double embedded photonic crystals for extraction of guided light in light-emitting diodes. *Applied Physics Letters* **100**, 171105 (2012).
233 Walker, P. *et al.* Exciton polaritons in semiconductor waveguides. *Applied Physics Letters* **102**, 012109 (2013).
234 No, Y.-S. *et al.* A double-strip plasmonic waveguide coupled to an electrically driven nanowire LED. *Nano letters* **13**, 772-776 (2013).
235 Gutman, N., Dupree, W. H., Sun, Y., Sukhorukov, A. A. & de Sterke, C. M. Frozen and broadband slow light in coupled periodic nanowire waveguides. *Optics express* **20**, 3519-3528 (2012).
236 Madden, S. *et al.* Low loss coupling to sub-micron thick rib and nanowire waveguides by vertical tapering. *Optics express* **21**, 3582-3594 (2013).
237 Hirano, S. *et al.* Room-temperature nanowire ultraviolet lasers: an aqueous pathway for zinc oxide nanowires with low defect density. *Journal of applied physics* **98**, 094305 (2005).
238 van Vugt, L. K. *et al.* Variable temperature spectroscopy of as-grown and passivated CdS nanowire optical waveguide cavities. *The Journal of Physical Chemistry A* **115**, 3827-3833 (2011).
239 Zhao, S. *et al.* An electrically injected AlGaN nanowire laser operating in the ultraviolet-C band. *Applied Physics Letters* **107**, 043101 (2015).
240 Lai, E., Kim, W. & Yang, P. Vertical nanowire array-based light emitting diodes. *Nano Research* **1**, 123-128 (2008).
241 Dai, J., Xu, C. X. & Sun, X. W. ZnO-Microrod/p-GaN Heterostructured Whispering-Gallery-Mode Microlaser Diodes. *Advanced Materials* **23**, 4115-4119 (2011).
242 Zhu, H. *et al.* Ultralow-Threshold Laser Realized in Zinc Oxide. *Advanced Materials* **21**, 1613-1617 (2009).
243 Vanmaekelbergh, D. & Van Vugt, L. K. ZnO nanowire lasers. *Nanoscale* **3**, 2783-2800 (2011).
244 Hua, B., Motohisa, J., Ding, Y., Hara, S. & Fukui, T. Characterization of Fabry-Pérot microcavity modes in GaAs nanowires fabricated by selective-area metal organic vapor phase epitaxy. *Applied Physics Letters* **91**, 131112 (2007).
245 Couteau, C., Larrue, A., Wilhelm, C. & Soci, C. Nanowire lasers. *Nanophotonics* **4**, 90-107 (2015).
246 Xu, T., Yang, S., Nair, S. V. & Ruda, H. Nanowire-array-based photonic crystal cavity by finite-difference time-domain calculations. *Physical Review B* **75**, 125104 (2007).
247 Heo, J., Jahangir, S., Xiao, B. & Bhattacharya, P. Room-temperature polariton lasing from GaN nanowire array clad by dielectric microcavity. *Nano letters* **13**, 2376-2380 (2013).